8-31-2021

Modeling and design optimization for membrane filters

YiXuan Sun
New Jersey Institute of Technology

Copyright Warning & Restrictions

The copyright law of the United States (Title 17, United States Code) governs the making of photocopies or other reproductions of copyrighted material.

Under certain conditions specified in the law, libraries and archives are authorized to furnish a photocopy or other reproduction. One of these specified conditions is that the photocopy or reproduction is not to be "used for any purpose other than private study, scholarship, or research." If a, user makes a request for, or later uses, a photocopy or reproduction for purposes in excess of "fair use" that user may be liable for copyright infringement,

This institution reserves the right to refuse to accept a copying order if, in its judgment, fulfillment of the order would involve violation of copyright law.

Please Note: The author retains the copyright while the New Jersey Institute of Technology reserves the right to distribute this thesis or dissertation

Printing note: If you do not wish to print this page, then select "Pages from: first page # to: last page #" on the print dialog screen

ABSTRACT

MODELING AND DESIGN OPTIMIZATION FOR MEMBRANE FILTERS

by
YiXuan Sun

Membrane filtration is widely used in many applications, ranging from industrial processes to everyday living activities. With growing interest from both industrial and academic sectors in understanding the various types of filtration processes in use, and in improving filter performance, the past few decades have seen significant research activity in this area. Experimental studies can be very valuable, but are expensive and time-consuming, therefore theoretical studies offer potential as a cost-effective and predictive way to improve on current filter designs. In this work, mathematical models, derived from first principles and simplified using asymptotic analysis, are proposed for: (1) pleated membrane filters, where the macroscale flow problem of Darcy flow through a pleated porous medium is coupled to the microscale fouling problem of particle transport and deposition within individual pores of the membrane; (2) dead-end membrane filtration with feed containing multiple species of physicochemically-distinct particles, which interact with the membrane differently; and (3) filtration with reactive particle removal using porous media composed of chemically active granular materials. Asymptotically-simplified models are used to describe and evaluate the membrane performance numerically and filter design optimization problems are formulated and solved for a number of industrially-relevant scenarios. This study demonstrates the potential of such modeling to guide industrial membrane filter design for a range of applications involving purification and separation.

MODELING AND DESIGN OPTIMIZATION FOR MEMBRANE FILTERS

by
YiXuan Sun

A Dissertation
Submitted to the Faculty of
New Jersey Institute of Technology and
Rutgers, The State University of New Jersey – Newark
in Partial Fulfillment of the Requirements for the Degree of
Doctor of Philosophy in Mathematical Sciences

Department of Mathematical Sciences
Department of Mathematics and Computer Science, Rutgers-Newark

August 2021

APPROVAL PAGE

MODELING AND DESIGN OPTIMIZATION FOR MEMBRANE FILTERS

YiXuan Sun

Linda J. Cummings, Dissertation Advisor — Date
Professor of Mathematics, New Jersey Institute of Technology

Lou Kondic, Dissertation Co-Advisor — Date
Distinguished Professor of Mathematics, New Jersey Institute of Technology

---

David G. Shirokoff, Committee Member — Date
Associate Professor of Mathematics, New Jersey Institute of Technology

---

Anand U. Oza, Committee Member — Date
Assistant Professor of Mathematics, New Jersey Institute of Technology

---

Ian M. Griffiths, Committee Member — Date
Professor of Industrial Mathematics and Royal Society University Research Fellow,
University of Oxford, Oxford, UK

BIOGRAPHICAL SKETCH

Author: YiXuan Sun 孙屹轩

Degree: Doctor of Philosophy

Date: August 2021

Undergraduate and Graduate Education:

- Doctor of Philosophy in Mathematical Sciences,
  New Jersey Institute of Technology, Newark, NJ, USA (2021)
- Bachelor of Science in Nutrition and Food Science,
  University of Maryland, College Park, MD, USA (2010)
- Bachelor of Science in Chemical Engineering,
  China Agricultural University, Beijing, China (2008)

Major: Mathematical Sciences

Publications:

Y.X. Sun, L. Kondic, L.J. Cummings, "Membrane Filtration with Multiple Species of Particles." *submitted for publication.*

Y.X. Sun, P. Sanaei, L. Kondic, L.J. Cummings, "Modeling and Design Optimization for Pleated Membrane Filters." *Physical Review Fluids* (**Editors' Suggestion**), **5**, 044306, 2020.

Presentations:

Y.X. Sun, L. Kondic, L.J. Cummings, "Filtration with Multiple Species of Particles." *Poster Presentation*, **InterPore** 2021 (13th Annual Meeting), Berlin, Germany **2021**.

Y.X. Sun, P. Sanaei, L. Kondic, L.J. Cummings, "Modeling and Design Optimization for Pleated Membrane Filters (attended online)." *Oral Presentation*, **InterPore** 2020 (12th Annual Meeting & Short Courses), Qingdao, China **2020**.

Y.X. Sun, L. Kondic, L.J. Cummings, "Membrane Filtration with Multiple Species of Particles." *Abstract*, 72st Annual Meeting of the American Physical Society's **D**ivision of **F**luid **D**ynamics (**DFD**), Washington State Convention Center, Seattle, WA **2019**.

Y.X. Sun, P. Sanaei, L. Kondic, L.J. Cummings, "Modeling and Design Optimization of Pleated Membrane Filters." *Poster Presentation*, **F**rontiers in **A**pplied and **C**omputational **M**athematics (**FACM**) & The **11**th **N**ortheast **C**omplex Fluids and **S**oft Matter Workshop (**NCS** 11) NJIT, NJ **2019**.

Y.X. Sun, P. Sanaei, L. Kondic, L.J. Cummings, "Modeling and Design Optimization of Pleated Membrane Filters." *Poster Presentation*, **T**ransport in **D**isordered **E**nvironments (**TDE**) workshop, Princeton, NJ **2019**.

Y.X. Sun, P. Sanaei, L. Kondic, L.J. Cummings, "Modeling and Design Optimization for Pleated Membrane Filters." *Oral Presentation*, 71st Annual Meeting of the American Physical Society's **DFD**, Georgia World Congress Center, Atlanta, GA **2018**.

Y.X. Sun, P. Sanaei, L. Kondic, L.J. Cummings, "Optimizing the Design of Pleated Membrane Filters." *Oral Presentation*, **N**ortheast **C**omplex Fluids and **S**oft Matter Workshop 9, University of Pennsylvania, PA **2018**.

Y.X. Sun, P. Sanaei, L. Kondic, L.J. Cummings, "Optimizing the Design of Pleated Membrane Filters." *Oral Presentation*, Applied Math Days (**AMD**), Rensselaer Polytechnic Institute (**RPI**), NY **2018**.

Y.X. Sun, P. Sanaei, L. Kondic, L.J. Cummings, "Modeling of Pleated Membrane Filters with Detailed Pore Structure." *Oral Presentation*, **N**ortheast **C**omplex Fluids and **S**oft Matter Workshop 8, Columbia University, NY **2018**.

Y.X. Sun, P. Sanaei, L. Kondic, L.J. Cummings, "Investigating the Performance of Pleated Membrane Filters." *Poster Presentation*, **F**rontiers in **A**pplied and **C**omputational **M**athematics, NJIT, NJ **2017**.

献给我的母亲，舅妈，和我的老师们。
I dedicate my dissertation work to my mother ShuFang Xiao, my aunt YuQin Wu and my teachers.

ACKNOWLEDGMENT

I would like to thank my advisor Professor Linda J. Cummings and my co-advisor Professor Lou Kondic for their support and guidance for my academic endeavor, which has been eventful and memorable. I want to thank my committee members Professors David Shirokoff, Anand Oza and Ian Griffiths for providing help and feedback for my projects.

I would like to thank many great teachers who helped me get my foot into the mathematical science degree, especially Professor Denis Blackmore for many long office hours explaining details about a proof or a particular technique for computations. I also want to thank Professors Amit Bose, John Bechtold, David Shirokoff, Cyrill Muratov, and Brittany Froese Hamfeldt for making math learning fun.

I want to thank my FDA internship mentor Dr. William Limm and my undergraduate advisor Dr. Martin Lo for helping me get into the PhD program and for providing moral support for me to pursue my dreams. I am grateful to have met them during my early years of academic life.

I want to thank my mom for always believing in her son and thinking he is the best with no reasoning or logic. I want to thank my dad for giving me the courage, ambition and persistence to pursue what I want.

There are many memories I shared with colleagues and friends who helped me or whom I helped along the journey. I want to give special thanks to Tadanaga Takahash, Jacob Lesniewski, Jimmie Adriazola, Pejman Sanaei, BiNan Gu, Axel Turnquist, Ryan Howard Allaire, Brandon Behring, Valeria Barra, YiMing Yu, GuangYuan Liao, and Chao Chen for their support and suggestions about my work. I owe them a beer, and I certainly hope we get to drink together for the years to come.

I thank Dr. Thilo Simon for several helpful discussions during department tea time which led to Appendix A. I want to thank Dr. Uwe Beuscher, Dr. Zhenyu He, and Dr. Vasu Venkateshwaran of W.L. Gore & Associates for several useful discussions. I acknowledge financial support from the National Science Foundation under Grants NSF-DMS-1261596 and NSF-DMS-1615719 for this work.

Last but not the least, I thank Sherry Chhabra, Siva Kumar Valluri, Mykola Shumovskyi, JianJun Ma, the Chandra family and the Sadykov family for the friendship and fun gatherings for my past few years in New Jersey, which made the journey more colorful.

TABLE OF CONTENTS

Chapter **Page**

TABLE OF CONTENTS
(Continued)

Chapter **Page**

LIST OF TABLES

Table **Page**

LIST OF FIGURES

Figure **Page**

LIST OF FIGURES
(Continued)

Figure **Page**

LIST OF FIGURES
(Continued)

Figure **Page**

LIST OF FIGURES
(Continued)

Figure **Page**

LIST OF FIGURES
(Continued)

Figure **Page**

CHAPTER 1

INTRODUCTION

1.1 Motivation

At the most basic level, membrane filtration is a process of separation, whereby undesired/desired particles are removed/retained from a fluid suspension (known as a *feed*) by passing through a porous membrane (known as a *filter*). Membrane filters are commonly used in many applications and feature in many aspects of daily life, such as drinking water production [25], beer purification [65], vaccine purification [16], food and dietary supplement production [69], natural gas purification [44] and many more. With growing interest from both industrial and academic sectors in understanding the various types of filtration processes in use, and improving filter performance, the past few decades have seen many publications in this area, including excellent review articles that cover various aspects of membrane filtration [27, 62, 64, 66]. Nonetheless, with the majority of publications on the experimental side, simple and readily-applicable "first principles" mathematical models, which can explain and predict membrane filter performance, and guide improvements to membrane filter design, are still lacking.

Since the function of the membrane filter is to remove particles from the feed suspension, fouling of the membrane is an unavoidable part of successful filtration, and considerable research effort has been devoted to understanding the fouling mechanisms, with a view to elongating the useful life-span of a filter [7, 8, 14, 17, 24, 26, 45, 48]. Four basic fouling mechanisms have been identified in the literature (see, e.g. Grace [18] or Hermia [21]), often characterized as follows: (i) *standard* or *adsorptive blocking* (particles smaller than membrane pores enter and deposit on the wall to shrink the pores); (ii) *complete blocking* (particles larger than pores deposit at a pore entrance on the membrane surface and block the pore); (iii) *intermediate blocking* (as for

complete blocking except that pores are not completely sealed); and (iv) *cake filtration* (once the pores on the membrane surface are blocked, further particles stack up on the membrane surface, forming a "cake layer"). Useful predictive filtration models must be able to describe satisfactorily one or more of these fouling mechanisms, and therefore must account for transport and deposition of particles on or within the membrane pores, either from a continuum (track particle concentrations) or discrete (track individual particles) perspective.

Thanks to recent advances in the development of fast computational tools, numerical solution of the full Navier-Stokes equations and tracking of individual particles in the feed has become a feasible approach for modeling membrane filtration [37]. Several such computational fluid dynamics (CFD) studies, particularly focusing on particle deposition (fouling) on the membrane, have been performed [4, 37, 45, 67]. Such models may be very detailed, capable of tracking hundreds of millions of particles of arbitrary type and able to reproduce certain experimental data well. However, the computational demand for application-scale scenarios is extremely high; implementation of the CFD method is highly non-trivial and time consuming, and development of simpler models, which can treat different particle populations in an averaged sense, is desirable.

Membrane filter design can vary widely depending on the application, in terms of both internal pore structure (microscale design), and how the membrane is deployed (macroscale design). Although design improvements can be arrived at by trial and error, making prototypes and testing them can be costly and the process can be hard or impossible to systematize [64]. With this in mind, we are motivated to derive simplified mathematical models to describe the flow through and fouling of membrane filters, which can be used to evaluate filtration performance and ultimately to optimize the filter design. In this study, we focus primarily on the effect that the membrane's microstructure has on filtration performance; in particular, the effects of

varying pore size in the depth of the filter membrane. In order to keep the number of adjustable parameters to a minimum and to obtain clearer predictions for the impact of membrane design on filtration performance, we choose to focus on a single fouling mode: standard (or adsorptive) blocking.

In earlier work [51], Sanaei and Cummings proposed a simplified model for standard blocking, derived from first principles, and consistent with earlier models and experiments (e.g., Iwasaki [31] and Ison & Ives [29]). In this dissertation, we extend that work in several important ways. We study membranes of simple structure, where pores of circular cross-section connect upstream and downstream membrane surfaces directly with no branching (so-called "track-etched" type membranes [3]), and we focus on how axial variations in pore shape (in the direction transverse to the membrane) influence filtration performance. We model membrane filtration focusing on standard blocking with quantitative tracking of particle concentration in the filtrate. This model allows for evaluation of the filtration performance of a given membrane in terms of its pore shape and particle capture characteristics, and for optimization of filtration of a homogeneous feed of specified composition. We study how the feed composition, and the differences in membrane–particle interaction characteristics, affect the filtration process, and we formulate a range of relevant optimization problems to determine the optimum pore shape (within a given class of shape functions) to achieve desired filtration objectives. We also propose a new model that focuses on reactive particle removal via a chemically-active granular porous medium, with a feed containing multiple species of particles.

1.2 Outline

The remainder of this dissertation is organized as follows. In Chapter 2, we focus on membrane filtration using a pleated membrane filter with a homogeneous feed solution. In Section 2.1 we present a brief overview of the chapter, before describing

the problem setup in detail in Section 2.2. In Section 2.3, we present the detailed mathematical model, which couples the macro-scale problem of flow through a pleated porous membrane to the micro-scale problem of how particles transported by the flow are deposited within membrane pores, changing the pore structure. In Section 2.4, we formulate an optimization problem for the microscale (pore-level) membrane design, also considering the effect of inhomogeities in membrane pore structure (inevitable in membrane production), and present results; and in Section 2.5, we summarize our main conclusions and discuss some ideas for future investigation. The material presented in Chapter 2 was published in Physical Review Fluids [59].

In Chapter 3, we focus on dead-end membrane filtration (all flow perpendicular to the membrane) with feed containing multiple species of particles that have similar but differentiable physico-chemical properties. We present a brief overview of the chapter in Section 3.1 and describe the problem setup in detail in Section 3.2. We present a detailed two-species filtration model in Section 3.3 focusing attention on the filtration process within a representative pore of the membrane. We then outline a number of hypothetical filtration scenarios with two species of particles and formulate industrially-relevant optimization problems in Section 3.4. Although our optimization criteria as defined rely on simulating filtration over the entire useful lifetime of the filter (Section 3.4.3), we are able to demonstrate the feasibility of using data from the very early stages of our simulations as a reliable predictor of later behavior, offering a much faster route to optimization, discussed in Section 3.4.4. Sample optimization results are presented in Section 3.5. The material presented in Chapter 3 has been submitted for publication [58].

In Chapter 4, we focus on reactive particle removal using a chemically active porous medium (e.g., chemical coated granular material) as the filter. We describe the problem setup in Section 4.2 and propose model equations in Section 4.3. We demonstrate the model's applicability in Section 4.4 by choosing parameters that

provide a good fit to experimental data from a study by Acheampong *et al.* [1] pertaining to removal of contaminants from gold mining wastewater, which contains multiple species of toxic heavy metal ions and cyanide. Discussion of these preliminary results is provided in Section 4.5.

Finally, in Chapter 5 we summarize the main results of this dissertation, the conclusions to be drawn, and the possible directions for future work.

CHAPTER 2

MODELING AND DESIGN OPTIMIZATION FOR PLEATED MEMBRANE FILTERS

2.1 Overview

Pleated membrane filters, which offer larger surface area to volume ratios than unpleated membrane filters, are used in a wide variety of applications. However, the performance of the pleated filter, as characterized by a flux-throughput plot, indicates that the equivalent unpleated filter provides better performance under the same pressure drop. Earlier work (Sanaei & Cummings 2016 [53]) used a highly-simplified membrane model to investigate how the pleating effect and membrane geometry affect this performance differential. In this work, we extend this line of investigation and use asymptotic methods to couple an outer problem for the flow within the pleated structure to an inner problem that accounts for the pore structure within the membrane. We use our new model to formulate and address questions of optimal membrane design for a given filtration application.

2.2 Introduction

At the most basic level, membrane filtration is a process of separation, whereby undesired/desired particles are removed from a fluid suspension (known as a *feed*) by passing through a porous membrane. Membrane filters are commonly used in many applications and feature in many aspects of daily life, such as drinking water production [25], beer purification [65], vaccine purification [16], food and dietary supplement production [69], natural gas purification [44] and many more. With growing interest from both industrial and academic sectors in understanding the various types of filtration processes in use, and improving filter performance, the past few decades have seen many publications in this area, including excellent

review articles that cover various aspects of membrane filtration (see, for example, [27, 62, 64, 66]). Nonetheless, with the majority of publications on the experimental side, simple and readily-applicable "first principles" mathematical models, that can explain and predict membrane filter performance, and guide improvements to membrane filter design, are still lacking.

Since the function of the membrane filter is to remove particles from the feed suspension, fouling of the membrane is an unavoidable part of successful filtration, and considerable research effort has been devoted to understanding the fouling mechanisms (see, for example, [7, 8, 14, 17, 24, 26, 45, 48], among many others), with a view to elongating the useful life-span of a filter. Four basic fouling mechanisms have been identified in the literature (see, e.g., [18, 21]), often characterized as follows: (i) *standard* or *adsorptive blocking* (particles smaller than membrane pores enter and deposit on the wall to shrink the pores);(ii) *complete blocking* (particles larger than pores deposit at a pore entrance on the membrane surface and block the pore); (iii) *intermediate blocking* (as for complete blocking except that pores are not completely sealed); and (iv) *cake filtration* (once the pores on the membrane surface are blocked, further particles stack up on the membrane surface, forming a "cake layer").

In practice, it is rare that an entire filtration process is described well by a single fouling mechanism due to the complex composition of the feed and convoluted interaction between the feed and the porous medium (the *filter*). Often data indicate that two or more mechanisms are in operation simultaneously or sequentially (e.g., [63]), and several authors have proposed models to account for multiple fouling modes. For example, [24], [7], and [53] each proposed different models to account for two distinct fouling mechanisms; and [14] published a model to account for three sequential fouling mechanisms. In this last work [14], the pore is first constricted by small particles (standard blocking dominates); then, once the pore is sufficiently small, further particles are sieved out (complete blocking dominates); and finally a

cake layer is formed that dominates the end stage of the filtration process. For an appropriate choice of model parameters, a good agreement with experimental results was obtained.

Although inclusion of more fouling mechanisms may give a more complete picture, this comes at the expense of a larger number of model parameters that must be determined and explored. Moreover, it is often the case that a single fouling mode can dominate the majority of the filtration process, for a sufficiently simple feed. For example, [5] developed a single-mode fouling model considering only complete blocking within a membrane modeled as a layered network of pores, connected at layer junctions. Pore sizes in each layer are drawn from a probability distribution, and particle transport through the pore network also follows a specified probabilistic model, with certain (physically-motivated) restrictions. This model shows reasonable agreement with an experimental dataset. Though a very different model compared to the type we shall derive and study, it yields results that have certain features in common with ours, and we will return to this work later.

Membrane filter design can vary widely depending on the application, in terms of both internal pore structure (microscale design), and how the membrane is deployed (macroscale design). In many applications it is desirable to have a large membrane area available to maximize throughput, while simultaneously keeping the volume of the filtration unit to a minimum. *Pleated* membrane filters are commonly used to achieve this tradeoff, and these are the type of filters that we consider in this chapter (though many aspects of our modeling are more generally applicable). Pleated filters may have different geometries: some are cylindrical (see Figure 2.1(a)); while some are rectangular (Figure 2.1(b)). In most cases the membrane is sandwiched between two supporting layers and the resulting three-layer structure is folded (pleating) and fixed (e.g., via heating, [10]) to give permanence to the shape and structure of the pleated filter. Several key design factors used in characterization of pleated filters

have been identified in the literature, and a detailed description can be found in, e.g., [34], [66] and [10]. In our study, we focus on pleated filters with high *pleat packing density* (PPD), in which it is assumed that air gaps between adjacent pleats are negligible. Earlier work [53] used a highly-simplified membrane model to investigate how the pleating effect and membrane geometry affect the performance. In this work, we extend this line of investigation by using asymptotic methods to couple an outer problem for the flow within the pleated structure to a detailed inner problem that accounts for the pore structure (shape) within the membrane, and also by incorporating a model for the transport of small particles that lead to adsorptive fouling.

Although design improvements can be arrived at by trial and error, making prototypes and testing them can be costly and the process can be hard or impossible to systematize [64]. With this in mind, we are motivated to set up a simplified mathematical model to describe the flow through and fouling of pleated membrane filters, which can be used to evaluate filtration performance and ultimately to optimize the design. In this study, we focus on the effect that the membrane's microstructure has on the filtration performance; in particular, the effects of varying pore size in the depth of the filter membrane. In order to keep the number of adjustable parameters to a minimum and to obtain clearer predictions for the impact of membrane design on filtration performance, we choose to focus on a single fouling mode: standard (or adsorptive) blocking. In Section 2.3, we present the mathematical model; in Section 2.4, we formulate the optimization problem for the microscale membrane design and present results; and in Section 2.5, we summarize our conclusions and discuss some ideas for future investigation.

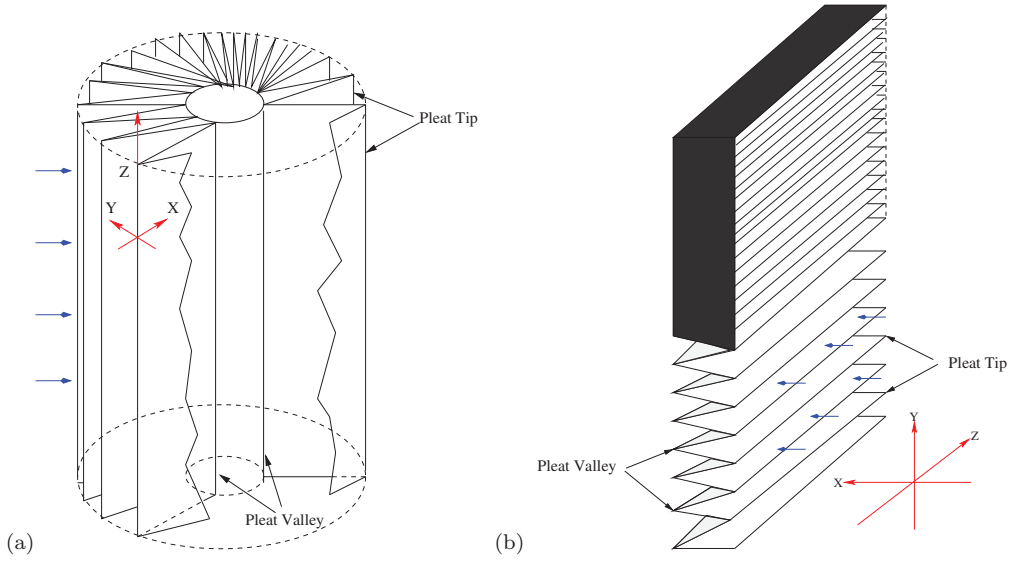

Figure 2.1 Sketches of (a) a cylindrical pleated membrane filter cartridge; (b) a rectangular pleated membrane filter cartridge. Blue arrows indicate the flow direction.

2.3 Mathematical Modeling

2.3.1 Modeling assumptions: outline

In this study, we will focus ostensibly on the rectangular pleated membrane filter, though if one neglects the curvature of the cylindrical filter cartridge then our results are quite generally applicable. As noted in the Introduction, we consider pleated filters with high pleat packing density (PPD), so that we may assume that all flow regions are occupied by either porous support material or filter membrane, with no air gaps. The *pleat tip* is defined to be the membrane fold on the inflow side, while the *pleat valley* is the fold on the outflow side. Figure 2.2 indicates how we simplify the geometry, first by neglecting dependence on the coordinate Z that runs parallel to the pleat tips/valleys; and then (if considering the cylindrical cartridge) neglecting the curvature of the cylinder. This reduces the problem to 2D in the (X, Y)-plane, where X is the direction along the pleat (from tip to valley), and Y is perpendicular to the membrane in each pleat (the azimuthal direction in the cylindrical cartridge). We further simplify by neglecting the curvature at the pleat tip and valley, which allows us to view each pleat as one of a periodic array of rectangles, indicated in the

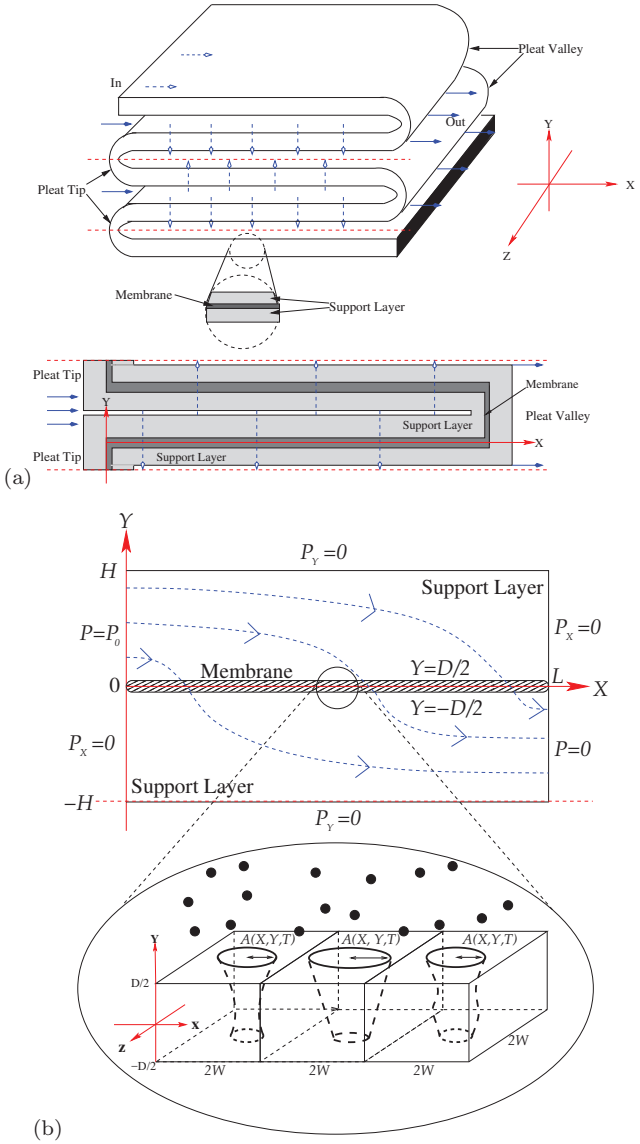

Figure 2.2 (a) Upper: Schematic, showing a few pleats. The region between the red dashed lines indicates a single complete pleat, assumed to repeat periodically. The zoom-in indicates the three-layer structure, with pale grey denoting the support layers and dark grey the membrane layer (in reality much thinner than the support layers). Blue arrows indicate the flow direction. Lower: A single pleat period, indicating how the geometry is idealized in the model, with the same color coding as the zoom-in. (b) Simplified domain (half the pleat) showing boundary conditions at inlet and outlet and schematic streamlines. Symmetry is assumed about $Y = \pm H$, and support layer plus membrane occupies the whole space (no air gap). The zoom-in shows the membrane pore morphology.

lower part of Figure 2.2(a). Symmetry of each rectangle (pleat) about the centerline ($Y = H$) is assumed, which gives our simplified half-pleat domain, indicated in Figure 2.2(b).

We assume that Darcy's law governs flow in both the support layers and the filter membrane. Both are porous media, though the support material has a much higher permeability (K) than that of the membrane (K_{m}): $K \gg K_{\mathrm{m}}$; this will be important in our asymptotic analysis later. We further assume a no-flux condition at pleat tips and valleys, justified on the basis that both the support material and the membrane there will be tightly compressed if PPD is high, so that these regions will have much higher resistance than the main length of the pleat. Support permeability K is assumed to be constant in both space and time, reflecting an assumption that fouling of support layers (which are not designed to capture particles) does not occur: the pores of these layers are much larger than those of the membrane filter. In general, however, K_{m} will vary in both time and space due to fouling: $K_{\mathrm{m}}(X, T)$. The fouling occurs on a time scale much longer than the membrane transit time for the fluid, justifying an assumption that the flow problem may be solved quasi-statically for the instantaneous membrane permeability $K_{\mathrm{m}}(X, T)$. As the fouling progresses the pore radii shrink and K_{m} decreases (as explained below), which will in turn change the pressure and velocity fields within the system.

The membrane has thickness D, the supporting layers have thickness $H - D/2$, and the length from the pleat tip to pleat valley is L (also referred to as pleat depth in the literature). The membrane occupies the region $0 \leq X \leq L$, $-D/2 \leq Y \leq D/2$, and feed passes through the pores in the negative Y-direction. In pleated filters used in applications [64], the pleat depth is much larger than the membrane and support layer thicknesses; and the membrane thickness is often much smaller than the thickness of the support layer, i.e., $L \gg H \gg D$. We assume that each pore traverses the membrane from upstream to downstream side without branching, is

contained within a square prism of dimensions $2W \times 2W \times D$, and that the membrane consists of a periodic array of such prisms (see the zoom-in Figure 2.2(b)). Pores are modeled as slender tubes of circular cross-section, whose axis coincides with that of the containing prism. The pore radius is denoted by $A(X, Y, T)$, allowing for variation in both the plane (X) and the depth (Y) of the membrane, as well as time (T) due to the fouling. This description is entirely appropriate for "track-etched" membranes (in which pores are made by etching the nuclear tracks left by radiation [3]), but may also be considered as a reasonable model for membranes with more general pore structure in a depth-averaged sense. We also assume the pore-containing prism is long and thin, i.e., $W \ll D$. The lengthscale separations $W \ll D \ll L$ justify the slender pore assumption (with slowly-varying radius in Y), as well as our assumption (implicit in the above) that pores are sufficiently numerous in the X direction that they may be considered as continuously distributed in X, with radius $A(X, Y, T)$ also continuously varying in X.

We assume the feed is a dilute suspension, which we treat as an incompressible Newtonian fluid. We denote the concentration of particles (assumed identical and much smaller than pore radii) in the fluid by C, with $C \equiv C_0$ in the inflowing feed solution. Consistent with the assumption of no fouling in the support layers, we take $C = C_0$ in the whole region $[0, L] \times [D/2, H]$; C will vary in both space and time within the membrane as adsorptive fouling occurs, as described below.

2.3.2 Governing equations

We study the case where flow through the pleated filter unit is driven by a constant pressure drop P_0, with no-flux conditions at pleat tips and valleys. With the further assumptions of periodicity and symmetry within each pleat (indicated in Figure 2.2(a) and outlined in Section 2.3.1), we can simplify the problem domain to be half of the pleat (Figure 2.2(b)), with no flux (symmetry) boundary conditions imposed at

$Y = \pm H$. Based on the assumptions set out in Section 2.1, we model the flow in both the supporting and the membrane layers with Darcy's law. The velocity $\mathbf{U} = (U, V)$ within the support layers is then given in terms of the pressure $P(X, Y)$ by

$$\mathbf{U} = (U, V) = -\frac{K}{\mu}\nabla P, \quad \nabla = (\partial_X, \partial_Y), \quad 0 \leq X \leq L,\ D/2 \leq |Y| \leq H. \tag{2.1}$$

Incompressibility of the feed solution requires

$$\nabla \cdot \mathbf{U} = 0 \quad \Rightarrow \quad \nabla^2 P = 0, \quad 0 \leq X \leq L,\ D/2 \leq |Y| \leq H, \tag{2.2}$$

within the support layers, under the stated assumption that support permeability K does not vary spatially. We have the following boundary conditions on the pressure within the support layers:

$$P^+(0, Y) = P_0,\ P_X^+(L, Y) = 0,\ P_Y^+(X, H) = 0, \tag{2.3}$$

$$P_X^-(0, Y) = 0,\ P^-(L, Y) = 0,\ P_Y^-(X, -H) = 0, \tag{2.4}$$

where we use $\pm$ superscripts to distinguish between quantities evaluated for $Y \gtrless 0$, respectively, on either side of the membrane.

As outlined in Section 2.1, we model membrane pores as a distribution of slender tubes with circular cross-section spanning the membrane, of length D and radius $A(X, Y, T)$. For our preliminary investigations, we assume that initially all pores are identical (homogeneity in the plane of the membrane), with radius varying only in the Y direction, $A(X, Y, 0) = A_0(Y)$ (note, however, that with the X-dependent pressure distribution and geometry, fouling will vary with respect to X and thus the local pore radius A will depend on X for $T > 0$). With this membrane structure, it is reasonable to assume that the Darcy flow through the membrane is approximately

unidirectional, $\mathbf{U}_\mathrm{m} = (0, V_\mathrm{m})$.[1] Incompressibility then gives $\partial V_\mathrm{m}/\partial Y = 0$, with

$$V_\mathrm{m}(X,T) = -\frac{K_\mathrm{m}}{\mu}\frac{\partial P_\mathrm{m}}{\partial Y}, \quad -D/2 \le Y \le D/2. \tag{2.5}$$

Since the pressure gradient $\partial P_\mathrm{m}/\partial Y$ is independent of Y, this equation may be rewritten as

$$|V_\mathrm{m}| = \frac{K_\mathrm{m}}{\mu D}\left[P^+\big|_{Y=D/2} - P^-\big|_{Y=-D/2}\right], \qquad 0 \le X \le L, \tag{2.6}$$

where continuity of the pressure between support layer and membrane at the membrane boundaries was used. Here, the membrane permeability K_m is related to the local pore radius A by

$$K_\mathrm{m}(X,Y,T) = \frac{\pi A^4(X,Y,T)}{32W^2}, \tag{2.7}$$

which follows from the Hagen-Poiseuille formula, see, e.g., [47] (recall that $2W$ is the size of the pore-containing period box). Continuity of flux between the support layers and membrane gives

$$|V_\mathrm{m}| = \frac{K}{\mu}\frac{\partial P^+}{\partial Y}\bigg|_{Y=D/2} = \frac{K}{\mu}\frac{\partial P^-}{\partial Y}\bigg|_{Y=-D/2}, \qquad 0 \le X \le L. \tag{2.8}$$

The (cross-sectionally averaged) velocity of the fluid within the pore, $V_\mathrm{p}(X,Y,T)$, is related to the superficial Darcy velocity within the membrane, $V_\mathrm{m}(X,T)$, by

$$4W^2 V_\mathrm{m} = \pi A^2 V_\mathrm{p}. \tag{2.9}$$

The local pore radius A (and hence the membrane permeability at that location) changes in time due to the adsorptive fouling, modeled by accounting for particle transport and deposition within pores. Following earlier work [51], we propose a

[1] For membranes that are not of this simple "track-etched" type, our additional lengthscale assumption $D \ll H \ll L$ helps justify this unidirectional flow approximation.

simple advection and deposition model for the particle concentration $C(X, Y, T)$ within pores,

$$V_{\mathrm{p}} \frac{\partial C}{\partial Y} = -\Lambda \frac{C}{A}, \quad C(X, \frac{D}{2}, T) = C_0. \tag{2.10}$$

This model comes from an asymptotic analysis of the full advection and diffusion equation for a suspension of small particles passing through a slender tube; the detailed justification can be found in [51]. The dimensional constant Λ measures the strength of attraction between the particles and the pore wall that gives rise to the deposition. The pore radius shrinks in response to the deposition: consistent with Equation (2.10) we propose

$$\frac{\partial A(X, Y, T)}{\partial T} = -\Lambda \alpha C(X, Y, T), \quad A(X, Y, 0) = A_0(Y), \tag{2.11}$$

for some constant α (proportional to the particle volume). This formulation with $A_0(Y)$ assumes that all pores in the membrane are identical initially. We will later briefly consider initial pore profiles that can vary in the X-direction also, so as to allow investigation of the possible effects of nonuniform pore size distribution in the plane of the membrane.

2.3.3 Nondimensionalization & asymptotic analysis

2.3.3.1 Nondimensionalization. In order to identify and exploit asymptotic simplifications, we introduce the following scales and dimensionless variables. Consideration of the support layers suggests the scales

$$(X, Y) = (Lx, Hy), \quad P^{\pm}(X, Y, T) = P_0 p^{\pm}(x, y, t), \tag{2.12}$$

Table 2.1 Approximate Dimensional Parameter Values [38]

Parameter	**Description**	**Typical value**
L	Length of the pleat	1.3 cm
H	Support layer thickness	1 mm
D	Membrane thickness	300 μm
W	Pore prism lateral dimension	2 μm (very variable)
P_0	Pressure drop	Depends on application
K	Support layer permeability	4×10^{-11} m^2 (very variable)
K_{m0}	Representative membrane permeability	4×10^{-13} m^2 (very variable)

Based on the Application, the Pore Size May Vary from 1 nm to 10 μm [66].

Table 2.2 Approximate Dimensionless Parameter Values (from Table 2.1)

Parameter	**Formula**	**Typical value**
ϵ	H/L	0.077
δ	D/H	0.3
Γ	$K_{\mathrm{m0}}/(K\epsilon^2\delta)$	5.53

while consideration of the membrane filter leads to the remaining scalings,

$$Y = D\tilde{y}, \qquad A(X,Y,T) = Wa(x,\tilde{y},t), \tag{2.13}$$

$$K_{\mathrm{m}}(X,Y,T) = K_{\mathrm{m0}}k_{\mathrm{m}}(x,\tilde{y},t), \qquad P_{\mathrm{m}}(X,Y,T) = P_0 p_{\mathrm{m}}(x,\tilde{y},t), \tag{2.14}$$

$$V_{\mathrm{m}}(X,T) = \frac{K_{\mathrm{m0}}P_0}{\mu D}v_{\mathrm{m}}(x,t), \qquad C(X,Y,T) = C_0 c(x,\tilde{y},t). \tag{2.15}$$

Time is scaled on the pore shrinkage timescale,

$$T = \frac{W}{\Lambda\alpha C_0}t. \tag{2.16}$$

Note that we have introduced two scaled coordinates in the Y-direction: y in Equation (2.12) and $\tilde{y}$ in Equation (2.13), relevant to the support layer and the membrane, respectively. The chosen scalings lead naturally to two dimensionless length ratios: $\epsilon = H/L$, the aspect ratio of the pleat; and $\delta = D/H$, the ratio of membrane thickness to support layer thickness. Both will be assumed small in the following: $\epsilon \ll 1$, $\delta \ll 1$ (no further assumption is needed on the relative sizes of ϵ and δ). In Equation (2.15), K_{m0} is a representative value for the initial membrane permeability. For simplicity, we choose $K_{\mathrm{m0}} = \pi W^2/32$, then Equation (2.7) gives the dimensionless membrane permeability as

$$k_{\mathrm{m}}(x,\tilde{y},t) = a^4(x,\tilde{y},t). \tag{2.17}$$

2.3.3.2 Darcy flow in supporting layers. The dimensionless governing equations and boundary conditions in the supporting layers $\delta/2 \le |y| \le 1$ are

$$\epsilon^2 p^+_{xx} + p^+_{yy} = 0, \quad \delta/2 \le y \le 1, \tag{2.18}$$

$$p^+(0,y) = 1, \quad p^+_x(1,y) = 0, \quad p^+_y(x,1) = 0, \tag{2.19}$$

$$\epsilon^2 p^-_{xx} + p^-_{yy} = 0, \quad -1 \le y \le -\delta/2, \tag{2.20}$$

$$p^-_x(0,y) = 0, \quad p^-(1,y) = 0, \quad p^-_y(x,-1) = 0, \tag{2.21}$$

where ϵ and δ are defined in Table 2.2, and we have suppressed the time dependence with the understanding that the time taken for significant fouling of the membrane to occur is much longer than that taken for fluid to transit the filter unit (note that with this assumption, the fouling is the only unsteady process in our model). This system is closed by enforcing flux continuity across the membrane, Equations (2.6) and (2.8), giving

$$p_y^+|_{y=\delta/2} = p_y^-|_{y=-\delta/2} = -\Gamma v_\mathrm{m}, \tag{2.22}$$

where the dimensionless parameter Γ, defined by

$$\Gamma = \frac{K_{\mathrm{m}0}}{K\epsilon^2\delta}, \tag{2.23}$$

captures the relative importance of the resistance (inversely proportional to the permeability) of the supporting material to that of the membrane, such that if $\Gamma \gg 1$ the supporting material provides most of the resistance whereas if $\Gamma \ll 1$ the membrane provides most of the resistance. In our analysis we assume Γ is O(1) (see Table 2.2 for a value for typical pleated filters).

2.3.3.3 Flow and fouling within the membrane.

The dimensionless equation for Darcy flow through the membrane layer, defined by $-1/2 \leq \tilde{y} \leq 1/2$, is:

$$v_\mathrm{m} = -k_\mathrm{m}\frac{\partial p_\mathrm{m}}{\partial \tilde{y}} = -a^4\frac{\partial p_\mathrm{m}}{\partial \tilde{y}}. \tag{2.24}$$

With the incompressibility condition $\partial v_\mathrm{m}/\partial\tilde{y} = 0$, and the continuity of pressure at the membrane surfaces, i.e., $p_\mathrm{m}(x, 1/2) = p^+(x, \delta/2)$ and $p_\mathrm{m}(x, -1/2) = p^-(x, -\delta/2)$, we have

$$v_\mathrm{m} = \frac{p^-(x, -\frac{\delta}{2}) - p^+(x, \frac{\delta}{2})}{\int_{-\frac{1}{2}}^{\frac{1}{2}} \frac{d\tilde{y}}{a^4}}, \tag{2.25}$$

with p^-, p^+ determined by the support layer model outlined above. Note here the use of the two different length scales, in the supporting layer ($y = Y/H$; numerator of (2.25)) and within the membrane layer ($\tilde{y} = Y/D$; denominator of (2.25)). Equation (2.10) for the particle concentration $c(x, \tilde{y}, t)$ within the membrane becomes

$$v_{\mathrm{m}} \frac{\partial c}{\partial \tilde{y}} = -\lambda a c, \quad c(x, \frac{1}{2}, t) = 1, \tag{2.26}$$

where the dimensionless deposition coefficient λ is given by

$$\lambda = \frac{\pi \mu D^2 \Lambda}{4 W K_{\mathrm{m}0} P_0}. \tag{2.27}$$

The pore radius evolution Equation (2.11) becomes

$$\frac{\partial a(x, \tilde{y}, t)}{\partial t} = -c(x, \tilde{y}, t), \quad a(x, \tilde{y}, 0) = a_0(\tilde{y}). \tag{2.28}$$

2.3.3.4 Asymptotic solution. We seek asymptotic solutions for $p^{\pm}$ in the distinguished limit $\Gamma = O(1)$, $\epsilon \ll 1$ by expanding $p^{\pm}$ in powers of ϵ as follows:

$$p^+(x, y) = p_0^+(x, y) + \epsilon^2 p_1^+(x, y) + \cdots, \quad p^-(x, y) = p_0^-(x, y) + \epsilon^2 p_1^-(x, y) + \cdots, \tag{2.29}$$

and substituting in Equations (2.18)–(2.21). This gives coupled Equations for $p_0^{\pm}$ and $p_1^{\pm}$,

$$p_{0yy}^{\pm} = 0, \tag{2.30}$$

$$p_{0xx}^{\pm} + p_{1yy}^{\pm} = 0, \tag{2.31}$$

with boundary conditions

$$p_0^+(0, y) = 1, \quad p_{0x}^+(1, y) = 0, \quad p_{0y}^+(x, 1) = 0, \tag{2.32}$$

$$p_0^-(1, y) = 0, \quad p_{0x}^-(0, y) = 0, \quad p_{0y}^-(x, -1) = 0, \tag{2.33}$$

$$p_1^+(0, y) = 0, \quad p_{1x}^+(1, y) = 0, \quad p_{1y}^+(x, 1) = 0, \tag{2.34}$$

$$p_1^-(1, y) = 0, \quad p_{1x}^-(0, y) = 0, \quad p_{1y}^-(x, -1) = 0. \tag{2.35}$$

From Equations (2.30)–(2.35), we obtain $p_0^{\pm} = p_0^{\pm}(x)$ (independent of y but still unknown), and

$$p_{1_y}^{+} = (1-y)p_{0_{xx}}^{+}, \tag{2.36}$$

$$p_{1_y}^{-} = -(1+y)p_{0_{xx}}^{-}. \tag{2.37}$$

From Equations (2.22), (2.25), (2.36) and (2.37), we obtain the following coupled system for $p_0^{\pm}$,

$$p_{0_{xx}}^{+}(x) = \frac{\tilde{\Gamma}(p_0^{+}(x) - p_0^{-}(x))}{\int_{-\frac{1}{2}}^{\frac{1}{2}} \frac{d\tilde{y}}{a^4}}, \quad p_0^{+}(0) = 1, \quad p_{0x}^{+}(1) = 0, \tag{2.38}$$

$$-p_{0_{xx}}^{-}(x) = \frac{\tilde{\Gamma}(p_0^{+}(x) - p_0^{-}(x))}{\int_{-\frac{1}{2}}^{\frac{1}{2}} \frac{d\tilde{y}}{a^4}}, \quad p_0^{-}(1) = 0, \quad p_{0x}^{-}(0) = 0, \tag{2.39}$$

where $\tilde{\Gamma} = \Gamma/(1-\delta/2)$. Note that when we further assume $\delta \ll 1$, we may drop the tilde to give the leading order system summarized in §2.3.3.5 below.

2.3.3.5 Model summary. To summarize, we have the following asymptotic model equations, valid to leading order in ϵ and δ:

$$p_{0_{xx}}^{+}(x,t) = \frac{\Gamma(p_0^{+}(x,t) - p_0^{-}(x,t))}{r_{\mathrm{m}}(x,t)}, \qquad p_0^{+}(0,t) = 1, \quad p_{0x}^{+}(1,t) = 0, \tag{2.40}$$

$$-p_{0_{xx}}^{-}(x,t) = \frac{\Gamma(p_0^{+}(x,t) - p_0^{-}(x,t))}{r_{\mathrm{m}}(x,t)}, \qquad p_0^{-}(1,t) = 0, \quad p_{0x}^{-}(0,t) = 0, \tag{2.41}$$

$$\frac{\partial c(x,\tilde{y},t)}{\partial \tilde{y}} = \frac{\lambda a(x,\tilde{y},t)c(x,\tilde{y},t)r_{\mathrm{m}}(x,t)}{p_0^{+}(x) - p_0^{-}(x)}, \qquad c(x,\frac{1}{2},t) = 1, \tag{2.42}$$

$$\frac{\partial a(x,\tilde{y},t)}{\partial t} = -c(x,\tilde{y},t), \qquad a(x,\tilde{y},0) = a_0(\tilde{y}), \tag{2.43}$$

where $r_{\mathrm{m}}(x,t)$, defined as

$$r_{\mathrm{m}}(x,t) = \int_{-\frac{1}{2}}^{\frac{1}{2}} \frac{d\tilde{y}}{a^4(x,\tilde{y},t)}, \tag{2.44}$$

represents the dimensionless membrane resistance at location x and time t. Model parameters Γ and λ are defined in Equations (2.23) and (2.27).

2.3.3.6 Method of solution. From Equations (2.40) and (2.41), we have $p_{0xx}^{+}(x,t) = -p_{0xx}^{-}(x,t)$. Integrating twice with respect to x gives an expression for p_0^- in terms of p_0^+,

$$p_0^-(x,t) = -p_0^+(x,t) + c_1(t)x + c_2(t), \tag{2.45}$$

for some $c_1(t)$ and $c_2(t)$ (which are independent of x, but vary in time as fouling occurs). By substituting Equation (2.45) into Equation (2.38) we obtain a single equation for p_0^+ containing these two arbitrary functions of time,

$$r_{\mathrm{m}}(x,t)p_{0xx}^{+}(x,t) - 2\Gamma p_0^+(x,t) = -\Gamma(c_1(t)x + c_2(t)), \tag{2.46}$$

which must be solved subject to the four boundary conditions

$$p_0^+(0,t) = 1, \quad p_{0x}^+(0,t) = c_1(t), \quad p_0^+(1,t) = c_1(t) + c_2(t), \quad p_{0x}^+(1,t) = 0. \tag{2.47}$$

Hence, with p_0^+, c_1 and c_2 determined, we have the leading-order solution for the pressure within the support layers (p_0^- can then be determined from Equation (2.45)).

To solve the equations numerically, we discretize Equations (2.42), (2.43) and (2.46) in time and space. At each time step, we need to solve Equation (2.46) subject to the boundary conditions (2.47). The initial pore profile $a_0(\tilde{y})$ is specified, so we can calculate the initial membrane resistance r_{m} defined in Equation (2.44), and hence solve Equation (2.46) at $t = 0$ to obtain the initial (leading order) pressure distribution within the support layers. With this and the initial pore profile we can solve Equation (2.42) to calculate the initial particle concentration c within the membrane, and hence solve Equation (2.43) to obtain the pore profile a at the next time step. This allows us to find the membrane resistance r_{m} at the new time step, and the above process repeats. We continue to solve the system until pore closure occurs at final time t_{f}, defined to be when the flux decreases below a preset small number.[2]

[2]In the literature, flux falling to 10% of the initial value is commonly used as a stopping criterion for filtration, on the practical grounds that a filter would be cleaned or discarded

Note that even though pore profiles are non-uniform in x during the evolution (due to the pressure gradients in x that lead to differential fouling), pore closure ultimately occurs uniformly in x along the pleat. This is because if pores at one x-location experience greater fouling at some time, the membrane resistance r_{m} at that location will be higher, so that flow is diverted to x-locations with lower resistance. These locations subsequently undergo increased fouling, leading to increased resistance. The net effect of this flow redistribution via resistance is that ultimately pores close uniformly in x along the pleat.

2.4 Results and Performance Optimization

2.4.1 Key definitions for performance evaluation

To evaluate filter performance and to carry out design optimization, we first define some key quantities:

$$\mathcal{F}(t) := \int_0^1 -v_{\mathrm{m}}(x,t)dx\,, \tag{2.48}$$

$$\mathcal{J}(t) := \int_0^t \mathcal{F}(\tau)d\tau\,. \tag{2.49}$$

$\mathcal{F}(\mathrm{t})$ is dimensionless flux, and $\mathcal{J}(\mathrm{t})$ is dimensionless throughput. We note for future reference that the dimensional flux and throughput F and J are related to their dimensionless equivalents by the following scalings, based on Equations (2.12), (2.15) and (2.16):

$$F(T) = \frac{K_{\mathrm{m0}}P_0L}{\mu D}\mathcal{F}(t), \tag{2.50}$$

$$J(T) = \frac{K_{\mathrm{m0}}P_0LW}{\alpha C_0\Lambda\mu D}\mathcal{J}(t). \tag{2.51}$$

once the flux drops to this level, see, e.g., [66]. In our simulations and optimization, for simplicity we run simulations until the dimensionless flux is close to zero (10^{-3}).

We will return to these definitions when we discuss variation of the deposition parameter λ. Following earlier work (see, e.g., [24]), we plot $\mathcal{F}$ versus $\mathcal{J}$ as one characterization of membrane performance in filtration. In our simple filtration scenario, it is desirable to keep flux high for as long as possible, while achieving a large total throughput over the filter lifetime, provided the particle removal requirement is satisfied. The instantaneous x-averaged particle concentration at the downstream side of the membrane $\tilde{y} = -1/2$, $c_{\text{avg}}(t)$, another important physical quantity when considering the particle removal capability of the membrane, is defined as:

$$c_{\text{avg}}(t) = \frac{\int_0^1 -v_{\text{m}}(x,t)c(x,-\frac{1}{2},t)dx}{\mathcal{F}(t)}. \tag{2.52}$$

This quantity represents the averaged particle concentration in the filtrate[3], sampled at any given time. We also monitor the accumulated particle concentration of the filtrate, $c_{\text{acm}}(t)$, defined as:

$$c_{\text{acm}}(t) = \frac{\int_0^t \int_0^1 -v_{\text{m}}(x,\tau)c(x,-\frac{1}{2},\tau)dxd\tau}{\mathcal{J}(t)}. \tag{2.53}$$

This quantity represents the particle concentration of the accumulated filtrate at any given time (suppose all the filtrate is collected in a well-mixed jar as the filtration progresses, then $c_{\text{acm}}(t)$ is the particle concentration of the collected filtrate in the jar at time t).

2.4.2 Formulating the optimization problem

Although we can predict the performance for any given initial pore profile distribution using our model Equations (2.40)–(2.43), a question of greater interest is to find the *optimized* pore profile for any given filtration objective and operating conditions (referred to as the objective or cost function and constraints, respectively, in the optimization literature). For our case, we consider the optimization process as finding

[3]Note that "filtrate" here refers to the feed that has passed through the filter.

the pore profile that gives *the highest total throughput* $\mathcal{J}(t_f)$ ((2.49) evaluated at t_f) while maintaining the *initial particle removal threshold* R *above a certain percentage* at time $t = 0$ ($c_{avg}(0) \leq 1 - R/100$). In our example simulations that follow, the particle removal threshold is set at $R = 99\%$, or $R = 99.9\%$.

The general optimization problem is challenging (it is in general not convex, and the searching space is infinite dimensional), even for the simple model presented here. We here present results for optimizing only within the limited class of initial pore profiles $a_0(\tilde{y})$ represented in terms of (low-degree) polynomials. We vary the coefficients of polynomials to find the values that maximize $\mathcal{J}(t_f)$ while satisfying the particle removal threshold constraint. We used the `MultiStart` algorithm with `fmincon` as local solver from the `MATLAB®` `Global Optimization` toolbox for this optimization. `MultiStart` uses uniformly-distributed or user-supplied start points within the searching domain to perform repeatedly gradient descent to find local minimizers of the cost function. The user has control over the number of searching points (start points) the `MultiStart` algorithm uses for running the local solver. After `MultiStart` reaches the stopping criterion, the algorithm creates a vector of `GlobalOptimSolution` objects, which contains the global minimum of the objective (cost) function and the minimizer that gives this global minimum (here, the optimal coefficients of the polynomial describing the pore profile). In our case, the cost function is defined as the negative of $\mathcal{J}(t_f)$ (found by evaluating Equation (2.49) at the pore closure time t_f) provided neither the particle removal threshold constraint nor the physical constraint (pore size cannot exceed the dimensions of the containing box or be negative, i.e., $0 < a \leq 1$) is violated; the cost function takes value 1 if the physical constraint is violated and it takes value 2 if the particle removal threshold

constraint is violated:[4]

$$\text{Cost function} = \begin{cases} -\mathcal{J}(t_{\mathrm{f}}) & \text{if no constraint is violated,} \\ 1 & \text{if physical constraint is violated,} \\ 2 & \text{if threshold constraint is violated.} \end{cases} \tag{2.54}$$

2.4.3 Simulation results for the optimization

Since fouling is an integral part of the filtration process, any factors that influence fouling will automatically impact the optimization. Three principal factors are identified in the literature as affecting fouling [62]: (i) *feed characteristics*, (ii) *membrane properties* and (iii) *operational conditions*. These factors are all represented in our model parameter λ (2.27), which depends on μ (feed viscosity; *feed characteristics*); Λ (the particle/pore attraction coefficient, a function of both *feed characteristics* and *membrane properties*); D, W, K_{m0} (membrane thickness, size of pore-containing box, membrane permeability; *membrane properties*); and P_0 (applied pressure drop; *operational conditions*). Larger values of λ indicate a system with superior particle capture efficiency: particles are more easily captured by the membrane compared to systems with smaller λ values. We present results for two values: $\lambda = 0.1$ and $\lambda = 1$. The model parameter Γ in Equation (2.23) also characterizes certain membrane properties, but throughout our simulations we hold its value fixed (Table 2.2).

Depending on which physical quantity induces the change in λ, see Equation (2.27), a scaling factor for the dimensionless flux and throughput, $\mathcal{F}$ and $\mathcal{J}$, may be necessary to make direct performance comparisons between simulations with different λ-values, see Equations (2.50), (2.51). For example, if a factor of 10 increase in the dimensional deposition coefficient Λ induces the change from $\lambda = 0.1$ to $\lambda = 1$, then the dimensionless flux for $\lambda = 1$ must be decreased by a factor of 10 when comparing with the dimensionless flux for $\lambda = 0.1$ to give a proper comparison. However, if

[4]The physical constraint is checked first. The threshold constraint will not be checked if the physical constraint is violated already.

λ is changed via increasing membrane thickness D and pressure P_0 by the same factor, while keeping $K_{\mathrm{m0}}P_0L/(\mu D)$ and $K_{\mathrm{m0}}P_0LW/(\mu D\alpha C_0\Lambda)$ constant, then the dimensionless plots as presented here will be a proper comparison.

Figure 2.3 shows results for the optimization procedure outlined in §2.4.2 above. Optimization is carried out for initial pore profiles $a_0(\tilde{y})$ within the classes of linear, quadratic and cubic polynomials in $\tilde{y}$ (distinguished by the linestyles), with the particle removal threshold constraint fixed at $R = 99\%$. As one would expect, increasing the order of the polynomial that describes the initial pore profile leads to increased throughput $\mathcal{J}$, since we are optimizing over a larger function class. However, gains are minimal between the quadratic and cubic cases, indicating (a) rapid convergence towards the global optimum, and (b) that optimizing over low-order polynomials (e.g., quadratics) may be sufficient for practical purposes.

Results for $\lambda = 0.1$ (blue curves), and $\lambda = 1$ (green curves) are shown, for a total of six optimized scenarios. Figure 2.3(a) shows the $\mathcal{F}$-$\mathcal{J}$ curves for the membrane with the optimized pore profiles in all six cases. Figure 2.3(b) shows a magnified version of these plots for $\lambda = 0.1$, which are difficult to distinguish in (a). We observe that for fixed particle removal threshold ($R = 99\%$), increasing the dimensionless particle retention coefficient λ gives higher total dimensionless throughput. To put these results in context, consider the two specific scenarios outlined above. In the first, if λ is changed by changing Λ, then in dimensional terms the two scenarios would give rather comparable outcomes in terms of $\mathcal{J}(t_{\mathrm{f}})$. However, the flux for the larger λ-value is always significantly higher, indicating that the filtration process would be of much shorter duration. This can be explained by the fact that a stickier membrane can remove the same fraction of particles with much larger pores, admitting a larger flux. The larger flux will lead to faster fouling, leading to a shorter filtration time to obtain the same total throughput (which in most applications would be considered desirable). In the second scenario λ is changed by changing both membrane thickness

D and driving pressure P_0 by the same factor. Here the dimensionless $\mathcal{F}$- $\mathcal{J}$ plots may be directly compared, and we see that the larger λ-value is clearly superior. Two competing factors are at play here: on the one hand driving pressure is higher, which favors higher flux; but on the other hand the increased membrane thickness imparts higher system resistance, tending to lower the flux. The increased membrane depth allows the particle removal requirement to be satisfied with considerably larger pores, however, so that the net effect of the increased pressure outweighs that of the thicker membrane, leading to much higher flux and throughput over the filtration duration.

Figures 2.3(c) and (d) show the instantaneous and accumulated particle concentrations in the filtrate, c_{avg} and c_{acm}, respectively, versus throughput $\mathcal{J}$, for the corresponding optimized membranes (note that $\mathcal{J}$ is a monotonic increasing function of time t with $\mathcal{J}(0) = 0$, so the same trends will be observed as when c_{avg} is plotted against time t). These figures confirm that the particle removal constraint is met precisely at the start of the filtration, as one would expect. However, in Figure 2.3(c) we observe that the averaged particle concentration for $\lambda = 0.1$ (blue curves) *increases* for a certain period of time before decreasing again. This concentration increase was also observed in the corresponding accumulated particle concentration plot in Figure 2.3(d). This behavior is undesirable for particle removal applications: users would like to be assured that particle retention by the membrane will not deteriorate during the course of filtration. To the best of our knowledge this phenomenon was not observed in earlier models of adsorptive fouling; however, it has been reported experimentally (e.g., [32,41]) and in models of fouling by total blocking [5]. This issue will be further discussed in the Conclusions. Observe also that the case $\lambda = 1$ leads to a much more dilute concentration of impurities in the filtrate, evidenced by the lower value of c_{acm} at the conclusion of the filtration (Figure 2.3(d)). Figures 2.3(e) and (f) show the zoom-in of the $\lambda = 0.1$ results from Figures 2.3(c) and (d), respectively, for better visibility.

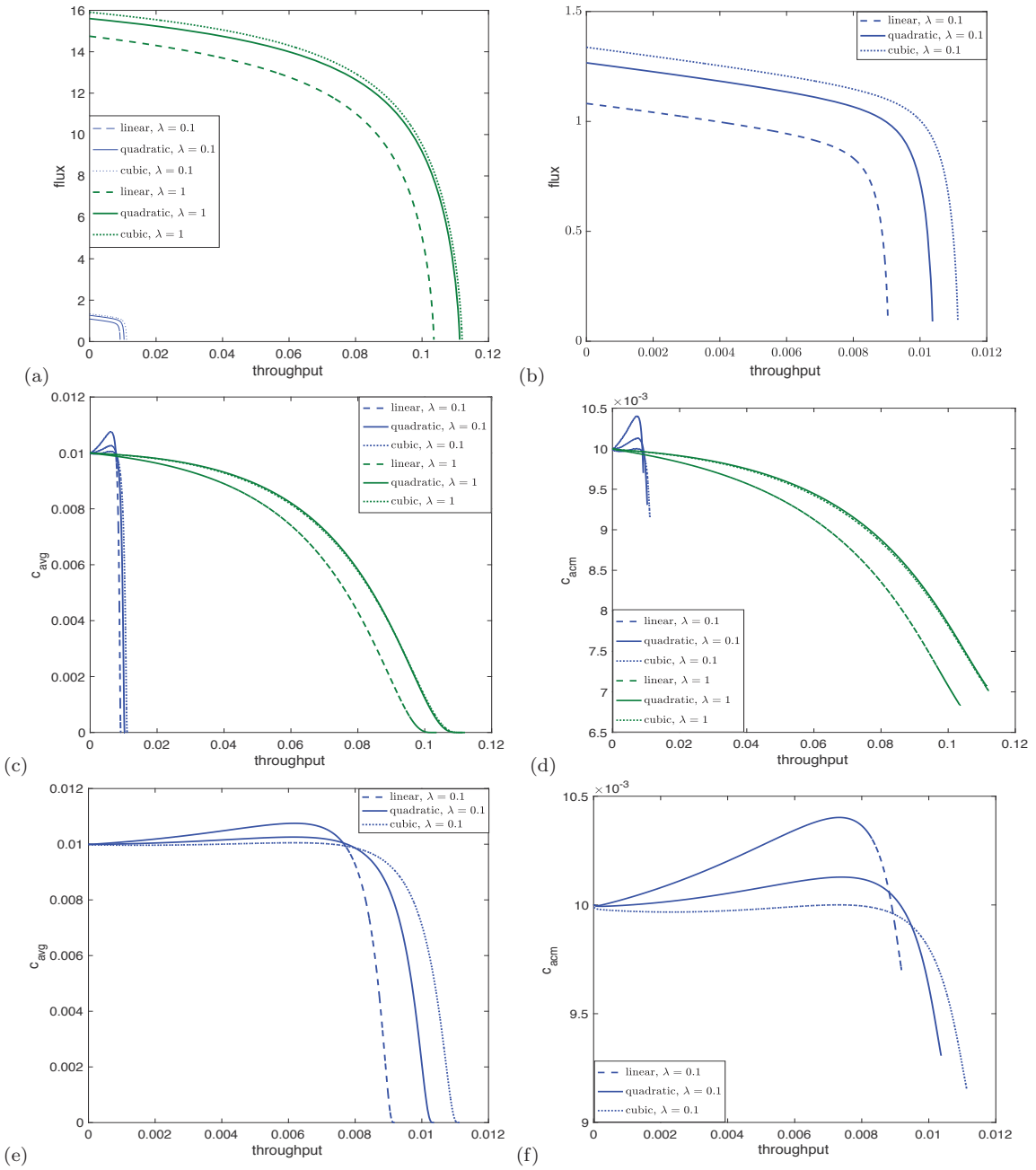

Figure 2.3 Results with particle removal threshold R fixed at 99%, $\lambda = 0.1$ in blue, and $\lambda = 1$ in green, for optimal pore profiles from the classes of linear, quadratic and cubic polynomials: (a) Flux-throughput ($\mathcal{F}$- $\mathcal{J}$) plots for all cases; (b) Zoomed flux-throughput ($\mathcal{F}$- $\mathcal{J}$) plot for $\lambda = 0.1$; (c) Instantaneous averaged particle concentration c_{avg} vs. throughput $\mathcal{J}$; (d) Accumulated average particle concentration c_{acm} vs. throughput $\mathcal{J}$; (e) Zoom of the $\lambda = 0.1$ results from (b); (f) Zoom of the $\lambda = 0.1$ results from (d).

Different applications may require different particle removal thresholds R. In Figure 2.4 we explore how changing R affects the optimized results, with λ fixed at $\lambda = 1$. Figure 2.4(a) shows the $\mathcal{F}$- $\mathcal{J}$ plots for three optimized membranes (again with pore profiles optimized over the classes of linear, quadratic, and cubic polynomials), for $R = 99\%$ (green; these curves are the same as the green curves in Figure 2.3(a)) and $R = 99.9\%$ (black). It is observed that if we insist on removing more particles ($R = 99.9\%$), we reduce the instantaneous flux and total throughput. This makes sense since the stricter requirement for particle removal (while keeping λ fixed) necessitates that pores be narrower to reduce the number of particles that can pass through the membrane, which decreases both $\mathcal{F}$ and $\mathcal{J}(t_{\mathrm{f}})$. Figure 2.4(b) shows the averaged instantaneous particle concentration c_{avg} versus throughput $\mathcal{J}$ in the filtrate for the corresponding optimized profiles, showing that again the particle removal thresholds are met precisely at $t = 0$ (the green curves for $R = 99\%$ are the same as those in Figure 2.3(c)). Figure 2.4(c) shows the zoom-in of these plots for $R = 99.9\%$, since these curves are hard to distinguish in Figure 2.4(b). This zoomed plot reveals that once again c_{avg} may increase over the course of the filtration, suggesting that a high particle retention requirement may lead to the risk of decreased particle retention capability later on. Figure 2.4(d) shows the accumulated particle concentration c_{acm} in the filtrate for the optimized profiles with the higher removal threshold $R = 99.9\%$. Again, the deterioration in particle retention over time is apparent.

For completeness, Figure 2.5 illustrates typical pore evolution during the filtration at different x-locations along the pleat, using the optimized linear pore profile obtained with $\lambda = 1$, $R = 99\%$. The evolution of six selected pores is shown, in cross-section (recall that the pores as modeled are three dimensional; see the schematic in Figure 2.2(b)). The red dashed line indicates the boundary of the pore-containing box. The blue lines in Figure 2.2(a) indicate the optimal (linear) pore walls, and in Figures 2.2(b,c,d) the increasing blue area indicates the particles that have deposited

(fouling) on the pore walls shrinking the pore radius. As explained earlier, pore closure is observed to be a self-leveling process: at the final time, all pores close simultaneously. Figure 2.5(e) shows an experimental image from a real track-etched membrane, showing good qualitative agreement with our simulations. In addition, we note that (though it may not be obvious from Figure 2.5) for simulations such as these, where there is no x-variation in the initial pore profiles, the evolving pore profiles retain symmetry about $x = 1/2$ (the point mid-way between pleat tips and valleys), with $a(x, \tilde{y}, t) = a(1 - x, \tilde{y}, t)$ for $0 \leq x \leq 1$, $-1/2 \leq \tilde{y} \leq 1/2$, $0 \leq t \leq t_{\mathrm{f}}$. In Appendix A, we demonstrate that this is true more generally, with initial pore profile distributions symmetric about $x = 1/2$ retaining this symmetry throughout the evolution.

2.4.4 Simulation results: Pore size variability

Our investigations so far have assumed that pore size does not vary along the length of the pleat, that is, all pores are initially identical (though they evolve differently in time). In practice, however, some variation of pore size is unavoidable in the process of membrane manufacture. This motivates us to explore how variation of the initial pore size distribution in the x-direction affects the filtration performance, to gain insight into the importance of membrane homogeneity in applications.

To study this in a simple and tractable way, we propose the following initial pore profile:

$$a(x, \tilde{y}, 0) = (1 + \sigma \sin(2n\pi x))\mathrm{A}(\tilde{y}), \qquad n = 1, 2, 3, \ldots, \tag{2.55}$$

in which σ and n capture the amplitude and spatial frequency of variation, respectively, and $\mathrm{A}(\tilde{y})$ is a polynomial in $\tilde{y}$ as considered previously. Note that the x-averaged pore size is the same for all cases. Before conducting any optimizations, we first explore variations of the form in Equation (2.55) in a membrane with

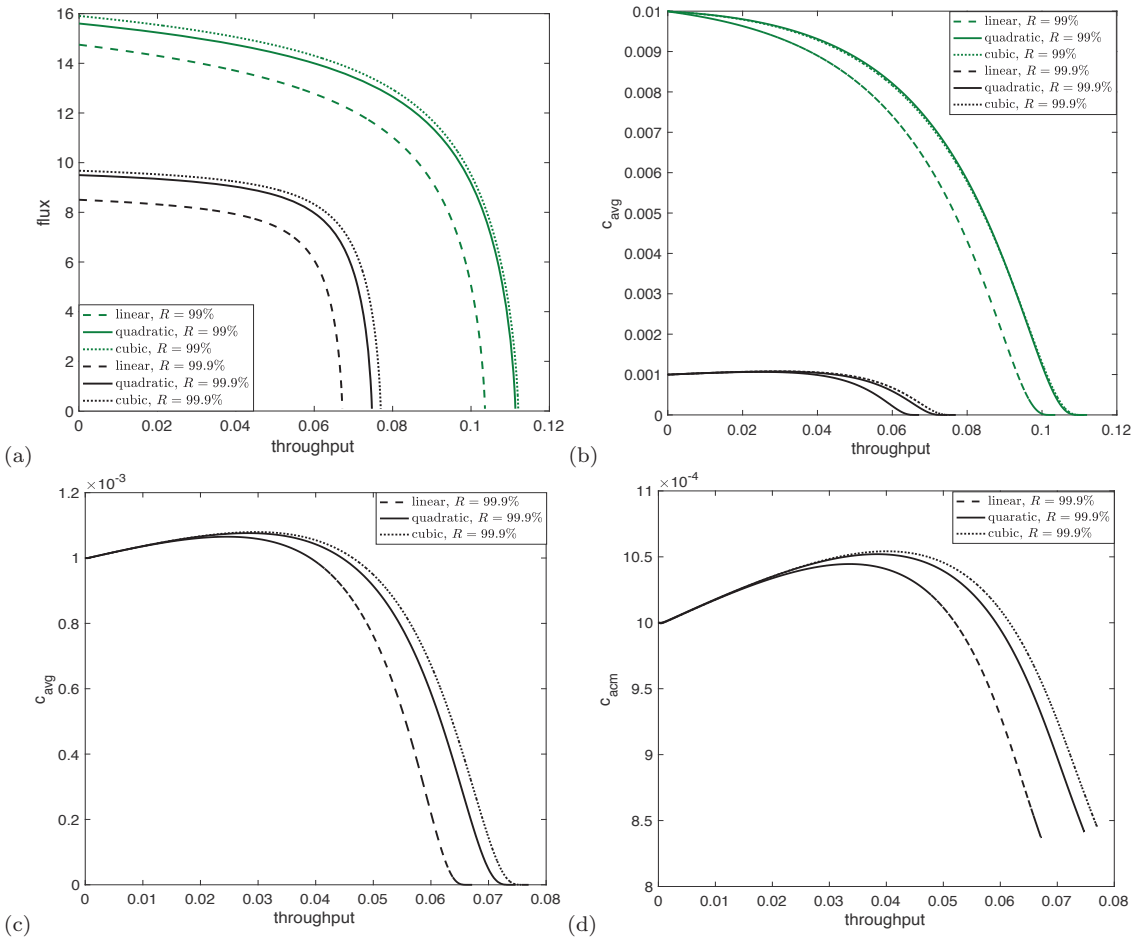

Figure 2.4 Results for membranes with optimized pore profiles from the classes of linear, quadratic and cubic polynomials, with $\lambda = 1$ and $R = 99\%$ (green curves) or $R = 99.9\%$ (black curves): (a) flux-throughput ($\mathcal{F}$- $\mathcal{J}$) plot for all cases; (b) Instantaneous averaged particle concentration c_{avg} vs. throughput $\mathcal{J}$ in the filtrate for the optimized profiles; (c) Zoom of the $R = 99.9\%$ results from (b); (d) Accumulated average particle concentration c_{acm} vs. throughput $\mathcal{J}$ in the filtrate for the optimized profiles with $R = 99.9\%$.

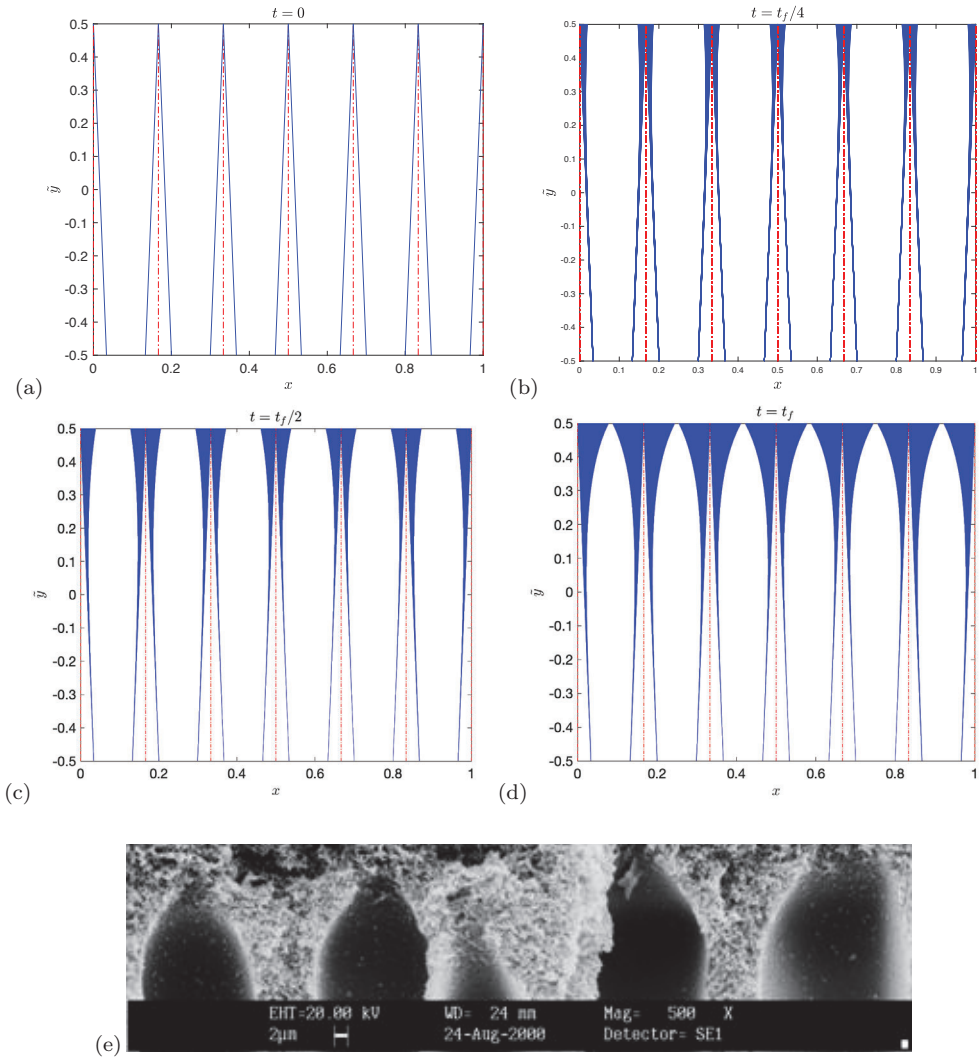

Figure 2.5 (a)–(d): Optimized linear pore profile evolution at different x-locations, with $\lambda = 1, R = 99\%$, red dashed line indicating the boundary of the prism containing each pore, and the solid blue color indicating the cumulative particle deposition on the pore wall: (a) $t = 0$, (b) $t = t_f/4$, (c) $t = t_f/2$, (d) $t = t_f$; (e) experimental result showing heavily-fouled ultrafiltration membrane in water treatment system. The black pore regions are clearly visible [56].

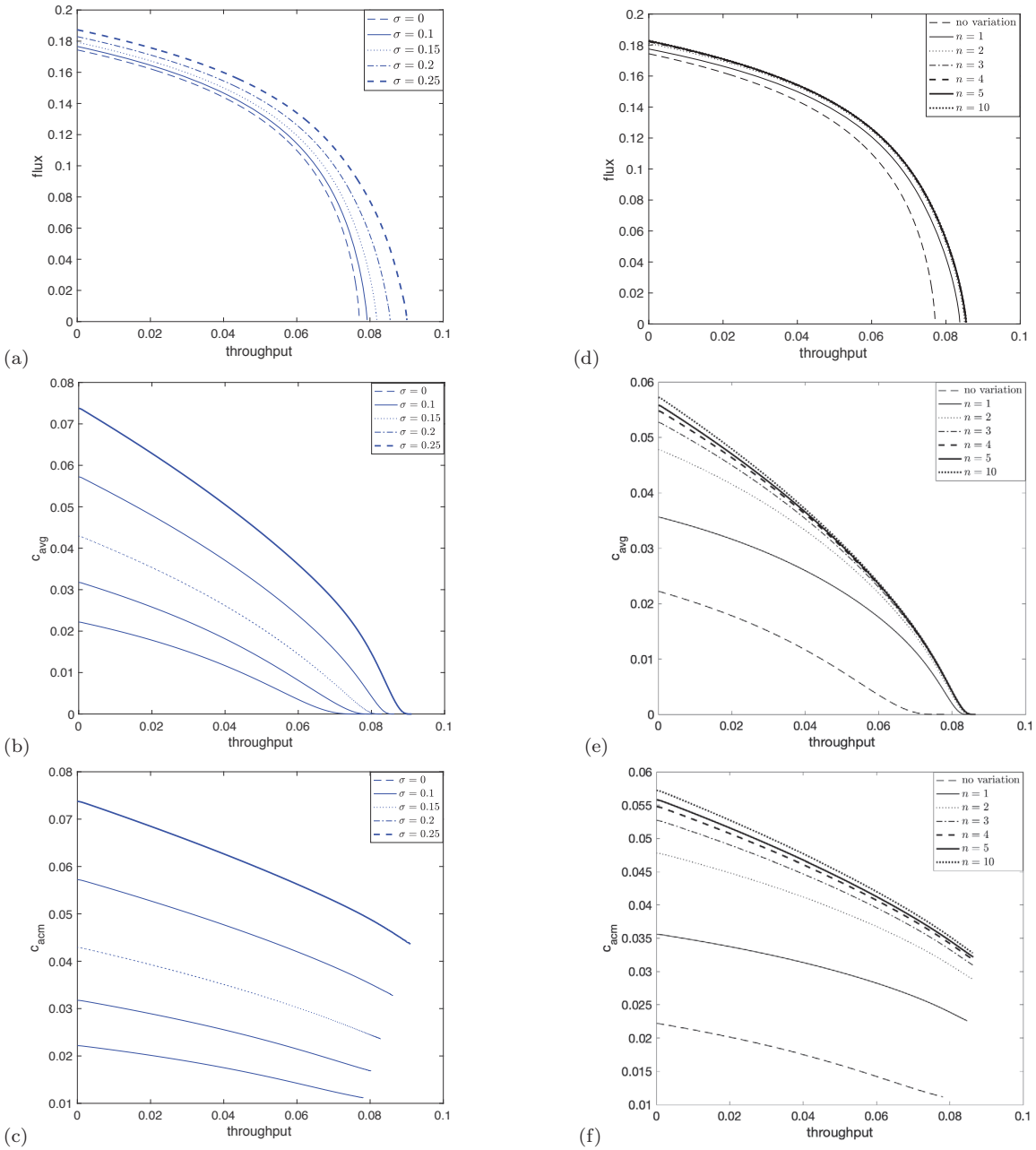

Figure 2.6 Effect of in-plane pore-size variation of the form $a(x, \tilde{y}, 0) = 0.799(1 + \sigma \sin(2n\pi x))$ with $\lambda = 1$. (a-c) illustrate variations in σ with $n = 10$: (a) flux-throughput ($\mathcal{F}$- $\mathcal{J}$) plots, (b) c_{avg} (instantaneous average particle concentration in filtrate) vs. throughput $\mathcal{J}$, and (c) c_{acm} (particle concentration in accumulated filtrate) vs. throughput $\mathcal{J}$. (d-f) illustrate variations in n with $\sigma = 0.2$: (d) $\mathcal{F}$- $\mathcal{J}$, (e) c_{avg} vs. $\mathcal{J}$, (f) c_{acm} vs. $\mathcal{J}$.

simple cylindrical pores, where A is independent of $\tilde{y}$. Figures 2.6(a,b,c) show the flux-throughput ($\mathcal{F}$-$\mathcal{J}$) graphs, and plot the average particle concentrations c_{avg}, and the accumulated particle concentrations c_{acm} versus throughput, respectively, as σ varies from 0 (uniform pores) to 0.25 (25% variations in pore sizes) with $n = 10$ and $\lambda = 1$. We take A = 0.799; this value ensures that the largest pores are (just) contained within the assumed period-box. Increasing the amplitude σ of the pore size variation increases total throughput $\mathcal{J}(t_{\text{f}})$; however, the particle concentration in the filtrate increases as well, over the entire duration of filtration. We note that the differences in $\mathcal{J}(t_{\text{f}})$, though measurable, are not highly significant as σ varies ($\mathcal{J}(t_{\text{f}})$ increases by about 20% as σ increases from 0 to 0.25); however the changes in particle concentration in the filtrate are significant: both $c_{\text{avg}}(0)$ and $c_{\text{acm}}(0)$ increase by more than 300% for the same change in σ. Figures 2.6(d,e,f) show the flux-throughput ($\mathcal{F}$-$\mathcal{J}$) graphs, and plot the average particle concentrations c_{avg}, and the accumulated particle concentrations c_{acm} versus throughput $\mathcal{J}$, respectively, as n, the spatial frequency of pore-size variations, increases (with $\sigma = 0.2$). The same trends are observed as for the variation of σ: there is a modest increase in total throughput $\mathcal{J}(t_{\text{f}})$ as n increases, and a more significant increase in the particle concentration in the filtrate. We find that for sufficiently large n ($n > 10$), its exact value is not relevant. Since the increase in $\mathcal{J}(t_{\text{f}})$ is so modest as both σ and n increase, while particle retention capability declines significantly, these results suggest that pore-size variation is unfavorable for effective filtration, and manufacturers should seek to make their membranes as uniform as possible (with respect to in-plane variations). Future work is needed to test whether this finding extends to more general pore shapes.

Although uniform pores may well be desirable, some pore-size variation is unavoidable in manufacturing, thus a natural question to ask is: if the maximum pore-size variation is known, what is the optimized pore profile that the manufacturer should aim for? Lacking detailed data on manufacturing pore-size tolerances, we

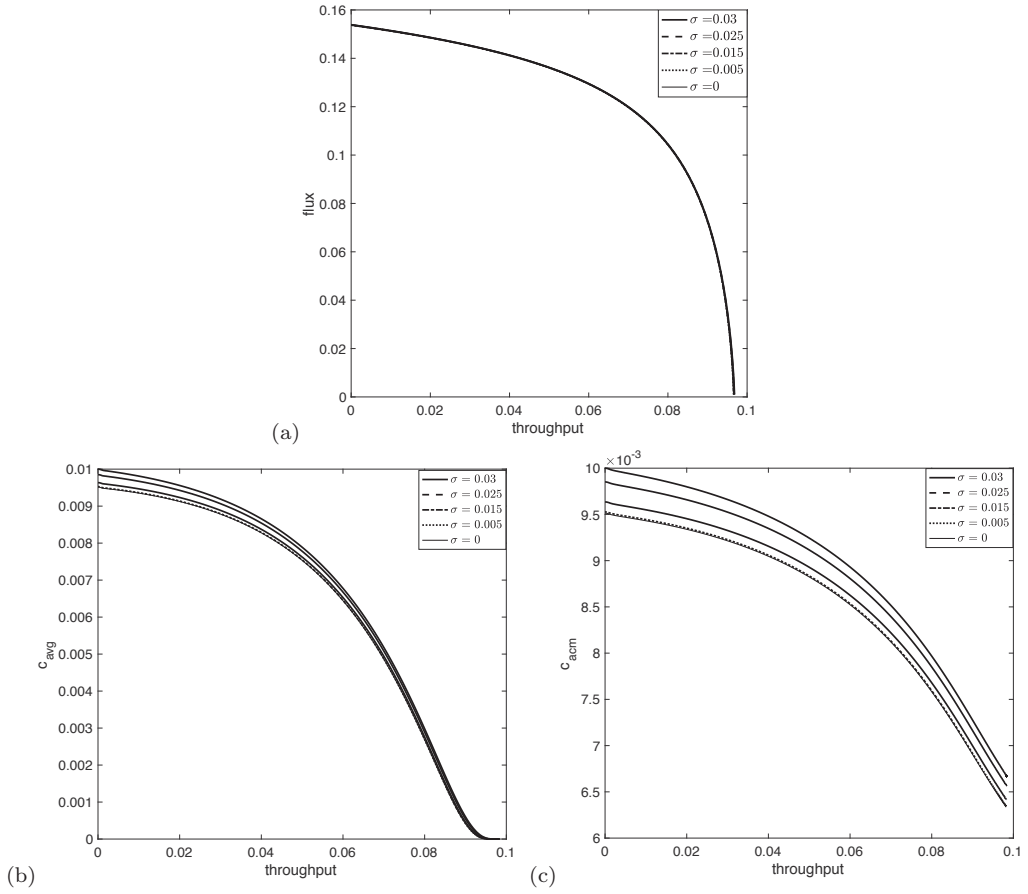

Figure 2.7 Effect of in-plane pore-size variations of the form (2.55) $a(x, \tilde{y}, 0) = \mathrm{A}(\tilde{y})(1 + \sigma \sin(2n\pi x))$. Results based on this initial pore profile, optimized with $\sigma = 0.03$, $n = 10$ and $\mathrm{A}(\tilde{y})$ linear, for $\lambda = 1$, $R = 99\%$. (a) Flux-throughput ($\mathcal{F}$-$\mathcal{J}$) plots, (b) c_{avg} vs. throughput $\mathcal{J}$, and (c) c_{acm} vs. throughput $\mathcal{J}$; for $\sigma = 0, 0.005, 0.015, 0.025, 0.03$.

present some illustrative examples. Suppose that the maximum pore-size variation is $\pm 3\%$. We set $\sigma = 0.03$ and $n = 10$ initially, in $a(x, \tilde{y}, 0)$ as given in Equation (2.55). With these parameters fixed, we then find the polynomial profiles $\mathrm{A}(\tilde{y})$ that optimize $a(x, \tilde{y}, 0)$, using the approach of Section 2.4.2. Figure 2.7 shows selected results, optimizing over linear $\mathrm{A}(\tilde{y})$ only, with the particle removal threshold R fixed at 99%: in (a,b,c) the *dashed* curves represent the *optimized* results for $\mathcal{F}$- $\mathcal{J}$, c_{avg}- $\mathcal{J}$and c_{acm}- $\mathcal{J}$, respectively, carried out for $\lambda = 1$, $n = 10$ and $\sigma = 0.03$. The remaining curves in (a-c) show results of simulations for this same optimized pore profile $\mathrm{A}(\tilde{y})$, but taking other values of $\sigma \in (0, 0.03)$ in Equation (2.55).

The flux-throughput ($\mathcal{F}$- $\mathcal{J}$) plots in Figure 2.7(a) show almost no change as σ is varied. Figures 2.7(b,c) show that, if pore size varies less than the estimated $\pm 3\%$ used for the optimization, the particle removal requirement will not be violated. Both $c_{\mathrm{avg}}(t)$ and $c_{\mathrm{acm}}(t)$ decrease as σ decreases. Figures 2.7(a-c) collectively indicate that if the manufacturer has a reliable upper bound on the in-plane pore-size variation (x-direction), they could use the optimized initial pore profile $a(x, \tilde{y}, 0)$ (varying in both x- and $\tilde{y}$-directions as per Equation (2.55)) based on this bound. As long as the bound holds, the resulting profile will yield almost the optimized total throughput, without violating the particle removal requirement. Though we here considered optimizing only over the class of linear profiles $\mathrm{A}(\tilde{y})$, results for quadratic and cubic profiles (not shown here) support the same conclusions.

In addition to in-plane variations in membrane pore size, it is equally inevitable that pores will deviate from the desired design (in both size and shape) in the depth of the membrane ($\tilde{y}$ direction). To gain some initial insight into the effects of such depth-dependent pore profile variation, we consider the following initial pore profile

$$a(x, \tilde{y}, 0) = \mathrm{A}(\tilde{y}) + \sigma \|\mathrm{A}(\tilde{y})\|_{L^1} \frac{\tilde{\mathrm{A}}(\tilde{y}, n)}{\|\tilde{\mathrm{A}}(\tilde{y}, n)\|_{L^\infty}}, \qquad n = 1, 2, 3, \ldots, \tag{2.56}$$

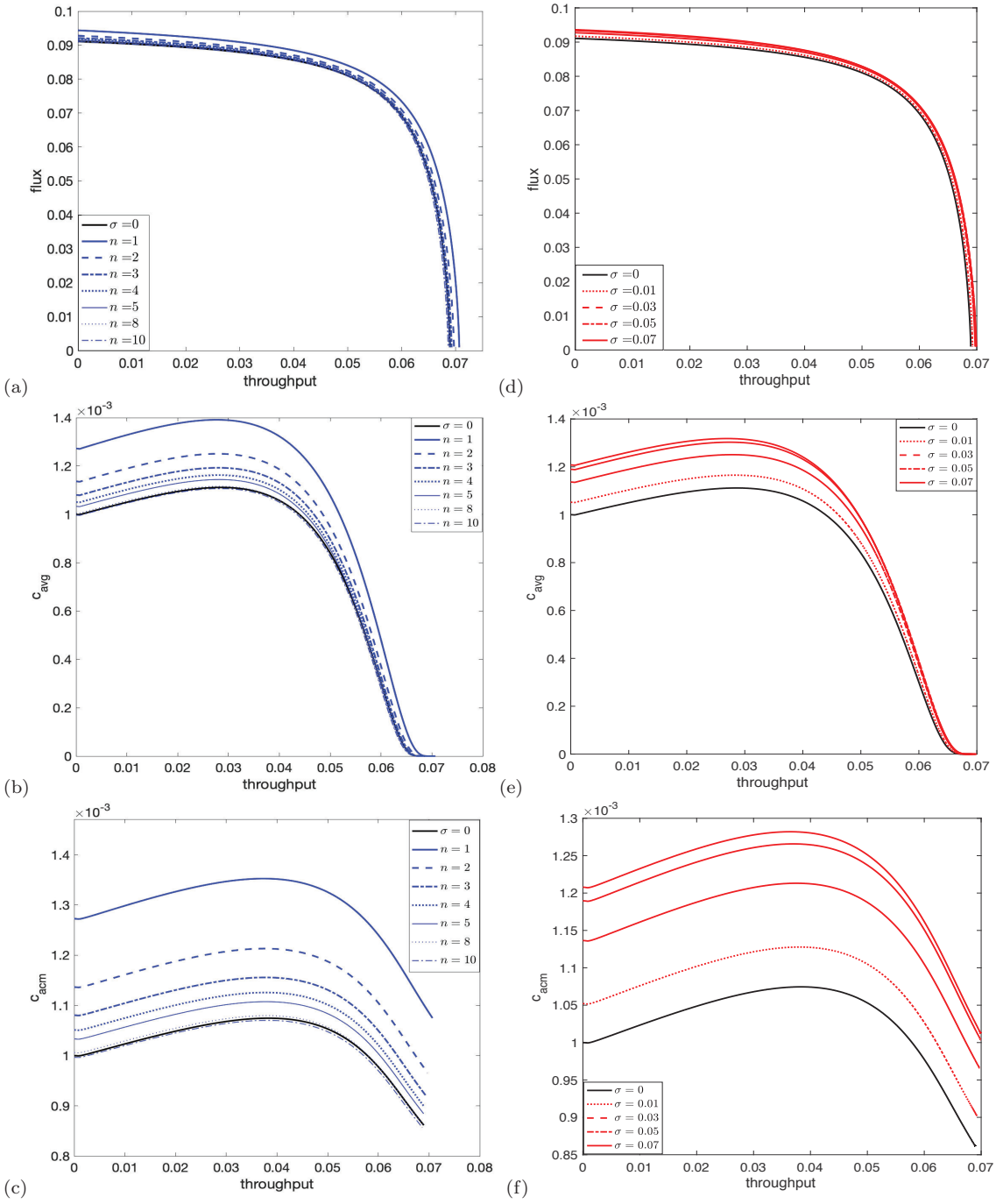

Figure 2.8 In-depth pore-size variations (2.56) $a(x,\tilde{y},0) = \mathrm{A}(\tilde{y}) + \sigma\|\mathrm{A}(\tilde{y})\|_{L^1}\frac{\tilde{\mathrm{A}}(\tilde{y},n)}{\|\tilde{\mathrm{A}}\|_{L^\infty}(n)}$: (a-c) show results with $\sigma = 0.03$, and $\mathrm{A}(\tilde{y})$ the linear optimized pore profile for $\lambda = 1$, $R = 99.9\%$. (a) Flux-throughput ($\mathcal{F}$-$\mathcal{J}$) plots, (b) c_{avg} vs. throughput $\mathcal{J}$, (c) c_{acm} vs. throughput $\mathcal{J}$, for $n = 1, 2, 3, 4, 5, 8, 10$. (d-f) show results with $n = 2$: (d) $\mathcal{F}$-$\mathcal{J}$ plots, (e) c_{avg} vs. $\mathcal{J}$, (f) c_{acm} vs. $\mathcal{J}$, for $\sigma = 0, 0.01, 0.03, 0.05, 0.07$.

in which σ and n capture the amplitude and spatial frequency of variation, $\mathrm{A}(\tilde{y})$ is a polynomial in $\tilde{y}$ as considered previously, and $\|\cdot\|_{L^1}$, $\|\cdot\|_{L^\infty}$ are the standard L^1 and L^∞ (maximum) norms, (respectively) for $\tilde{y} \in [-1/2, 1/2]$. While optimization could be carried out for higher-order polynomials, the results we present are for profiles $\mathrm{A}(\tilde{y})$ linear in $\tilde{y}$. We choose a functional form for $\tilde{\mathrm{A}}(\tilde{y}, n)$ that permits oscillations of specified wavenumber in the depth of the membrane, while preserving pore volume compared with the unperturbed "optimal" pore, which mathematically (to leading order in small pore-size perturbations σ) reduces to the constraint

$$\int_{-1/2}^{1/2} \mathrm{A}(\tilde{y})\tilde{\mathrm{A}}(\tilde{y}, n)d\tilde{y} = 0.$$

In the linear case $\mathrm{A}(\tilde{y}) = a\tilde{y} + b$, $\tilde{\mathrm{A}}(\tilde{y}, n)$ can take the form

$$\mathrm{A}(\tilde{y}, n) = \sin(4n\pi\tilde{y}) + \frac{(4n+1)a\cos((4n+1)\pi\tilde{y})}{8nb}.$$

The formulation of Equation (2.56) then incorporates the idea that the value of σ captures the percentage of pore-size amplitude variation from the unperturbed (optimized) pore profile $\mathrm{A}(\tilde{y})$ (e.g., $\sigma = 0.03$ corresponds to approximately 3% variation from $\mathrm{A}(\tilde{y})$).

Sample results are shown in Figure 2.8, where the optimization is carried out with $\lambda = 1$, and particle removal threshold $R = 99.9\%$ (the optimized result is indicated by $\sigma = 0$ in the legend). Similar to our earlier results of Figure 2.6 for in-plane pore-size variation, Figures 2.8(a,b,c) show the flux-throughput ($\mathcal{F}$-$\mathcal{J}$) graphs for each case, as well as plots of the instantaneous average particle concentrations c_{avg} and the accumulated particle concentrations c_{acm} in the filtrate versus $\mathcal{J}$, respectively, as n, the spatial frequency of pore-size variations in depth, increases (with $\sigma = 0.03$ fixed for all except the black $\sigma = 0$ curves). We find that, for n sufficiently large ($n > 8$), the effect of the variations is insignificant, with filtration performance approaching that of the unperturbed, optimal, case. In all cases, there is little effect on $\mathcal{F}$- $\mathcal{J}$

characteristics, but small values of n ($n = 1, 2, 3$) can have rather a large effect on the particle retention capability, leading to as much as 30% more particles evading capture by the membrane.

Figures 2.8(d,e,f) plot the corresponding graphs as the perturbation amplitude σ varies from 0 (no variation) to 0.07 (7% variations in pore sizes) with perturbation wavenumber fixed at $n = 2$. From Figure 2.8(d) we again observe negligible changes to the flux and throughput characteristics. Particle removal capability, however, changes by nearly 20% for a 5% perturbation of pore radius indicated by Figures 2.8(e) and (f). This suggests that particle removal capability is more sensitive to perturbations of (optimized) pore profiles in the $\tilde{y}$ direction compared to in-plane variations (see Figure 2.7 (b) and (c)), and maintaining the optimized pore shape (or more generally, the desired depth permeability gradient of the filter) will be critical to achieve the maximum total throughput while simultaneously satisfying the particle removal requirement.

2.5 Conclusion

We have formulated a simple mathematical model for evaluating the performance of a pleated membrane filter, with variable internal pore structure within the membrane. In order to obtain a model that is fast to simulate, while still capturing the permeability gradients that exist in real filtration membranes, we assume that the membrane pores are tubes of circular cross-section spanning the membrane from upstream to downstream side, and that the variation in the pore radius models the variations in permeability. Though clearly an oversimplification for many membranes, this type of geometrical pore model is frequently used in filtration modeling, and we expect our results to provide a good guide as to how average pore size should vary in the depth of the membrane.

The simplicity of our model allows for quick simulations of filtration all the way to final pore-blocking, which in turn allows us to carry out the optimization of the filter pore profile for a common filtration objective (maximizing throughput over the filter lifetime with a specified partical removal constraint that must be satisfied) and operating condition (constant pressure); see Section 2.4.2. For this filtration objective and operating condition, we are able to use our model to find (numerically) the optimal initial pore shape within a restricted class of such shapes (which, in the interest of keeping computational time relatively short, we take to be low-order polynomials in the depth of the membrane). Our results indicate that this optimization should be sufficient for most practical applications: as the degree of the polynomial increases from 1 to 3 convergence of the results (presumably to some global optimum) appears rapid. We are currently working on possible approaches to solve efficiently the general optimization problem in order to determine the optimum initial pore profile over all possible shapes.

In Section 2.4.4, we also briefly explored the impact of (unavoidable) in-plane variations and in-depth variations to the desired (optimal) pore geometry, on filtration performance. Our initial investigations indicate that, for in-plane variations our optimization techniques could still be useful if the tolerance in pore-size variation is well-characterized, and sufficiently small. However our investigation for in-depth pore-size variation indicates that particle removal can be significantly impacted by variations, and maintaining the optimized pore shape will be critical to achieve the highest total throughput $\mathcal{J}(t_{\mathrm{f}})$ while simultaneously satisfying the particle removal requirement.

One significant observation from our simulations is that, under certain conditions, the particle concentration in the filtrate may *increase* after the filtration starts — that is, particle removal capability of the membrane may actually deteriorate in the early stages of the filtration. This phenomenon, which is known to occur

experimentally [32], has not (to the best of our knowledge) been observed in earlier theoretical studies of adsorptive fouling. However, the results of [32] in fact show monotone deterioration in particle retention, unlike our results which indicate an eventual improvement in retention as significant fouling occurs. This difference indicates that additional refinements to our model may be needed.

Although we believe that our model represents a valuable step forward in helping manufacturers identify optimal membrane structures for given filtration scenarios, it does have several limitations, and there are many potential areas for improvement. First, we only consider very simple homogeneous feed solutions that contain identical particles. In most applications there will likely be multiple species in the same feed, and the objective with respect to which we optimize could also be more complicated: for example, to remove some species while allowing others to pass through. Future work will address filtration with more complex feed solutions. Second, in this work we only consider one fouling mechanism, while in practice there could be multiple simultaneous mechanisms. It would not be difficult to include multiple fouling mechanisms in our model; for example following the approach of [53]. We note, however, that the more mechanisms we include in our model, the more unknown parameters the model will have and the larger the parameter space to explore. For applications where standard blocking dominates, our model presented here should be adequate. Third, even for such applications where standard blocking dominates, there are further details that could and should be considered. For example, particles deposited on the clean membrane in the initial stages of filtration could have a shielding effect, and modify the physico-chemical interactions between particles and membrane, making it possibly more difficult for particles arriving at a later time to deposit on the membrane. Again, this is something we plan to address in our future work. Lastly, though we believe our simple "tubular pore" model should provide a good guide as to desirable membrane properties, there are certainly other types

of pore structures that could be considered, e.g., branching pore structures. Some preliminary studies may be found in [52], and we are currently undertaking more ambitious studies into how membranes with arbitrary pore networks can be efficiently modeled.

CHAPTER 3

FILTRATION WITH MULTIPLE SPECIES OF PARTICLES

3.1 Overview

Filtration of feed containing multiple species of particles is a common process in the industrial setting. In this work, we propose a model for filtration of a suspension containing an arbitrary number of particle species, each with different affinities for the filter membrane. We formulate a number of optimization problems pertaining to effective separation of desired and undesired particles in the special case of two particle species and we present results showing how properties such as feed composition affect the optimal filter design (internal pore structure). In addition, we propose a novel multi-stage filtration strategy, which provides a significant mass yield improvement for the desired particles, and surprisingly higher purity of the product as well.

3.2 Introduction

Membrane filtration is widely used in many technological applications [12, 16, 60, 65, 66, 69] and in everyday life, for instance in coffee-making and air conditioning. Fouling of the membrane by particles in the feed is unavoidable in successful filtration and understanding of the fouling mechanism(s), critical for improving filtration performance and preventing filter failure, has therefore been the target of significant research effort (see for example [27, 28, 30, 55, 62]). Extensive experimental studies [23, 31, 32, 41–43, 63] have been reported for a range of filtration scenarios, mostly focusing on a feed consisting of a single type of particle [23, 31, 32, 43, 63], though possibly with a distribution of particle sizes [41, 42]. In reality however, filtration typically involves feed containing multiple species of particles (e.g., in gold extraction from ore [1, 49], vaccine extraction [16], and other bio-product purification after fermentation [65]), which interact with the membrane differently [11, 13].

For feed containing multiple particle species, the goal may be to remove all suspended particles, but there are many applications in which the purpose of the filtration is to remove some particle species from the feed while recovering other species in the filtrate. For example, when producing vaccine by fermentation, one would want to filter the live virus out and retain the vaccine (detached protein shell of the virus, for example [68]) in the filtrate. To our best knowledge, little theoretical study has been devoted to feed containing multiple species of particles. Some experimental results are available [1, 13, 49], though the focus is mostly on the specific underlying application rather than mechanistic understanding of how the presence of different particle types affects the filtration process.

Thanks to recent advances in the development of fast computational tools, numerical solution of the full Navier-Stokes equations and tracking of individual particles in the feed has become a feasible approach for modeling membrane filtration [37]. Several such computational fluid dynamics (CFD) studies, particularly focusing on particle deposition on the membrane, have been performed [4, 37, 45, 67]. Such models may be very detailed, capable of tracking hundreds of millions of particles of arbitrary type and able to reproduce certain experimental data well. However, the computational demand for application-scale scenarios is extremely high; implementation of the CFD method is highly non-trivial and time consuming, and development of simpler models, which can treat different particle populations in an averaged sense, is desirable.

In earlier work [51], Sanaei and Cummings proposed a simplified model for standard blocking (adsorption of particles, much smaller than the filter pores, onto the internal pore walls), derived from first principles. The model assumes the pore is of slender shape, with pore aspect ratio ϵ defined as typical width W divided by the length D of the pore, $\epsilon = W/D \ll 1$, see Figure 3.1. This provides the basis for an asymptotic analysis of the advection-diffusion equation governing particle

transport within the continuum framework, valid for a specific asymptotic range of particle Péclet numbers (details can be found in [51] Appendix A). This model is in agreement with one proposed earlier by Iwasaki [31] based on experiments involving water filtration through sand beds, the validity of which was further confirmed in later experiments by Ison & Ives [29].

Building on that work [51], we recently proposed a model for membrane filtration focusing on standard blocking with quantitative tracking of particle concentration in the filtrate. This model allowed for evaluation of the filtration performance of a given membrane in terms of its pore shape and particle capture characteristics, and for optimization of filtration of a homogeneous feed containing just one type of particles [59]. In the present work we extend this approach to filtration with multiple species of particles in the feed. For simplicity, we consider dead-end filtration using a track-etched type of membrane. We study how the concentration ratio of the different types of particles in the feed, and the differences in membrane–particle interaction characteristics, affect the filtration process and we formulate optimization problems to determine the optimum pore shape (within a given class of shape functions) to achieve the desired objectives.

To illustrate our model behavior and its application for design optimization, we explore some hypothetical scenarios of practical interest, in particular: When there are two compounds A and B in a mixture, which filter design will produce the maximum amount of purified compound B before the filter is completely fouled? Questions such as this lead naturally to constrained optimization problems: how to design a filter such that a certain large fraction of type A particles is guaranteed to be removed, while retaining the maximum yield of type B particles in the filtrate, over the filtration duration?

We propose new fast optimization methods to solve these problems, based on quantities evaluated at the beginning of the filtration, which are over 10 times faster

than the method used in our earlier work [59]. Motivated by some of our findings, we also propose a new multi-stage filtration protocol, which can significantly increase the mass yield per filter of the desired compound, and simultaneously improve the purity of the final product.

Many variations on the questions we address could be proposed, and the methods we present are readily adapted to a wide range of scenarios. For brevity and simplicity, however, in the present work we focus chiefly on variants of the example outlined above to illustrate our methods. For the majority of the paper we present results for the case in which the feed contains just two particle species, noting that (within the limitations of our modeling assumptions) our model is readily extended to any number of particle species (some sample results for feed containing more than two species are included in the Appendix C).

The remainder of this paper is organized as follows. We set up our two-species filtration model in Section 3.3, focusing attention on the filtration process within a representative pore of the membrane. We then outline a number of hypothetical filtration scenarios with multiple species of particles and formulate the corresponding optimization problems in Section 3.4.1. Although our optimization criteria as defined rely on simulating filtration over the entire useful lifetime of the filter, we will demonstrate the feasibility of using data from the very early stages of our simulations as a reliable predictor of later behavior, offering a much faster route to optimization, discussed in Section 3.4.2. Sample optimization results will be presented in Section 3.5. Section 3.6 is devoted to the summary and discussion.

3.3 Filtration Modeling with Two Particle Species

In this chapter, we focus on dead-end filtration feed solution, carrying multiple different particle species, through a membrane filter. We first highlight some key modeling assumptions: we assume the particles are non-interacting (justifiable if the

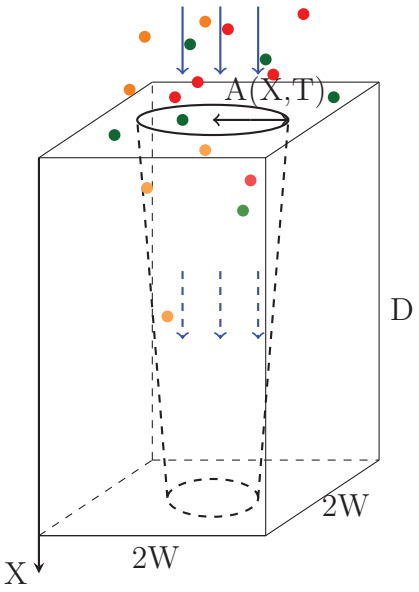

Figure 3.1 Sketch of a cylindrical pore of radius $A(X,T)$ and length D inside a square prism, representing a basic building-block of the filter membrane (our model is relevant for any other regular tesselating prism, e.g., a hexagonal or triangular prism). Blue arrows indicate the flow direction; colored dots indicate the different particle types present in the feed, and W represents the maximum possible pore radius.

feed solution is sufficiently dilute); that the particles are much smaller than the pore radius; and that the pore is of slender shape, with length much larger than its width (this is the case for "track-etched" type membranes whose pores are straight and form a direct connection between upstream and downstream sides of the membrane; see, e.g., Apel [3]). We consider only one type of fouling: the so-called standard blocking mechanism, in which particles (much smaller than pores) are adsorbed on the pore wall leading to pore shrinkage; and we inherit all the additional assumptions made in deriving the standard blocking model proposed by Sanaei and Cummings [51]. Under these assumptions, we set up our model for constant pressure and constant flux conditions, in Sections 3.3.1 and 3.3.2, respectively.

3.3.1 Solute at constant driving pressure

We consider a feed solution containing two types (different physicochemical properties) of particles, type 1 and type 2, through a planar membrane filter under constant pressure. In the presentation that follows, we use uppercase fonts to denote dimensional quantities and lower case for nondimensional quantities, which will be defined in Section 3.3.3 when we introduce appropriate physical scalings. We assume that the membrane is composed of identical pores of circular cross-section with radius $A(X,T)$ (where X is distance along the pore axis), periodically repeating in a regular (e.g., square or hexagonal) lattice arrangement. Each circular pore is contained within a regular tesselating polygonal prism, which accommodates a pore of maximum radius W ($0 < A \leq W$) and height D (see Figure 3.1 for example), where $W \ll D$. We define the representative pore aspect ratio $\epsilon = W/D \ll 1$, which will be used in our particle deposition model discussed below. The incompressible feed (assumed Newtonian with viscosity μ) flows through the pore with cross-sectionally averaged axial velocity, $U_{\rm p}(X,T)$, given in terms of the pressure $P(X,T)$ by

$$U_{\rm p}(X,T) = -\frac{K_{\rm p}(X,T)}{\mu}\frac{\partial P}{\partial X}, \tag{3.1}$$

where $K_{\rm p} = A^2(X,T)/8$ is the local permeability of an isolated pore (which follows from the Hagen-Poiseuille formula, see e.g., Probstein [47], consistent with our pore shape assumption). This is equivalent to a Darcy flow model with velocity $U(T)$ within the membrane related to $U_{\rm p}(X,T)$ via porosity $\Phi_{\rm m} = \pi A^2(X,T)/(2W)^2$,

$$U(T) = \Phi_{\rm m} U_{\rm p}(X,T) = -\frac{K(X,T)}{\mu}\frac{\partial P}{\partial X}, \tag{3.2}$$

where

$$K(X,T) = \frac{\pi A(X,T)^4}{32W^2} \tag{3.3}$$

is the membrane permeability. The flow is driven by constant pressure drop P_0 across the membrane. Conservation of mass then closes the model, giving the equation and boundary conditions governing the pressure $P(X,T)$ within the membrane as

$$\frac{\partial}{\partial X}\Big[K(X,T)\frac{\partial P}{\partial X}\Big] = 0, \qquad 0 \le X \le D, \tag{3.4}$$

$$P(0,T) = P_0, \quad P(D,T) = 0. \tag{3.5}$$

Extending the approach of Sanaei & Cummings [51], we propose the following fouling model equations, which assume that the two particle types are transported independently by the solvent and do not interact with each other:

$$U_{\mathrm{p}}\frac{\partial C_i}{\partial X} = -\Lambda_i\frac{C_i}{A}, \quad C_i(0,T) = C_{0i}, \quad i = 1,2; \tag{3.6}$$

$$\frac{\partial A}{\partial T} = -\sum_{i=1,2}\Lambda_i\alpha_i C_i, \quad A(X,0) = A_0(X), \tag{3.7}$$

where $C_i(X,T)$ is the concentration (mass per unit volume of solution) of type i particles; Λ_i is a particle deposition coefficient for type i particles; and α_i is an unknown (problem-dependent) constant, related inversely to the density of the material that comprises type i particles. Equation (3.6) follow from a systematic asymptotic analysis (based on the small parameter ϵ defined above, see also Table 3.2) of advection-diffusion equations for each particle species. Equation (3.7) assumes the rate of pore radius shrinkage (due to the particle deposition) is a linear function of the local particle concentrations at depth X, and derives from a mass-balance of the particles removed from the feed, consistent with Equation (3.6). Derivations of these results for filtration of a feed with just one particle type are given in Sanaei & Cummings [51] Appendix A and [52].

3.3.2 Solute at constant flux

Here we briefly consider how the above model is modified for the same feed solution, supplied at constant flux U_0. As fouling occurs the membrane resistance increases,

hence the driving pressure must increase to maintain the same flux through the filter. Equation (3.2) still holds for the superficial Darcy velocity, which is now held at constant value U_0 by adjusting the driving pressure $P(0,T)$, giving

$$U = U_0 = -\frac{K(X,T)}{\mu}\frac{\partial P}{\partial X}, \tag{3.8}$$

with just one boundary condition at the membrane outlet,

$$P(D,T) = 0. \tag{3.9}$$

In this case, the incompressibility condition is satisfied automatically. Equations (3.6)-(3.7) then close the model, as in the constant pressure case.

3.3.3 Non-dimensionalization

3.3.3.1 Constant pressure. We non-dimensionalize our model Equations (3.2)–(3.7) using the following scalings, with lower-case fonts indicating the dimensionless variables:

$$p = \frac{P}{P_0}, \qquad u = U\frac{32D\mu}{\pi W^2 P_0}, \qquad u_{\mathrm{p}} = U_{\mathrm{p}}\frac{32D\mu}{\pi W^2 P_0}, \tag{3.10}$$

$$c_1 = \frac{C_1}{C_{01}+C_{02}}, \qquad c_2 = \frac{C_2}{C_{01}+C_{02}}, \qquad a = \frac{A}{W}, \tag{3.11}$$

$$x = \frac{X}{D}, \qquad t = \frac{T}{T_0}, \quad \text{with} \quad T_0 = \frac{W}{\Lambda_1\alpha_1(C_{01}+C_{02})}, \tag{3.12}$$

where the chosen timescale is based on the deposition rate of particle type 1. The resulting non-dimensionalized equations are listed below: Equations (3.2)-(3.5) become

$$u = \frac{\pi a^2}{4}u_{\mathrm{p}} = -a^4\frac{\partial p}{\partial x}, \tag{3.13}$$

$$\frac{\partial}{\partial x}\left(a^4\frac{\partial p}{\partial x}\right) = 0, \tag{3.14}$$

$$p(0,t) = 1, \quad p(1,t) = 0, \tag{3.15}$$

Table 3.1 Dimensional Parameters, with Approximate Values (where known) [38]

Parameter	Description	Typical Value & Units
D	Membrane thickness	300 μm
W	Maximum possible pore radius	2 μm (very variable)
P_0	Pressure drop	unknown N/m^2
K	Representative membrane permeability	4×10^{-13} m^2 (very variable)
C_{0i}	Initial concentration of type i particles in feed	unknown kg/m^3
Λ_i	Type i particle deposition coefficient	unknown m/s
α_i	Constant related to density of type i particles	unknown m^3/kg
μ	Dynamic viscosity	unknown Pa $\cdot$ s

Depending on the Application, Pore Size may Vary from 1 nm to 10 μm [66]. The Unknown Quantities Are Variable and/or Application Dependent.

so that dimensionless permeability is just a^4 with the chosen scalings; and Equations (3.6)-(3.7) take the form

$$u_{\mathrm{p}}\frac{\partial c_1}{\partial x} = -\lambda_1\frac{c_1}{a}, \quad c_1(0,t) = \xi, \tag{3.16}$$

$$u_{\mathrm{p}}\frac{\partial c_2}{\partial x} = -\lambda_2\frac{c_2}{a}, \quad c_2(0,t) = 1-\xi, \tag{3.17}$$

$$\frac{\partial a}{\partial t} = -c_1 - \beta c_2, \; a(x,0) = a_0(x), \tag{3.18}$$

where $\lambda_i = 32\Lambda_i D^2\mu/(\pi W^3 P_0)$ is the deposition coefficient for particle type i, $\xi = C_{01}/(C_{01}+C_{02})$ is the concentration ratio between the two types of particles, $\beta = \Lambda_2\alpha_2/(\Lambda_1\alpha_1)$ is the ratio for effective particle deposition coefficients between the two types of particles, and $0 < a_0(x) \leq 1$ is the pore profile at initial time $t = 0$. The model parameters are summarized in Table 3.2 for future reference. Since we consider scenarios where particle type 1 is to be removed by filtration while type 2 should be retained in the filtrate, only values $\beta \in (0,1)$ will be considered in this chapter.

Table 3.2 Dimensionless Parameters and Descriptions (from Table 3.1)

Parameter	Formula	Description
λ_i	$32\Lambda_i D^2\mu/(\pi W^3 P_0)$	Dimensionless deposition coefficient for type i particles
ξ	$C_{01}/(C_{01}+C_{02})$	Initial concentration ratio of type 1 particles in the feed
β	$\Lambda_2\alpha_2/(\Lambda_1\alpha_1)$	Effective deposition coefficient ratio (assumes $\beta \in (0,1)$)
ϵ	W/D	Typical pore aspect ratio

To solve this system numerically, we first note that Equations (3.13)–(3.15) can be solved to give

$$u(t) = \Big(\int_0^1 \frac{1}{a^4(x,t)} dx \Big)^{-1}. \tag{3.19}$$

Given $a_0(x)$, we compute $u(0)$ via Equation (3.19), which allows us to find $u_{\mathrm{p}}(x,0)$ via Equation (3.13). We then compute $c_1(x,0), c_2(x,0)$ via Equations (3.16) and (3.17) respectively. With c_1, c_2 determined, we then compute the pore shape $a(x,t)$ for the next time step via Equation (3.18), then repeat the above process until the chosen termination condition (based on flux falling below some minimum threshold) for the simulation is satisfied.

3.3.3.2 Constant flux. Most scales follow from the constant pressure case of Subsection 3.3.3.1; here we highlight only the differences for the constant flux scenario, again with lower case fonts indicating the non-dimensionalized variables:

$$u = \frac{U}{U_0}, \qquad u_{\mathrm{p}} = \frac{U_{\mathrm{p}}}{U_0}, \qquad p = P\frac{\pi W^2}{32 U_0 D\mu}. \tag{3.20}$$

The remaining scalings are as in Equations (3.11) and (3.12), leading to the model

$$u = 1 = -a^4 \frac{\partial p}{\partial x}, \qquad p(1,t) = 0, \tag{3.21}$$

$$u_{\mathrm{p}} = \frac{4}{\pi a^2}, \tag{3.22}$$

$$u_{\mathrm{p}} \frac{\partial c_1}{\partial x} = -\lambda_1 \frac{c_1}{a}, \qquad c_1(0,t) = \xi, \tag{3.23}$$

$$u_{\mathrm{p}} \frac{\partial c_2}{\partial x} = -\lambda_2 \frac{c_2}{a}, \qquad c_2(0,t) = 1 - \xi, \tag{3.24}$$

$$\frac{\partial a}{\partial t} = -c_1 - \beta c_2, \qquad a(x,0) = a_0(x). \tag{3.25}$$

To solve these equations numerically, we proceed as in the constant pressure case, with the simplification that $u = 1$ and u_p is a known function of a, see Equation (3.22). Note that the inlet pressure $p(0,t)$ is given by

$$p(0,t) = \int_0^1 \frac{dx}{a^4(x,t)}, \tag{3.26}$$

from which it follows that, as the pore radius $a(x,t)$ decreases due to fouling, the driving pressure must increase to maintain the constant flux. We continue the simulation until the specified termination condition (based here on exhausting some fixed amount of feed, subject to a constraint on maximum inlet pressure $p(0,t)$) is reached.

3.4 Optimization

In this section, we explore the specific scenarios introduced earlier in Section 3.2 to find the optimized initial pore shape $a_0(x)$ by defining a suitable objective function $J(a_0)$ with corresponding constraints. For the purpose of the mathematical formulation of the optimization problem, we assume $a_0(x) \in C([0,1])$ (the class of real-valued functions continuous on the real interval $[0,1]$); however, for practical purposes to obtain solutions within reasonable computing time we restrict the search space for the optimizer $a_0(x)$ to low degree polynomial functions (numerical implementation

details will be given in Section 3.4.2). In addition, we require $0 < a_0(x) \leq 1$ so that the initial profile is contained within its unit prism (see Figure 3.1).

In Section 3.4.1, we define some key metrics that we use to measure the performance of the filter design and use these to set up the optimization problems. Three filtration scenarios will be studied: two under constant pressure conditions and the third under constant flux. In Section 3.4.2, we outline our optimization methods: first a "slow method" (described in Section 3.4.3) based directly on the objective function defined in Section 3.4.1 below; then we propose a "fast method" (in Section 3.4.4) based on our observations of optimizing with the slow method. We demonstrate the feasibility of using our model with fast optimization to predict and optimize for various filtration scenarios with multiple species of particles in the feed.

3.4.1 Definitions and objective functions

Adapting the approach taken in our earlier work [59], we first define some key (dimensionless) quantities that will be used to measure the performance of the membrane. We define instantaneous flux through the membrane as $u(t)$, and cumulative throughput $j(t)$ as the time integral of the flux,

$$j(t) = \int_0^t u(\tau) d\tau. \tag{3.27}$$

We denote the instantaneous concentration at the outlet ($x = 1$) for each particle type i in the filtrate, $c_i(1,t)$ as $c_{i,\text{ins}}(t)$, and the *accumulative concentrations* of each particle type i in the filtrate, $c_{i,\text{acm}}$ as

$$c_{i,\text{acm}}(t) = \frac{\int_0^t c_{i,\text{ins}}(\tau) u(\tau) d\tau}{j(t)}. \tag{3.28}$$

Let t_f denote the final time of the filtration process, when the termination condition is reached. For the constant pressure case, we define this to be when the flux drops below some specified fraction ϑ of its initial value (throughout our work here $\vartheta = 0.1$,

based on common industrial practice, see e.g., van Reis & Zydney [66]); for the constant flux case, we consider t_f to be the fixed time at which the specified amount of feed is exhausted, assuming that the terminal driving pressure $p(0, t_f)$ is less than the maximum operating pressure p_{max} for all initial pore profile functions $a_0(x)$ in the searching space considered.

To specify the particle removal requirement from the feed for each type of particles, we define the *instantaneous particle removal ratio* for type i particles, $R_i(t) \in [0, 1]$, as

$$R_i(t) = 1 - \frac{c_{i,\text{ins}}(t)}{c_i(0,t)}, \tag{3.29}$$

where $c_{i,\text{ins}}(t)$ is instantaneous concentration of particle type i at the outlet and $c_i(0,t)$ is the type i particle concentration in the feed at time t.[1] Then the initial particle removal ratio $R_i(0)$ is the fraction of type i particles removed after the feed passes through the clean filter. We also define the *cumulative particle removal ratio* for type i particles, $\bar{R}_i(t)$, as

$$\bar{R}_i(t) = 1 - \frac{c_{i,\text{acm}}(t)}{c_i(0,t)}, \qquad i = 1, 2, \tag{3.30}$$

where $c_{i,\text{acm}}(t)$ is defined in Equation (3.28). The final cumulative particle removal ratios at the end of the filtration are then $\bar{R}_i(t_f)$.

Preliminary investigations for our multi-species filtration model indicate that the particle removal capability of the filter improves, for the constant pressure scenarios, as the filtration proceeds and pores shrink, thus in our optimizations we impose the particle removal requirement only at the initial step, i.e., we require $R_1(0)$ to be greater than a specified number (R) between 0 and 1. Throughout this work

[1] In the problems that we consider $c_i(0,t) = c_{i0}$ is fixed ($c_1(0,t) = c_{10} = \xi$ and $c_2(0,t) = c_{20} = 1 - \xi$), but if we wish to consider feed with time-varying particle concentrations, then $c_i(0,t)$ in (3.30) should be replaced by appropriate averaged concentrations, $\bar{c}_i(0,t) := (\int_0^t c_i(0,\tau)u(\tau)d\tau)/j(t)$.

Table 3.3 Key Metrics Defined in Section 3.4.1 and Subsection 3.5.1.2 for Measuring Membrane Performance and Their Ranges, Values (where fixed across all simulations) or definitions

Metric	Description	Range/value/definition
$u(t)$	flux	$\in (0, \infty)$
$j(t)$	throughput	$= \int_0^t u(\tau)d\tau$
$j(t_\mathrm{f})$	total throughput at final time t_f	$= \int_0^{t_\mathrm{f}} u(\tau)d\tau$
$c_{i,\mathrm{ins}}(t)$	instantaneous concentration at the outlet for each particle type i	$= c_i(1,t) \in (0, c_i(0,t))$
$c_{i,\mathrm{acm}}(t)$	accumulative concentrations of each particle type i in the filtrate	$\in (0, c_i(0,t))$ (defined in (3.28))
$R_i(t)$	instantaneous particle removal ratio for type i particles	$\in [0,1]$
$\bar{R}_i(t)$	cumulative particle removal ratio for type i particles	$\in [0,1]$
$\tilde{R}$	desired final cumulative particle removal ratio for type 1 particles	0.99
Υ	desired fraction of type 2 particles in filtrate (effective separation)	0.5
ϑ	flux fraction at termination (constant pressure filtration)	0.1
k_i	purity for type i particles in the filtrate at the end of filtration	$\in [0,1]$
γ	effective physicochemical difference between the two species	$\in [0,1]$

we consider the desired final particle removal ratio for type 1 particles to be 0.99 and denote this fixed value by $\tilde{R}$. Other values of R are used for "intermediate" filtration stages in our description of multi-stage filtration later, with the understanding that the final goal is to reach removal ratio $\tilde{R} = 0.99$. With these definitions, for the constant pressure case, we illustrate our methods by considering a number of membrane design optimization scenarios, outlined below.

Problem 1. In many situations there are competing demands and it may be useful to consider objective functions that assign weights to different quantities of interest. Suppose we have a feed with known concentrations of type 1 and type 2 particles, where the goal is to remove type 1 particles from the feed, while retaining type 2 particles in the filtrate and simultaneously collecting as much filtrate as possible, until the termination time $t_{\mathrm{f}} := \inf\Big\{t : u(t) \leq \vartheta u(0)\Big\}$ is reached. Which filter design $a_0(x)$ – the initial pore profile, within our searching space – will remove a specified fraction $R \in [0,1]$ of type 1 particles and simultaneously maximize the objective function $J(a_0) := w_1 j(t_{\mathrm{f}}) + w_2 c_{2\mathrm{acm}}(t_{\mathrm{f}})$ (where w_1 and w_2 are weights associated to the total throughput and final cumulative concentration of type 2 particles in the filtrate, respectively)? For example, in water purification [25], type 1 particles could be toxins like lead (which we insist are removed), while type 2 particles are desirable minerals. In this application, it is of interest to retain type 2 particles, but the primary concern is to produce the purified water, so a larger value might be assigned to w_1 than w_2. This example motivates the following design optimization problem.

Optimization Problem 1

Maximize

$$J(a_0) := w_1 j(t_\mathrm{f}) + w_2 c_{2\mathrm{acm}}(t_\mathrm{f}) \tag{3.31}$$

subject to Equations (3.15)-(3.18), **and**

$$0 < a_0(x) \leq 1, \quad \forall x \in [0,1],$$

$$R_1(0) \geq R,$$

$$t_\mathrm{f} = \inf\Big\{t : u(t) \leq \vartheta u(0)\Big\}.$$

Here, we seek the optimum pore shape $a_0(x)$ to maximize $J(a_0)$, a weighted combination of $j(t_\mathrm{f})$ and $c_{2\mathrm{acm}}(t_\mathrm{f})$, subject to the flow and fouling rules dictated by our model (Equations (3.15)-(3.18)), and the physical constraints that the pore is initially contained within the unit prism (so that adjacent pores cannot overlap), and the desired user-specified fraction R of type 1 particles is removed from the feed at the start of filtration. For example, if $w_1 = 1$, $w_2 = 0$, $R = \tilde{R}$ then we are maximizing the total throughput of filtrate, with a hard constraint that at least 99% of type 1 particles are removed initially, and no concern for the proportion of type 2 particles retained in the filtrate. On the other hand, if $w_1 = 0.5$, $w_2 = 0.5$, $R = \tilde{R}$ then (assuming the dimensionless quantities $j(t_\mathrm{f})$ and $c_{2\mathrm{acm}}(t_\mathrm{f})$ are of similar magnitude) we care equally about total throughput and the proportion of type 2 particles retained in the filtrate, again with a hard constraint on removal of type 1 particles.

Problem 2. Suppose we have a large quantity of feed containing known concentrations of type 1 and type 2 particles, where the goal is to remove type 1 particles and collect the maximum quantity of type 2 particles in the filtrate (e.g., for vaccine production after fermentation, one would want to filter out the live virus – type 1 particles – and retain as much vaccine – type 2 particles – as possible in

the filtrate), until the termination time t_f is reached. Which filter design $a_0(x)$, within our searching space, will remove a specified fraction $R \in [0,1]$ of type 1 particles and simultaneously maximize the final yield of type 2 particles in the filtrate, $c_{2acm}(t_f)j(t_f) =: J(a_0)$? This question leads to the following design optimization problem.

Optimization Problem 2

Maximize

$$J(a_0) := c_{2acm}(t_f)j(t_f) \tag{3.32}$$

subject to Equations (3.15)-(3.18), **and**

$$0 < a_0(x) \leq 1, \quad \forall x \in [0,1],$$
$$R_1(0) \geq R,$$
$$t_f = \inf\Big\{t : u(t) \leq \vartheta u(0)\Big\}.$$

Here we seek the optimum $a_0(x)$ that maximizes objective function $J(a_0)$, representing the final mass of type 2 particles in the filtrate, subject to the flow and fouling rules of our model, the physical constraints, and the desired particle removal requirement.

For the case in which constant flux through the filter is specified, we consider the following illustrative scenario:

Problem 3. Given a fixed amount of feed, what is the best filter design to maximize the yield of a purified compound of interest (e.g., gold in mining [39], vaccine extraction [16] or other bio-product purification), while removing an impurity? In this scenario, we consider the optimization problem as finding the initial pore profile $a_0(x)$ such that the filter removes a certain proportion (R) of type 1 particles from the feed, while maximizing the amount of type 2 particles collected in the filtrate,

until the feed is exhausted, i.e., the termination time t_f is reached. This problem statement motivates the following optimization problem:

Optimization Problem 3

Maximize

$$J(a_0) := c_{2\text{acm}}(t_f) j(t_f) \tag{3.33}$$

subject to Equations (3.21)-(3.25), **and**

$$0 < a_0(x) \leq 1, \quad \forall x \in [0,1],$$

$$R_1(0) \geq R,$$

t_f specified (time at which feed is exhausted).

The objective function $J(a_0)$ in Equation (3.33) represents choosing the optimum $a_0(x)$ to maximize the final mass of purified type 2 particles obtained at the end of the filtration.

3.4.2 Optimization methodology overview

The design optimization problems outlined above are mathematically challenging and computationally expensive in general due to non-convexity [9] (of both the objective function and the constraints), large number of design variables (in our case the number of possible design variables is infinite, as our searching space for the pore shape $a_0(x)$ is the infinite-dimensional function class $C([0,1])$) and the computational cost of evaluating the objective function (which requires that we solve the flow and transport equations until the termination time t_f). For simplicity and efficiency, we therefore restrict our searching space for $a_0(x)$ to be (low degree) polynomial functions, the coefficients of which represent our design variables (the class of searchable functions could be expanded without difficulty but with commensurate increase in computational cost). In the following two subsections, we outline our

two optimization routines: first the slow method, which arises naturally from the problems posed and which relies on running many simulations over the entire lifetime of the filter; then the proposed new fast method, which uses data from only the very earliest stages of filtration to predict the optimum over the filter lifetime. The two methods are compared in Section 3.5.

3.4.3 Slow method

We vary the coefficients of polynomials $a_0(x)$ to find the values that maximize the objective functions defined in **Problems 1-3**, under the constraints specified in each case. The polynomial functions in this case are referred to as shape functions in the shape optimization literature [61]. In the interests of reducing computation time, for the purpose of the demonstration simulations presented here, we restrict our searching space to be the linear pore profile, i.e., we consider initial profiles of the form $a_0(x) = d_1x + d_0$, where d_1, d_0 are the design variables to be optimized for each specific scenario, with searching range for $(d_1, d_0) \in [-1, 1] \times [0, 1]$. We use the `MultiStart` method with `fmincon` as local solver from the `MATLAB®` `Global Optimization` toolbox for this optimization. Since the routine finds a minimizer while we want to maximize $J(a_0)$, we work with the cost function $-J(a_0)$; more details of the implementation of the cost function and constraints can be found in our earlier work [59].

We specify a starting point $(d_1^0, d_0^0) \in [-1, 1] \times [0, 1]$ (initial guess for running the local solver `fmincon`), cost function (based on our objective functions and constraints), design variable searching range, and number of searching points n (the number of points in (d_1, d_0)-space that will be explored) for the `MultiStart` method. With the user-specifed starting point (d_1^0, d_0^0), an additional $(n-1)$ starting points $(d_1^i, d_0^i) \in [-1, 1] \times [0, 1], i = 1, 2, ...n-1$ are generated by the `MultiStart` algorithm. The resulting n points are then used to run the local solver `fmincon` (based on a

gradient descent method) to find a list of local minimizers. We use the best minimizer from the list as the coefficients for our optimized linear pore profile. Note that there is no guarantee the method will find the global minimizer due to the nature of gradient descent methods applied to non-convex problems (the result found depends on the starting-points); however, local minimizers can be systematically improved and for practical purposes may be useful if they provide significant improvement over current practice (see e.g., the study by Hicks *et al.* on airfoil design [22]). Simulations using this method are presented in Figures 3.2, 3.3, 3.4, 3.5, described in Section 3.5 later.

3.4.4 Fast method

The "slow" optimization method described above is straightforward and easy to implement, but reliable results require that many (n large) individual model simulations be run through to the termination time t_{f}. The results presented in this chapter are restricted to optimizing membrane structure within the class of linear pore profiles only, but in any real application it may be desirable to optimize over wider function classes, e.g., polynomials of higher order. We find (empirically) that each unit increase of the degree of polynomial $a_0(x)$ requires roughly a 10-fold increase in the number of searching points to reach the best local optimum, with a corresponding increase in the run time. Run time will also increase if more than two particle species are considered, or if some of the constraints are removed or inactive (e.g., a less strict particle removal requirement) and the feasible region becomes very large. Maximum computational efficiency in practical situations is therefore critical. Motivated by the idea that imposing carefully-chosen conditions on the initial state of a system can, in many cases, guarantee certain features of later states, we propose a fast method based on simulations of the very early stages of filtration. We note that similar ideas have been used to estimate filter capacity (the total amount of feed processed during

a filtration) using a method called $V_{\max}$, which essentially predicts the filter capacity using only the first 10-15 minutes of filtration data [70].

Extensive preliminary simulations for **Problem 1** with $w_2 = 0$ [2] indicate that the $(u(t), j(t))$ flux-throughput graph at optimum is initially flatter and higher (see Figure 3.3(a) for example), with small gradient $|u'(0)|$ and large vertical intercept $u(0)$, in comparison with graphs for sub-optimal solutions. Moreover, fouling shrinks the pore and increases resistance, thus flux decreases in time and $u'(0) < 0$ for all model solutions. We therefore expect that, at optimum, $u(0)$ should be as large as possible and $u'(0)$ as close to zero as possible. Similar ideas apply to the case $w_2 > 0$, where we wish also to maximize $c_{2\text{acm}}(t_\text{f})$, the cumulative concentration of type 2 particles in the feed at the final time: we propose instead to maximize a function based on the initial state of the system as characterized by $c_{2\text{ins}}(0)$ and $c'_{2\text{ins}}(0)$ (respectively the initial concentration and initial concentration gradient, with respect to t, of type 2 particles at the membrane outlet $x = 1$). Again, preliminary simulations indicate that at optimum $c'_{2\text{ins}}(0)$ is close to zero and negative,[3] while $c_{2\text{ins}}(0)$ is large, compared to sub-optimal solutions. With these observations, we expect to maximize $c_{2\text{acm}}(t_\text{f})$ by insisting on high initial instantaneous concentration $c_{2\text{ins}}(0)$ and small initial gradient $c'_{2\text{ins}}(0)$.

With these motivations, we now define modified objective functions for our fast method. In place of (3.31) in Optimization **Problem 1**, we propose the following fast objective function, which uses data from only the initial stage of the model solution:

$$J_{1,\text{fast}}(a_0) = w_1 u(0) + w_1 u'(0) + w_2 c_{2\text{ins}}(0) + w_2 c'_{2\text{ins}}(0), \tag{3.34}$$

[2] In which we optimize for total throughput only in constant pressure-driven flow for two particle species with $\lambda_1 = 1$, $\beta \in (0.1, 0.9)$ and $\xi \in (0.1, 0.9)$, using the slow method outlined above.

[3] The occasional increase in particle concentration at the membrane outlet that was observed at early times in our previous work [59] for single-particle-species filtration was never seen here.

in which the terms in w_1 act to maximize total throughput and those in w_2 maximize concentration of type 2 particles in the filtrate, where w_1 and w_2 can be tuned depending on the relative importance of the two quantities. Note that the weights assigned to $u(0)$ ($c_{2\text{ins}}(0)$) and $u'(0)$ ($c'_{2\text{ins}}(0)$) do not have to be the same; we could allow four independent weights for the four quantities in (3.34). However, for the simple application scenarios we considered we found just two independent weights w_1, w_2 to be sufficient to give reliable results in an efficient manner.

To replace (3.32) in Optimization **Problem 2**, we propose the following fast objective function

$$J_{2,\text{fast}}(a_0) = u(0)c_{2\text{ins}}(0), \tag{3.35}$$

in which $u(0)c_{2\text{ins}}(0)$ captures the initial collection of the particle 2 in the filtrate. Other "fast" objective functions involving $u'(0)$ and $c'_{2\text{ins}}(0)$ were tested, but found to confer no improvements, hence we opt for the simplest effective objective function.

In the following section, we demonstrate that our fast optimization method always gives results at least as good as those for the slow method, and then use it to investigate various model features and predictions.

3.5 Results

In this section, we present our simulation results for a few two-species filtration scenarios. We focus on the effects of ξ, the concentration ratio of the two particle types in the feed, and $\beta = \Lambda_2\alpha_2/(\Lambda_1\alpha_1)$, the ratio of the effective particle deposition coefficients for the two particle types (both these parameters are unique to multi-species filtration, having no counterparts in single-species models). For most of our simulations, we fix $\lambda_1 = 1$ (particle type 1 has fixed affinity for the membrane throughout) and the initial fraction of type 1 particles to be removed is fixed at $\tilde{R}$. In Section 3.5.1, we first present sample comparison results between the fast and slow

methods for **Problem 1** and **Problem 2**, noting that many more tests than are presented here were conducted to verify that the fast method reliably finds optima as good as or superior to those found by the slow method, under a wide range of conditions. We then use the fast method to study the effects of varying parameters β and ξ for several two-species filtration scenarios under constant pressure conditions. Based on the results of studying these parameters, we propose a multi-stage filtration strategy that will increase the mass yield of particle we wish to recover in Section 3.5.1.2. We present sample results for the constant flux case in Section 3.5.2, focusing on **Problem 3**.

3.5.1 Optimization of constant pressure filtration

3.5.1.1 Demonstrating the efficacy of the fast optimization method. We begin by demonstrating both slow and fast optimization methods described in Section 3.4.2 above. Figure 3.2 shows the fouling evolution of the optimized membrane pores $a_0(x)$ for **Problem 1** with $w_1 = 1, w_2 = 0, \xi = 0.5, \beta = 0.1, \alpha_1 = \alpha_2, \lambda_1 = 1$, and $R_1(0) \geq \tilde{R}$, using the slow method (left panel) and fast method (right panel). The top row shows the clean, unfouled optimized pore profiles at $t = 0$ (Figures 3.2 (a) and (d)); the center row shows the fouling of these pores at $t = t_f/2$ halfway through the filtration (Figures 3.2 (b) and (e)); and the bottom row shows the fouled pores at termination time $t = t_f$ (Figures 3.2 (c) and (f)). The gray region is the filter material, and the dark blue color indicates the fouling (region occupied by deposited particles). The white area denotes the open pore (void), and the red center line is the axis of symmetry of the pore (which has circular cross-section). This figure illustrates that the optima $a_0(x)$ found by fast and slow methods are indistinguishable.

Figure 3.3 further compares the slow method (objective function (3.31), dashed curves) and the corresponding fast method (objective function (3.34), dotted curves) for **Problem 1**, with various weights $[w_1, w_2]$ indicated in the legend (recall that

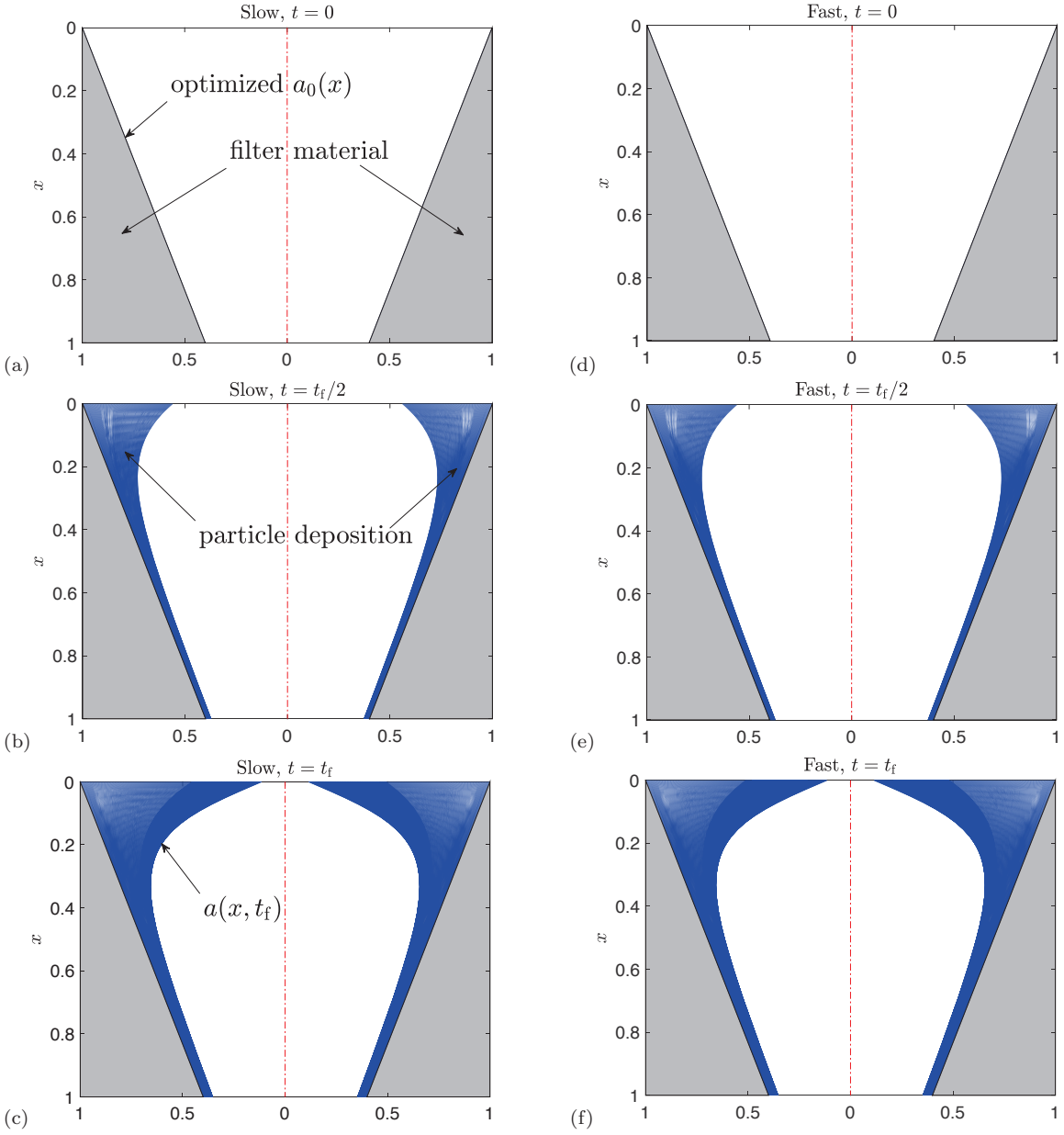

Figure 3.2 Fouling evolution of the optimized membrane pore $a_0(x)$ for **Problem 1** with $w_1 = 1, w_2 = 0, \xi = 0.5, \beta = 0.1, \alpha_1 = \alpha_2, \lambda_1 = 1$; (a-c) show evolution for $a_0(x) = -0.6001x + 0.9998$ optimized using slow method and (d-f) show evolution of $a_0(x) = -0.6002x + 0.9999$ for the corresponding fast method, at $t = 0$ (unfouled; (a) and (d)), $t = t_f/2$ (halfway through filtration; (b) and (e)) and $t = t_f$ (end of filtration; (c) and (f)).

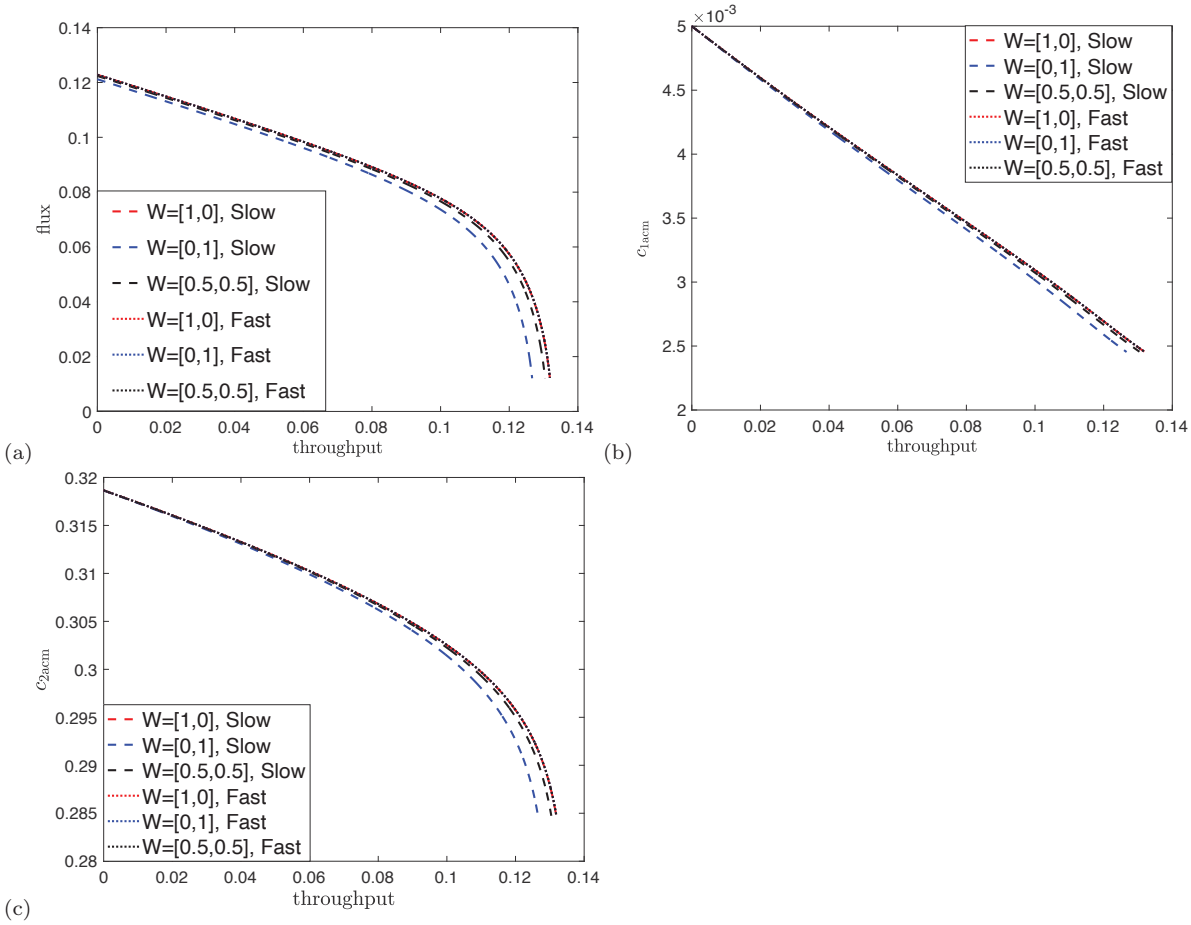

Figure 3.3 Comparison of slow method $J(a_0) = w_1 j(t_\mathrm{f}) + w_2 c_{2\mathrm{acm}}$ (dashed curves) with fast method $J_{1,\mathrm{fast}}(a_0) = w_1 u(0) + w_1 u'(0) + w_2 c_{2\mathrm{ins}}(0) + w_2 c'_{2\mathrm{ins}}(0)$ (dotted curves) for various weights W= $[w_1, w_2]$, with $\beta = 0.1, \xi = 0.5, \lambda_1 = 1$: (a) flux vs. throughput (u, j) plot, (b) cumulative concentration of type 1 particles vs. throughput $(c_{1\mathrm{acm}}, j)$ plot, (c) cumulative concentration of type 2 particles vs. throughput $(c_{2\mathrm{acm}}, j)$ plot.

w_1 is the weight for the total throughput, $j(t_f)$, while w_2 weights final cumulative concentration of type 2 particles, $c_{2acm}(t_f)$). The results presented here for $[w_1, w_2] = [1, 0]$ correspond to the optimized profiles presented in Figure 3.2. Results are plotted as functions of filtrate throughput over the duration of the filtration, $0 \leq t \leq t_f$. The quantities shown in Figure 3.3, for the optima obtained using both methods, are: (a) flux vs. throughput (u, j) plot; (b) accumulative concentration of type 1 particles vs. throughput, (c_{1acm}, j) plot; and (c) accumulative concentration of type 2 particles vs. throughput, (c_{2acm}, j) plot; all simulated with $\xi = 0.5, \beta = 0.1, \alpha_1 = \alpha_2, \lambda_1 = 1$, and $R_1(0) \geq \tilde{R}$. The figure shows that for all three sets of weights considered, $[w_1, w_2] = [1, 0], [0.5, 0.5]$ and $[0, 1]$, the fast method finds an optimized $a_0(x)$ as good as or better than that found by the slow method (larger or the same values for $j(t_f)$ and $c_{2acm}(t_f)$, while always satisfying the removal criterion $\tilde{R}$ for particle type 1).

These results (as well as many others not discussed here) demonstrate that, for the same number of searching points, the fast method converges to an optimizer that in all cases is as good as, or slightly better than, that obtained using the slow method, with considerably shorter running time (a typical optimization for the slow method takes 40 minutes with 10,000 searching points, while the fast method takes only 4 minutes). We also observe that varying the weights $[w_1, w_2]$ does not change the optimized profile significantly (especially with the fast method), indicating that maximizations of $j(t_f)$ and of $c_{2acm}(t_f)$ are correlated for the parameter values considered. One possible explanation for this correlation is that, provided the type 1 particle removal constraint $R_1(0) \geq \tilde{R}$ is met, the initial concentration of type 2 particles in the filtrate $c_2(1, 0)$ should be maximized by maximizing the initial flux $u(0)$, since the higher the flux, the more type 2 particles will escape capture by the filter.

Figure 3.4 presents direct comparisons of the slow and fast methods for **Problem 2**. Results for the slow method, with objective function (3.32), are

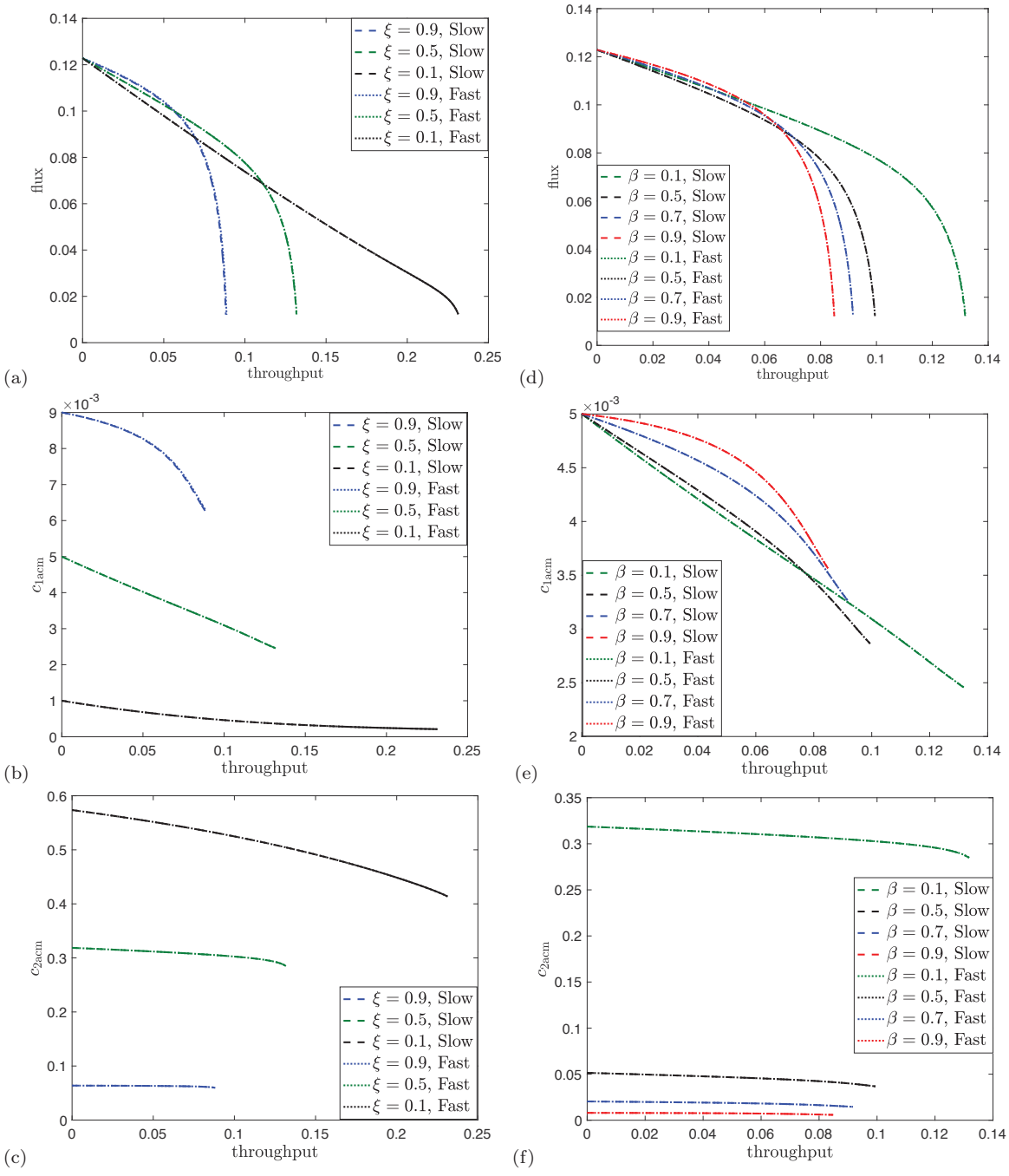

Figure 3.4 Comparison of slow method with objective function $J(a_0) = j(t_\mathrm{f})c_{2\mathrm{acm}}(t_\mathrm{f})$ (dashed curves) and fast method $J_{2,\mathrm{fast}}(a_0) = u(0)c_{2\mathrm{ins}}(0)$ (dotted curves) (a-c): with $\xi = 0.9, 0.5, 0.1$ and $\beta = 0.1$, $\alpha_1 = \alpha_2$, $\lambda_1 = 1$: (a) (u, j) plot, (b) $(c_{1\mathrm{acm}}, j)$ plot, (c) $(c_{2\mathrm{acm}}, j)$ plot. (d-f): with $\beta \in [0.1, 0.9]$ varying and $\xi = 0.5, \lambda_1 = 1$: (d) (u, j) plot, (e) $(c_{1\mathrm{acm}}, j)$ plot, (f) $(c_{2\mathrm{acm}}, j)$ plot.

indicated by dashed curves; and those for the corresponding fast method, with objective function (3.35), by dotted curves. The left panel, Figures 3.4 (a-c), shows results for various feed particle-composition ratios ξ (other parameters as in Figure 3.3); while the right panel, Figures 3.4 (d-f), compares results for various effective particle-membrane interaction ratios β, with $\xi = 0.5$. The flux through the membrane and the cumulative particle concentrations of each particle type in the filtrate are plotted as functions of filtrate throughput over the duration of the filtration, $0 \leq t \leq t_{\mathrm{f}}$. In all cases, for the same number of searching points, the fast method converges to the same optimal pore profile as the slow method across all ξ and β values considered (though the optima obtained are different for each parameter set). Similar to Problem 1, the computational speedup is considerable using the fast method.

In addition to demonstrating the efficacy of the fast optimization method, the results also illustrate some general features of the model. When a feed contains a larger fraction (higher ξ-value) of particles to be removed (type 1 particles here), our model predicts shorter filter lifetime (due to faster fouling) when compared to a feed with lower ξ-value, leading to less total throughput and lower final accumulative particle concentration of type 2 particles in the filtrate, see e.g., Figures 3.4(a) and (c). This is not desirable if we want to maximize total collection of type 2 particles; we will present one possible way to circumvent this issue in Subsection 3.5.1.2, where a multi-stage filtration is proposed.

Figure 3.4(b) is the $(c_{1\mathrm{acm}}, j)$ plot. Note that in all cases, the constraint for removal of particle type 1 is tight at the optimum, with the exact specified proportion $\tilde{R}$ of particles removed from the feed at time $t = 0$. Figures 3.4 (d-f) show that larger β values (meaning that the two particle types are more physicochemically similar; recall $\beta \in (0, 1)$ throughout our study, and if $\beta = 1$ both particle types interact identically with the membrane) lead to faster fouling of the filter, with lower total throughput

and lower total yield of type 2 particles in the filtrate. This confirms our expectation that the more similar the particle types are, the more challenging it is to separate them by filtration. To achieve effective separation, a sufficient physicochemical difference $\gamma = 1 - \beta$ is required.

Encouraged by the excellent results and significant speedup obtained when using the fast method with the same number of searching points as the slow method, we next investigate its performance with fewer searching points. Figure 3.5 shows the comparison between the slow method (dashed curves) with 10,000 searching points (found, empirically, to be the minimum number required for reliable results) and the fast method (dotted curves) with decreasing number of search points (10,000, 1,000, 100). Model parameters are fixed at $\xi = 0.5$ and $\beta = 0.1$; other parameters as in Figure 3.3. These results (as well as many other tests, not shown here) indicate that the fast method produces reliable results with just 1,000 searching points (blue dotted curves; this optimum even appears superior to the slow method with 10,000 search points, providing slightly higher total throughput). Even with as few as 100 search-points the fast method produces reasonable (though suboptimal) results (black dotted curve). In all cases, the particle removal constraint on c_1 is again tight at the optima found. Since run time for the optimization routine appears to scale in direct proportion to the number of searching points, a 10-fold reduction in the number of search points needed represents a significant additional computational saving: the fast method utilizing 1,000 search points is approximately 100 times faster than the slow method utilizing 10,000 points.

3.5.1.2 Multi-stage filtrations. In Figure 3.4 (a) we observed that, with a higher concentration ratio (e.g., $\xi = 0.9$) of type 1 particles in the feed, the optimized filter for a single-stage filtration tends to be fouled faster, which leads to lower total throughput per filter. This makes sense as the filter needs to remove a higher mass of

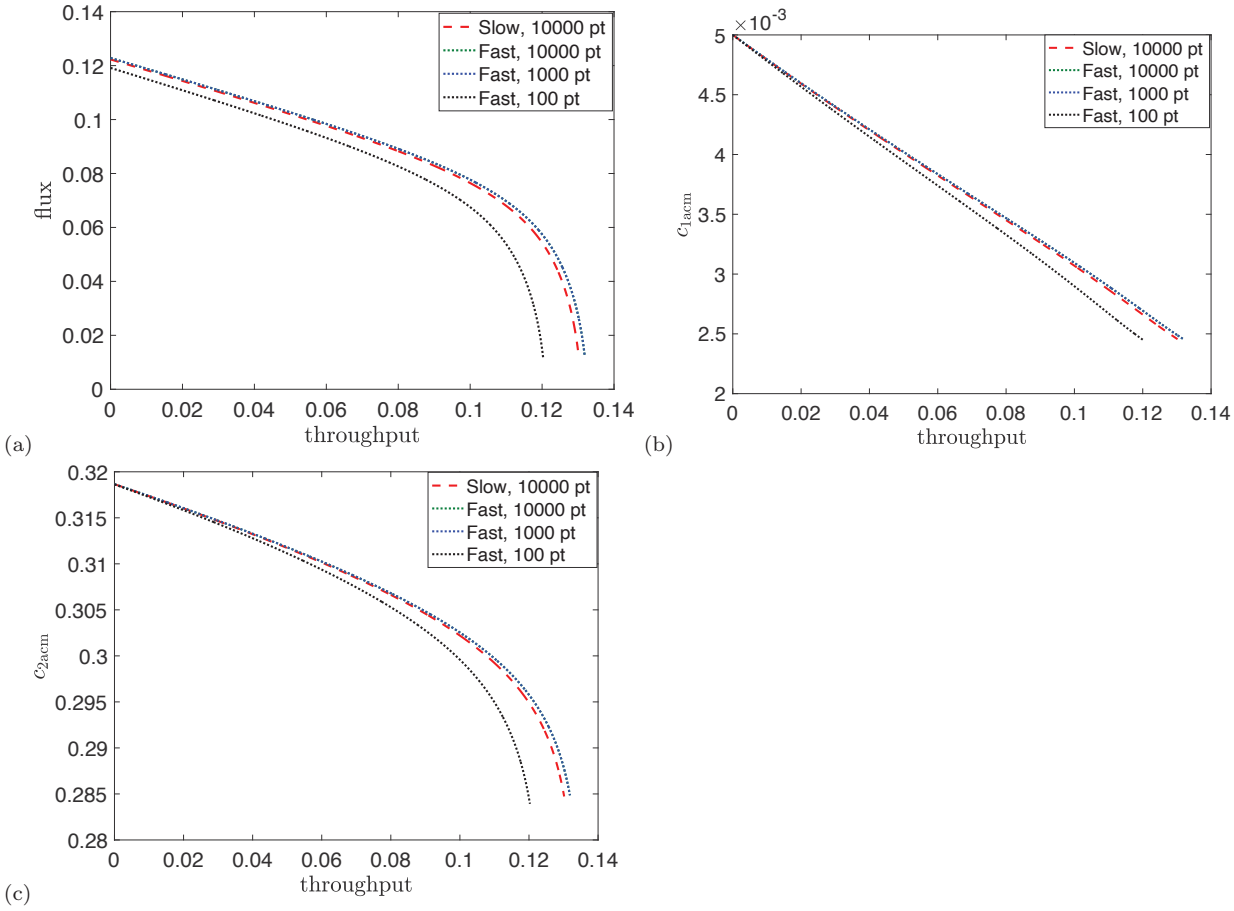

Figure 3.5 Comparison of slow method $J_{\mathrm{slow}}(a_0) = j(t_{\mathrm{f}})c_{2\mathrm{acm}}(t_{\mathrm{f}})$ (dashed curves) with 10,000 start points, with fast method $J_{\mathrm{fast}}(a_0) = u(0)c_{2\mathrm{ins}}(0)$ (dotted curves) using variable number of searching points, with $\xi = 0.5, \lambda_1 = 1$ and $\beta = 0.1$: (a) (u, j) plot; (b) $(c_{1\mathrm{acm}}, j)$ plot, and (c) $(c_{2\mathrm{acm}}, j)$ plot.

impurity (type 1 particles) to achieve the initial particle removal threshold $R_1(0) \geq \tilde{R}$ when ξ is larger. Our simulations also reveal that the fouling is largely confined to a narrow region adjacent to the upstream surface of the filter at optimum, with the majority of the downstream portion of the filter remaining unused (see Figure 3.2). In this section we propose a multi-stage filtration scenario that has the potential to alleviate some of these inefficiencies. Heuristically, we would like to process more feed per filter by increasing the membrane porosity and make more efficient use of the membrane material by fouling a higher proportion of the pore (void) volume (this will be discussed further in results corresponding to Figures 3.7 and 3.8); however, increasing the porosity will in general decrease the particle removal efficiency (due to higher flux), so the filtrate requires further purification to satisfy the particle removal requirement. This forms the basic idea of the proposed multi-stage filtration strategy: we will lower the initial particle removal requirement to increase the amount of feed processed per filter and try to satisfy the particle removal requirement by filtering the collected filtrate again, possibly more than once (multi-stage). The multi-stage filtration will work if the increase in feed processed can offset the increase in the number of additional filters required to meet the particle removal requirement. From the optimization point of view, we increase the feasible searching space by relaxing the initial particle removal constraint so that a better optimizer might be found.

In the following discussion we focus on the optimization **Problem 2**, where the goal is to maximize the yield (mass) of type 2 particles per filter used, while achieving *effective separation*,[4] which for definiteness we here define as removing the desired fraction $\tilde{R}$ of particle type 1 from the feed ($\bar{R}_1(\mathrm{t_f}) \geq \tilde{\mathrm{R}}$) while simultaneously recovering a minimum desired yield fraction Υ of type 2 particles in the filtrate ($\bar{R}_2(t_f) \leq 1 - \Upsilon$). For all of our simulations, $\tilde{R} = 0.99$ and $\Upsilon = 0.5$. We define

[4]The term "effective separation" has been used in the literature, though without clear quantitative definition, e.g. [33, 46, 54].

the *purity* for type i particles in the filtrate, $k_i \in [0,1]$, as

$$k_i = \frac{c_{i,\mathrm{acm}}(t_\mathrm{f})}{\sum_{i=1,2} c_{i,\mathrm{acm}}(t_\mathrm{f})}, \qquad i = 1,2, \tag{3.36}$$

where $c_{i,\mathrm{acm}}(t_\mathrm{f})$ is the accumulative concentration of the type i particle in the filtrate at the end of the filtration. With our hypothesized scenario of feed containing desired (type 2) and undesired (type 1) particles in mind, we note a simple relationship between the purity of type 2 particles and the final cumulative removal ratios:

$$k_2 = \frac{(1-\xi)[1-\bar{R}_2(t_\mathrm{f})]}{\xi[1-\bar{R}_1(t_\mathrm{f})] + (1-\xi)[1-\bar{R}_2(t_\mathrm{f})]}. \tag{3.37}$$

We will return to these definitions later.

The basic idea behind our multi-stage filtration is to first optimize the filter with a less strict initial type 1 particle removal requirement (i.e., we require $R_1(0) \geq R < \tilde{R}$) and filter the feed solution two or more times to achieve a larger total *yield per filter* of purified type 2 particles than in a single-stage filtration, with the effective separation condition satisfied at the end of the multi-stage filtration. We determine the *stage* of filtration by how many times the solution has passed through clean filters: for example, the clean stage 1 filter will take feed directly and be used to exhaustion; the filtrate collected from the stage 1 filter will then be sent through a new (clean) stage 2 filter (which may be used more than once within stage 2).

We propose the following two-stage or multi-stage filtration strategy: **1.** Optimize the filter (for **Problem 2**) with a less strict initial particle removal requirement ($R_1(0) \geq R < \tilde{R}$) and denote the optimized filter as F_R (e.g., for $R = 0.5$, we denote the optimized filter as $F_{0.5}$). **2.** (Stage 1) Run the filtration simulation using F_R until the filter is completely fouled; collect the filtrate. In scenarios to be considered later we allow stage 1 to use several filters simultaneously. **3.** Re-filter the collected filtrate through another clean F_R; collect the new filtrate. **4.** Test the filtrate from step 3. Does it meet required type 1 particle final removal requirement $\bar{R}_1(t_\mathrm{f}) \geq \tilde{R}$?

If yes, we are done; if no, repeat step 3 using the same filter until the requirement is met, or until this F_R is completely fouled. **5. (multi-stage)** If F_R is completely fouled before the requirement $\bar{R}_1(t_\mathrm{f}) \geq \tilde{R}$ is met, use another clean F_R and repeat step 3 until $\bar{R}_1(t_\mathrm{f}) \geq \tilde{R}$ is met. **6.** Once the threshold $\bar{R}_1(t_\mathrm{f}) \geq \tilde{R}$ is met, record the total mass of compound 2 in the filtrate and the number of F_R used, to compute the mass yield per filter. In order to keep track of the number of filters used and how many times each is reused, we identify each (stage) filter used by $F_{R,m}$, e.g., the second (stage) $F_{0.5}$ filter will be denoted $F_{0.5,2}$, and we track how many times each stage filter has been used by $n(m)$, e.g., $n(2)$ denotes the number of times $F_{0.5,2}$ is used. In cases where stage 1 involves more than one clean filter (used simultaneously) we also use notation l_m to denote the total number of mth stage filters used, e.g., l_2 is the number of stage 2 filters used; and we denote the total number of filters used at the end of multi-stage filtration by $M = \sum_m l_m$.

The operating procedure described above is summarized as a flow chart in Figure 3.6. After the multi-stage filtration is concluded we calculate the total mass of type 2 particles collected per filter used, $c_{2\mathrm{acm}}(t_\mathrm{f})j(t_\mathrm{f})/M$, and compare it with the collected mass from the filter F_R optimized for single-stage filtration. If the mass collected per filter used is larger for the multi-stage filtration, then the process is deemed more cost-effective.

In table 3.4, we list results comparing a single-stage filtration using a filter $F_{\tilde{R}}$ (optimized for particle type 1 initial removal threshold set at the desired value $\tilde{R}$), with two separate two-stage filtrations using filters $F_{0.7}$ and $F_{0.5}$ (optimized for lower initial removal thresholds $R = 0.7$ and $R = 0.5$, respectively). Fast optimization was carried out using objective function $J_{2,\mathrm{fast}}(a_0) = u(0)c_2(0)$ with $\xi = 0.9, \beta = 0.1, \alpha_1 = \alpha_2$, and $\lambda_1 = 1$. The quantities listed in table 3.4 are: R, initial type 1 particle removal threshold; M, total number of filters used in each case; $n(2)$, the number of times the 2nd (stage 2) filter is used; $\bar{R}_1(t_\mathrm{f})$ and $\bar{R}_2(t_\mathrm{f})$, the final cumulative particle removal

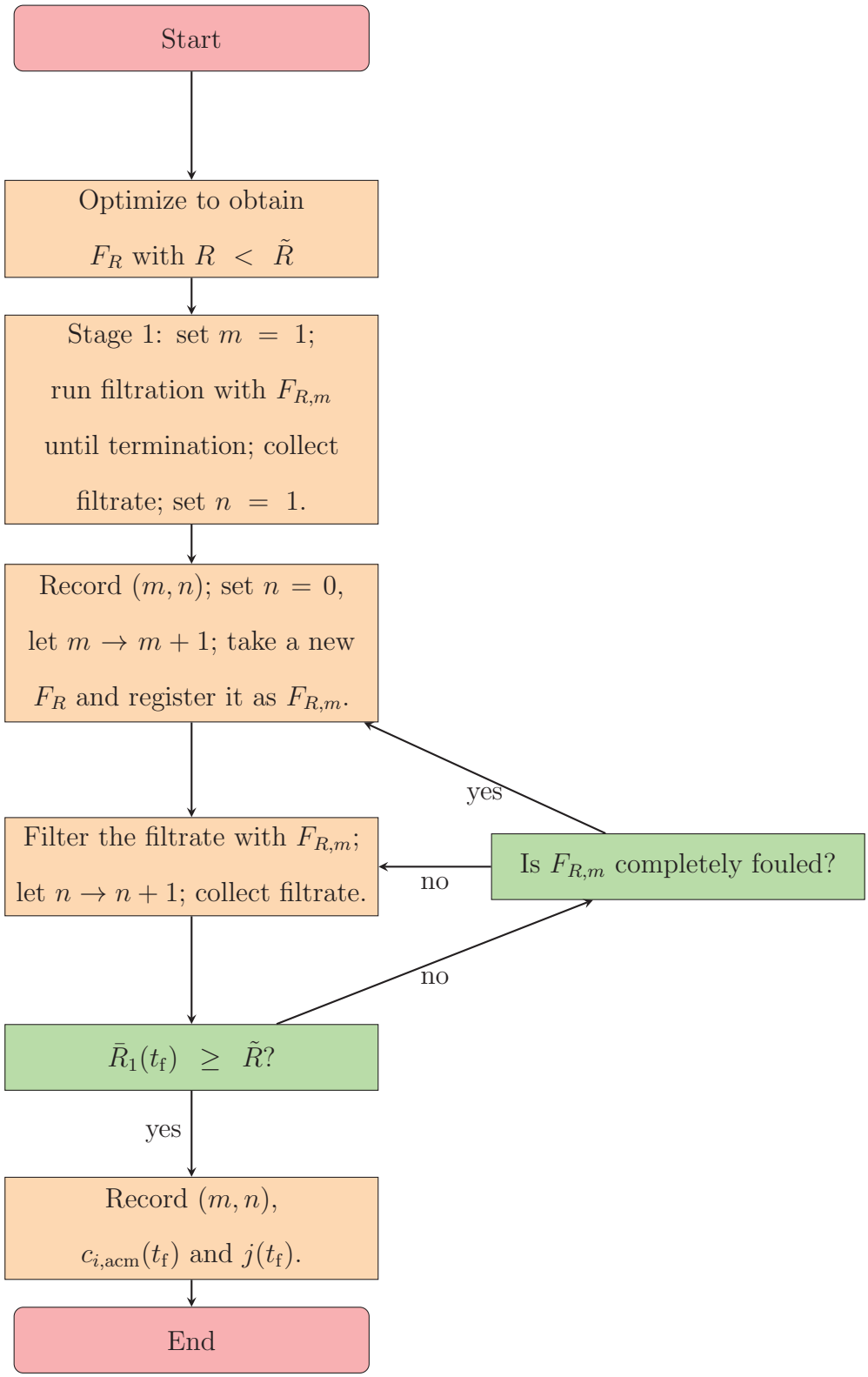

Figure 3.6 Flow chart of multi-stage filtration. $F_{R,m}$ signifies the mth stage filter used; for each $F_{R,m}$, $n(m)$ records how many times the filter is used.

Table 3.4 Comparisons of Single-stage Filtration ($R = \tilde{R}$) with 2-stage Filtrations ($R = 0.7$ and $R = 0.5$)

R	M	$n(2)$	$\bar{R}_1(\mathrm{t_f})$	$\bar{R}_2(\mathrm{t_f})$	k_2	$j(\mathrm{t_f})$	**mass yield/filter**
$\tilde{R}(=0.99)$	1	n/a	0.993	0.404	0.904	0.089	0.00528
0.7	2	3	0.997	0.455	0.954	0.217	0.00591
0.5	2	4	0.995	0.427	0.935	0.316	0.00905

We Record: M, the Total Number of Filters Used for Each Filtration Process; $n(2)$, the Number of Times the 2nd Filter is Used for Each Multi-stage Filtration Process; $\bar{R}_1(\mathrm{t_f})$ and $\bar{R}_2(\mathrm{t_f})$, the Final Cumulative Particle Removal Ratios for Particle Types 1 and 2 Respectively; k_2, the Purity of Type 2 Particles in the Final Filtrate; $j(\mathrm{t_f})$, Total Throughput; and Type 2 Particle Mass Yield per Filter.

ratios for particle types 1 and 2, respectively; k_2, the purity of type 2 particles in the final collected filtrate; $j(\mathrm{t_f})$, the total throughput; and the total mass yield of purified type 2 particles per filter (all relevant quantities are defined in Table 3.3).

These preliminary results show that, when our multi-stage filtration protocol is applied, we can achieve the same final particle removal requirement $\bar{R}_1(t_\mathrm{f}) \geq \tilde{R}$ as the single stage filtration but with much higher yield per filter of particle type 2; e.g., the third row of Table 3.4 shows that, with $R = 0.5$ the yield of purified type 2 particles per filter is almost doubled when compared to the single-stage filtration optimized for $R = \tilde{R}$. From table 3.4 we also observe that the multi-stage filtrations improve the purity of the filtrate as indicated by the k_2 values. We note that all three filtrations achieve effective separation according to our (somewhat arbitrary) definition, which corresponds to purity $k_2 \geq 0.847$ for the cases considered in Table 3.4, i.e., $\xi = 0.9$. If higher purity is desired to consider a separation effective, the removal ratios $\bar{R}_1(t_\mathrm{f})$ and $\bar{R}_2(t_\mathrm{f})$ can be adjusted accordingly based on Equation (3.37).

Figure 3.7 illustrates the results for the three optimized filters summarized in table 3.4 via the fouling evolution of the filter pores. Figures 3.7(a-c) show the filters from the first filtration stage, optimized for particle removal thresholds $R = \tilde{R}$ (a), $R = 0.7$ (b), and $R = 0.5$ (c), at time $t = t_\mathrm{f}$ (when the flux is reduced to the fraction

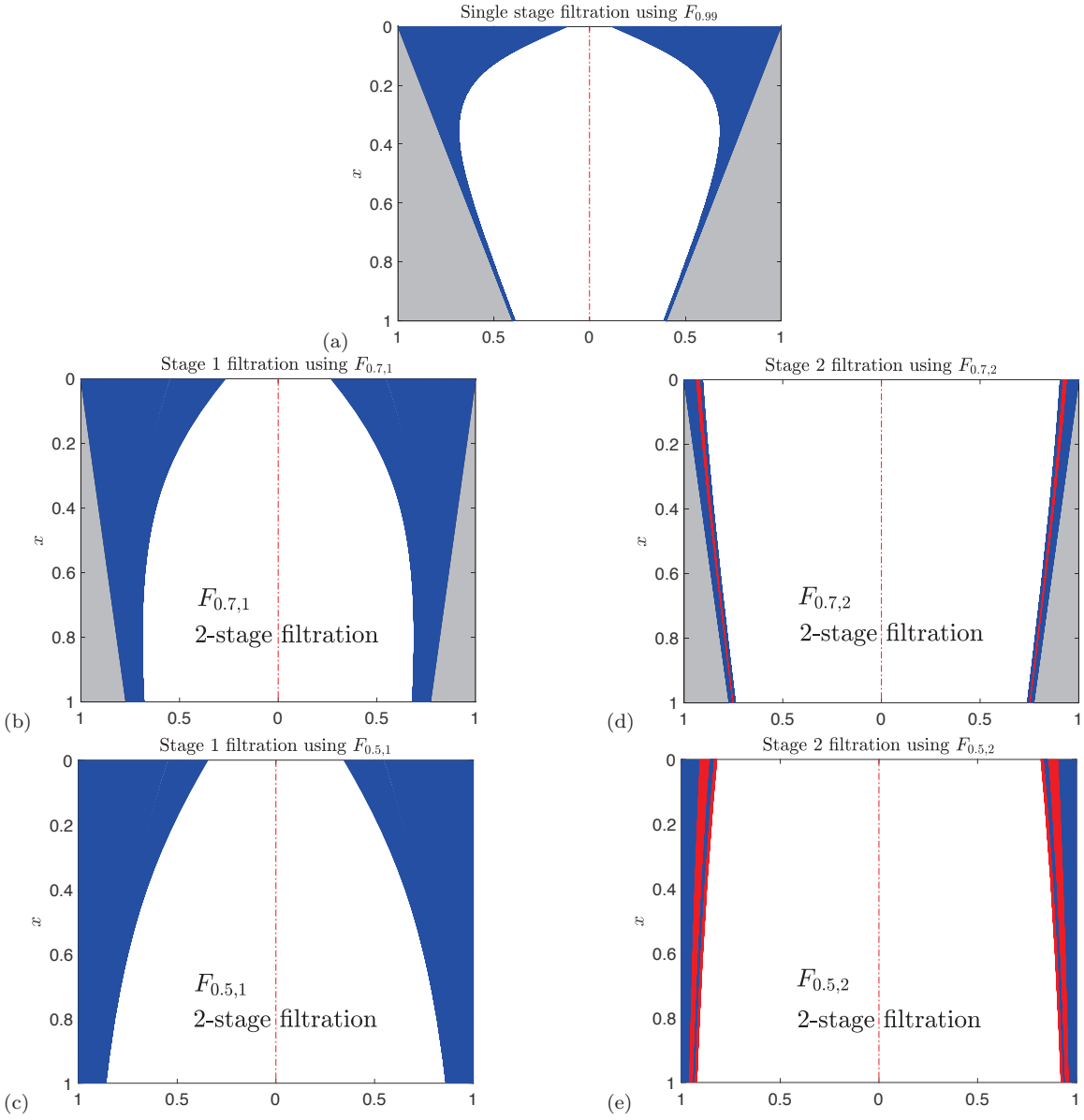

Figure 3.7 Comparison of single stage filtration and two-stage filtrations. (a-c) show completely fouled filters $F_{R,1}$ optimized for: (a) $R = \tilde{R}$ (single-stage filtration), (b) $R = 0.7$ and (c) $R = 0.5$, with other parameters fixed at $\xi = 0.9, \beta = 0.1, \alpha_1 = \alpha_2, \lambda_1 = 1$. Gray color indicates membrane material, blue is deposited particles, and white is void. (d, e) show the fouling sequence for the second filtration stages, required when $R < \tilde{R}$: (d) filtrate from (b) is passed repeatedly through $F_{0.7,2}$ and (e) filtrate from (c) is passed repeatedly through $F_{0.5,2}$, with alternating blue and red indicating deposited particles from the successive filtrations (filter reuse). Full details in text.

$\vartheta = 0.1$ of its initial value). Other model parameters are fixed at $\xi = 0.9, \beta = 0.1, \alpha_1 = \alpha_2, \lambda_1 = 1$. The blue and red colors indicate deposited particles; a change of color indicates reuse of the filter. Figures 3.7(d) and (e) show the fouling of the second stage filters, $F_{0.7,2}$ and $F_{0.5,2}$ respectively. We can see that when the initial removal threshold R is decreased, the fouling of the pore becomes more uniform along its depth, and the porosity of the corresponding optimized filter F_R increases. For the case $R = 0.5$, the optimized pore profile is almost as wide as possible; the gray colored region corresponding to the membrane material is too thin to be visible. The high mass yield per filter and small quantity of membrane material (due to high porosity) required to produce $F_{0.5}$ indicates that if the membrane material has good selectivity (i.e., high particle removal capability, greater λ_1 value in our model), it might be advantageous to focus on maximizing the filter porosity as a design approach to increasing the mass yield per filter, while simultaneously reducing the membrane material cost per filter and achieving effective separation using multi-stage filtration.

From Figures 3.7(d) and (e), it is clear that in both multi-stage filtration protocols, the secondary filters $F_{0.7,2}$ and $F_{0.5,2}$ are only lightly-used at termination, and could be used to process more filtrate. Specifically, we could use two or more first-stage filters $F_{R,1}$ in order to create sufficient once-filtered fluid to pass through the second stage filter $F_{R,2}$ and foul it significantly. We anticipate that increasing the volume of filtrate collected from stage 1 of the filtration using multiple $F_{R,1}$ should lead to higher mass yield per filter by more fully utilizing the filtration capacity of the stage 2 filter $F_{R,2}$. Before investigating this idea in detail we first test it using two, three and four stage-1 filters ($l_1 = 2, 3, 4$), which lead to 2-stage, 2-stage and 3-stage filtrations, respectively. The results are presented in Figure 3.8, using the filter $F_{0.5}$ (optimized for $R = 0.5$ as in Figure 3.7) with parameters as for the simulations of Figure 3.7.

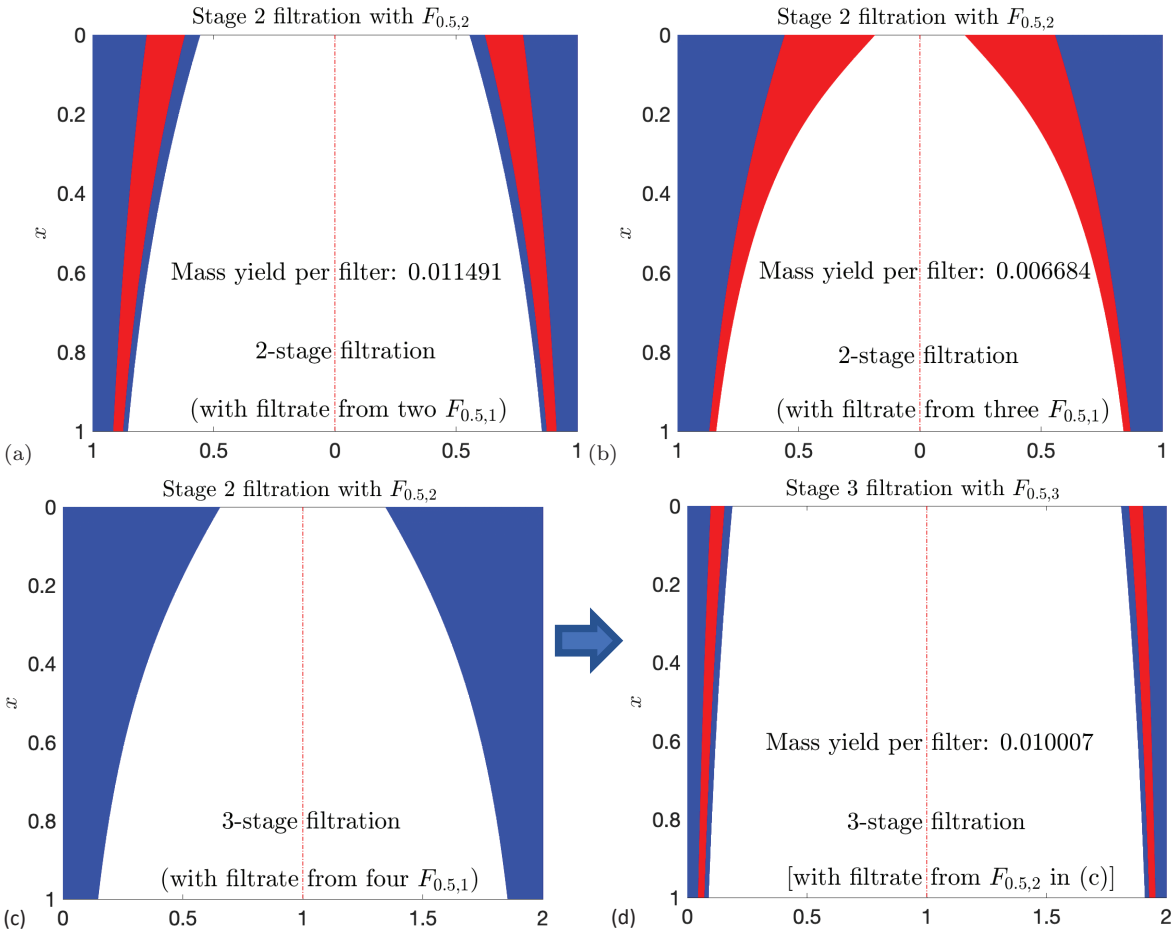

Figure 3.8 Multi-stage filtrations: (a,b) show second stage of 2-stage filtrations; (c,d) show 2nd and 3rd stages of a 3-stage filtration. (a) fouling of $F_{0.5,2}$ by filtering filtrate collected from two $F_{0.5,1}$ filters. (b) fouling of $F_{0.5,2}$ by filtering filtrate collected from three $F_{0.5,1}$ filters. (c) and (d): 3-stage filtration with (c) fouling of $F_{0.5,2}$ by filtering filtrate collected from four $F_{0.5,1}$ filters; (d) fouling of $F_{0.5,3}$ by filtering filtrate collected from $F_{0.5,2}$ shown in (c).

In the first test example, in stage 1 we collect filtrate by exhausting two $F_{0.5,1}$ filters ($l_1 = 2$; the fouling plot for each of these $F_{0.5,1}$ is identical to Figure 3.7(c) so is omitted in Figure 3.8) and then in stage 2, we send the combined filtrate repeatedly through an initially clean $F_{0.5,2}$. Figure 3.8(a) shows the subsequent fouling of $F_{0.5,2}$, with alternating blue and red color indicating particle deposition and filter reuse as before. After passing the filtrate through $F_{0.5,2}$ three times, the final particle 1 removal requirement is met (so $l_2 = 1$ and $M = l_1 + l_2 = 3$).

In the second example, in stage 1 we collect filtrate by exhausting three $F_{0.5,1}$ filters ($l_1 = 3$; again see Figure 3.7(c) for this stage). In stage 2 we pass the filtrate from stage 1 through an initially clean $F_{0.5,2}$. Figure 3.8(b) shows the fouling of this second-stage filter $F_{0.5,2}$. It is used twice, but during the second use becomes completely fouled before all the filtrate can be filtered. Leaving aside for the moment the question of whether a second stage-2 filter should be introduced to deal with the leftover twice-filtered fluid, we check the (thrice filtered) filtrate from this second stage-2 filtration and find that it meets the final particle 1 removal requirement. In this example, $l_2 = 1$ and $M = 1_1 + l_2 = 4$.

In the third example, at stage 1 we collect filtrate by exhausting four $F_{0.5,1}$ filters ($l_1 = 4$). This combined filtrate is then passed through a clean second-stage filter, $F_{0.5,2}$, whose fouling is shown in Figure 3.8(c). This $F_{0.5,2}$ filter is completely fouled after one use ($l_2 = 1$). Again, we defer the question of whether a second stage-2 filter would be cost-effective to deal with the remaining once-filtered feed, and check the particle-1 removal requirement of the twice-filtered feed. It is not yet satisfied, so we need a third stage of filtration with a new filter $F_{0.5,3}$. Figure 3.8(d) shows the fouling of this $F_{0.5,3}$ filter, which is used three times before the final particle 1 removal requirement is satisfied ($l_3 = 1$). Here $M = l_1 + l_2 + l_3 = 6$.

We find that in the first example, when we collect filtrate from two $F_{0.5,1}$ filters (Figure 3.8(a)), the mass yield of type 2 particles per filter is 0.012, which is indeed

greater than the value 0.0091 obtained with the original two-stage filtration of Figure 3.7. However, with three stage-1 $F_{0.5,1}$ filters, the second example of Figure 3.8(b), the mass yield of type 2 particles per filter decreases to 0.0067 (see table B.1), which may be explained by the fact that the second stage filter $F_{0.5,2}$ is completely fouled on its second use before all the filtrate obtained in stage 1 can be processed (the yield loss is due to the discarded filtrate). Similar loss of filtrate is observed in the third example, the 3-stage filtration of Figures 3.8(c) and (d), in which filtrate collected from four $F_{0.5,1}$ stage 1 filters was sent through a stage-2 filter $F_{0.5,2}$, which is exhausted before all of the stage-1 filtrate can be filtered a second time. Despite this loss, the mass yield per filter is 0.010, nearly as good as the first example of Figure 3.8(a). Additional simulations of the second and third test scenarios, in which new filters were introduced to process the discarded filtrate, gave less favorable results than those presented here. These three multi-stage filtration experiments suggest that a single stage-2 $F_{0.5,2}$ filter can process filtrate collected from three to four stage-1 $F_{0.5,1}$ filters, but no more.

The observations of Figure 3.8, though preliminary, indicate there may be an optimal ratio between the number of filters to use at different stages, which would utilize each filter's filtration capacity as fully as possible, and minimize the loss of filtrate at each stage, ultimately maximizing the mass yield per filter. We used our model to conduct such an investigation, the details of which are provided in Appendix Section B. We find (by trial and error) that the mass yield per filter can be as high as 0.013 using a four-stage filtration, with the following numbers of filters per stage: $l_1 = 18, l_2 = 6, l_2 = 3, l_4 = 1$. This four-stage filtration is illustrated schematically in Figure 3.9.

3.5.2 Optimization of constant flux filtration

In this section we briefly highlight results for the constant flux case, focusing on optimization **Problem 3**, with objective function (3.33). We study how the particle

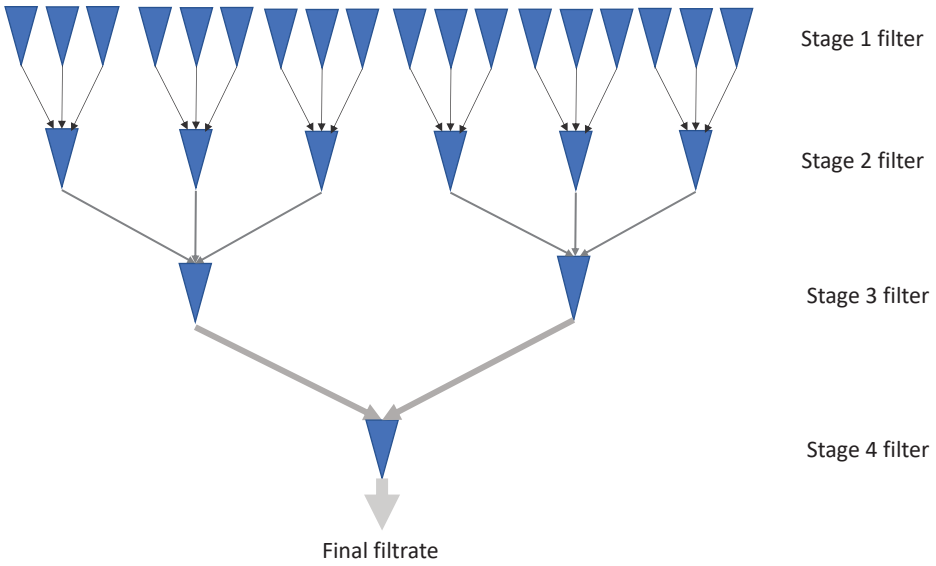

Figure 3.9 4-stage filtration illustration, with eighteen stage 1 filters, six stage 2 filters, two stage 3 filters and one stage 4 filter.

composition ratio in the feed (ξ) and the quantity of feed processed affect the optimization results. In all simulations we impose the additional constraints that the initial driving pressure $p(0,0) \leq 100$ and the driving pressure at the end of the filtration should be no greater than 10 times the initial driving pressure, i.e., $p(0,\mathrm{t_f}) \leq 10p(0,0)$ (typical driving pressure at termination is about 1.5-2 times the initial pressure [6, 57]). Simulations of our model at constant flux show that particle retention typically deteriorates over time, therefore, in addition to the initial particle removal requirement ($R_1(0) \geq \tilde{R}$) we also impose that the accumulative particle removal should be greater than a fixed number at the end of the filtration ($\bar{R}_1(\mathrm{t_f}) \geq \hat{R}$, where $\hat{R} \leq \tilde{R}$; this requirement also means that no fast optimization method is practicable for this case). The quantity of feed processed is fixed by specifying the number of time iterations N (in all simulations presented here $N \leq 1000$ and the time step is fixed).

Figure 3.10 shows the evolution of the optimized pore profiles obtained for the constant flux case (3.33) with $\xi = 0.9, 0.5, 0.1, \beta = 0.1, \lambda_1 = 10, \hat{R} = 0.98, N =$

1000. The figure shows: (a) driving pressure vs throughput, $(p(0,t),j)$-plot; (b) accumulative type 1 particle concentration in the filtrate vs throughput, $(c_{1\text{acm}},j)$-plot; (c) accumulative type 2 particle concentration in the filtrate vs throughput, $(c_{2\text{acm}},j)$-plot; and (d-f) show the pore profiles at the termination of the filtration for the three ξ-values, with blue color indicating deposited particles: (d) $\xi = 0.9$; (e) $\xi = 0.5$; (f) $\xi = 0.1$. We observe that, as ξ varies, the optimized pore profile changes significantly. For feed containing less impurity (the smallest value, $\xi = 0.1$, Figure 3.10(f)) the optimized pore profile is of Λ shape (instead of the V shape we observed consistently in the constant pressure case) and the particle deposition is more evenly distributed over the length of the pore. Also, in contrast to the constant pressure case, we see that the particle type 1 retention capability of the filter decreases in time for all three ξ values, with the most significant deterioration observed for the feed containing the highest fraction of impurity (the largest ξ-value, $\xi = 0.9$, see Figure 3.10(b)).

Another question of interest for this constant flux case is: how does the amount of feed processed affect the optimization result? We illustrate this by considering three different values of N, the total number of timesteps in our simulations. Figure 3.11 shows the evolution of pore profiles optimized for the constant flux objective function (3.33), with $\xi = 0.9, \beta = 0.1, \lambda_1 = 10, R = 0.99, \hat{R} = 0.98$ and $N = 1000, 500, 100$. The figure shows: (a) $(p(0,t),j)$-plot; (b) $(c_{1\text{acm}},j)$-plot; (c) $(c_{2\text{acm}},j)$-plot; and (d-e) show the pore profiles at the termination of the filtration, with blue color indicating particle deposition, for (d) $N = 500$ and (e) $N = 100$ ($N = 1000$ was shown earlier in Figure 3.10(d)). Collectively, Figures 3.10(d), 3.11(d) and 3.11(e) show that, as the quantity of feed decreases, the optimized pore profile changes from a V to a Λ shape. Comparing the optimized pore profiles with Figures 3.11(a-c) we see that the Λ shape is more prone to driving pressure increase and particle retention deterioration,

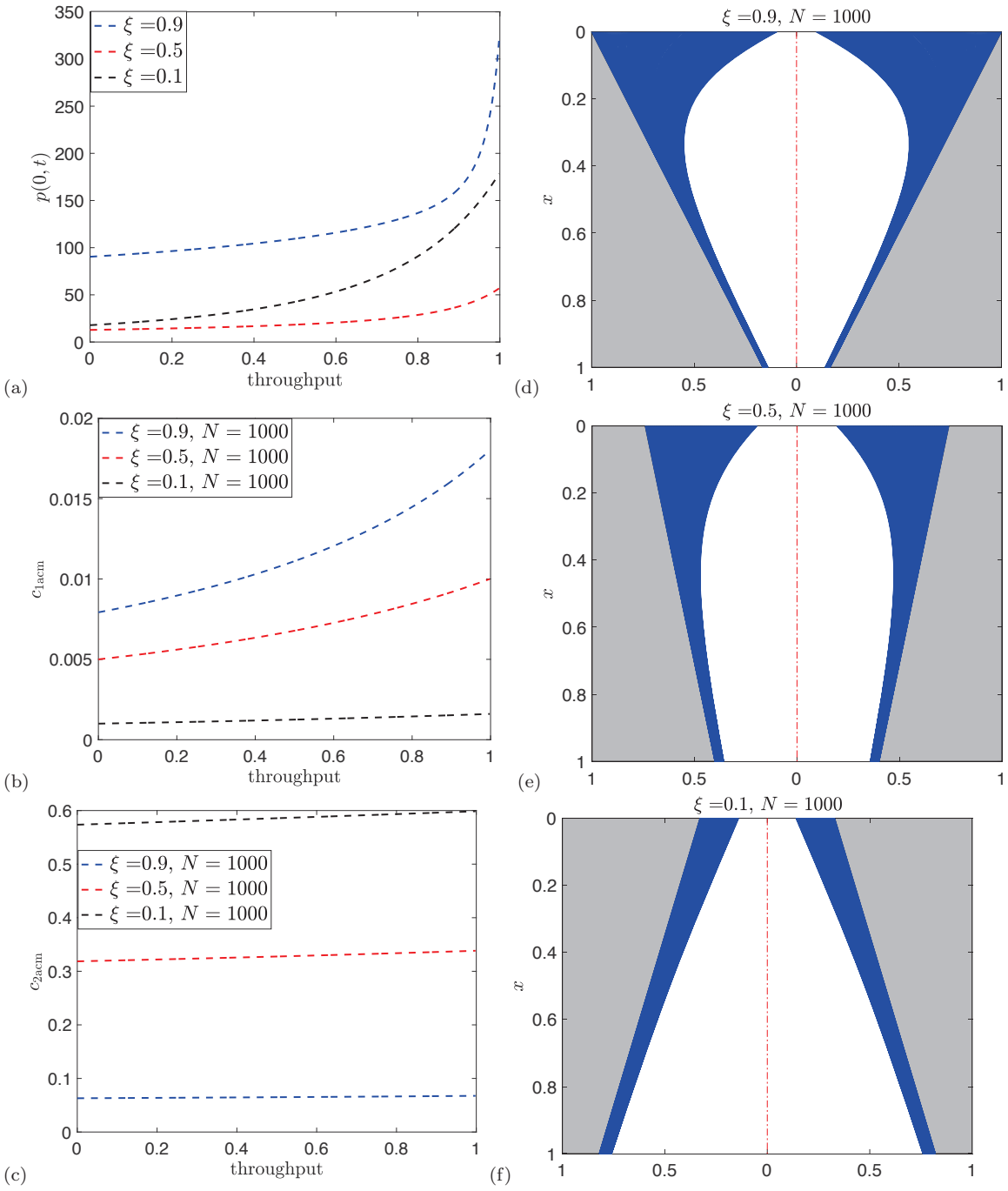

Figure 3.10 (a-c) Shows the evolution of optimized profile obtained for constant flux case with $\beta = 0.1, \lambda_1 = 10, \hat{R} = 0.98, N = 1000$ and $\xi = 0.9, 0.5, 0.1$,: (a) driving pressure vs throughput $(p(0,t), j)$ plot; (b) accumulative type 1 particle concentration in the filtrate vs throughput, $(c_{1\mathrm{acm}}, j)$ plot, and (c) $(c_{2\mathrm{acm}}, j)$ plot. (d-f) show the pore profile at the termination of filtration, with blue color indicating particle deposition: (d) $\xi = 0.9$; (e) $\xi = 0.5$; (f) $\xi = 0.1$.

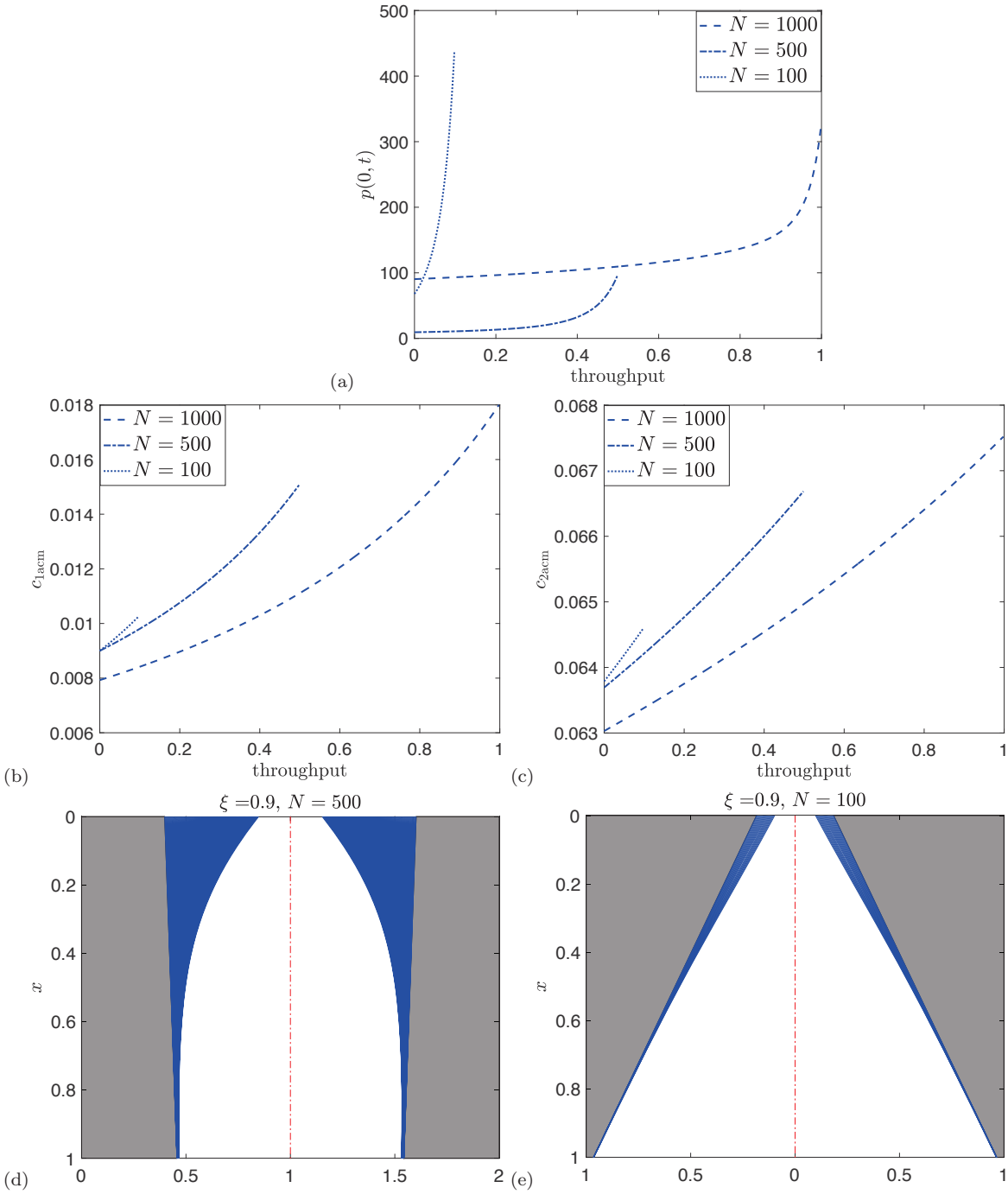

Figure 3.11 (a-c) Show the evolution of optimized profile obtained for constant flux objective function (3.33) with $\xi = 0.9, \beta = 0.1, \lambda_1 = 10, \hat{R} = 0.98$ and $N = 1000, 500, 100$: (a) $(p(0,t), j)$ plot (b) $(c_{1\mathrm{acm}}, j)$ plot, and (c) $(c_{2\mathrm{acm}}, j)$ plot. (d-e) show the pore profiles at the termination of the filtration, with blue color indicating particle deposition: (d) $N = 500$; (d) $N = 100$.

as well as the more even distribution of fouling noted earlier; observations that we now explain.

We deal first with the observation that for pores of Λ shape, particles deposit more evenly along the pore depth compared to pores of V shape. Particle concentration is always highest at the pore entrance, which favors a high deposition rate; however, flux u_p is also highest here for pores of Λ shape, which is unfavorable for particle deposition (both observations follow from Equation (3.23)). On the other hand, at the pore exit, particle concentration is lowest (unfavorable for deposition); but flux u_p is also lowest (favorable for particle deposition). Hence, for pores of Λ shape, there is always a competition between particle concentration and flux, which leads to the observed even fouling distribution along the pore length.

We next argue heuristically that this more uniform particle deposition is responsible for the observed particle concentration increase as follows: From Equations (3.22), (3.23) and (3.24) we obtain

$$c_i(1,t) = \left\{ \begin{array}{c} \xi \\ 1-\xi \end{array} \right\} \exp\Big[-\frac{\lambda_i \pi}{4} \int_0^1 a(x,t)dx \Big], \qquad \left\{ \begin{array}{c} i=1 \\ i=2 \end{array} \right\}, \tag{3.38}$$

showing that the change in particle concentration at outlet for type i particle depends on the change of the value of $\int_0^1 a(x,t)dx$. For Λ-shaped pores particle deposition is more even, thus $a(x,t)$ changes over the entire depth of the pore, with the consequence that $\int_0^1 a(x,t)dx$ changes more significantly than for V-shaped pores, where $a(x,t)$ changes significantly near the pore entrance, but on a region of small measure. The net effect for the Λ-shaped pore is the observed particle concentration increase in time. The same argument may also explain the significant pressure change for pores of Λ shape compared with pores of V shape, as the pressure change depends on the change of $\int_0^1 a^{-4}(x,t)dx$, see Equation (3.26).

Collectively, these arguments suggest the following explanation for why the Λ shape is selected for lower quantities of feed: For less feed, the filtration duration will be shorter; the significant particle concentration increase at the beginning of filtration for type 2 particles (see Figure 3.11(c)) is favorable for increasing the mass yield of these particles, while the short filtration duration keeps the concentration increase for type 1 particles within the prescribed removal limit.

The results in Figure 3.11 raise the question of whether the optimized pore profile will take the Λ shape more generally for sufficiently small feed quantity at constant flux regardless of particle composition ratio ξ. Figure 3.12 shows a sequence of simulations with a small quantity of feed characterized by $N = 100$, for different feed particle composition ratios $\xi = 0.9, 0.5, 0.1$, with $\beta = 0.1, \lambda_1 = 10, \hat{R} = 0.98$. The figure shows: (a) $(p(0,t), j)$-plot; (b) $(c_{1\text{acm}}, j)$-plot; (c) $(c_{2\text{acm}}, j)$-plot; while (d,e) show the pore profiles at the termination of the filtration, with blue color indicating deposited particles, for (d) $\xi = 0.5$; (e) $\xi = 0.1$ (the corresponding result for $\xi = 0.9$ was shown in Figure 3.11(e)). Collectively, Figure 3.11(e) and Figures 3.12(d) and (e) suggest that, for sufficiently small feed quantity, the optimized pore profile takes a Λ-shape regardless of feed particle composition. From Figures 3.12(b) and (c) we see the particle concentration changes are not significant for these short duration cases ($N = 100$), and the particle removal requirement for type 1 particles is satisfied for all three feeds with different particle-composition ratios; however, the pressure increase is still visible, see Figure 3.12(a).

3.6 Conclusions and Future Study

In this work we proposed a simplified mathematical model for filtration of feed containing multiple species of particles. Our focus in the main body of the paper was on a feed that contains just two particle species; a brief discussion of how the model extends to an arbitrary number of species is given in Appendix C. For the two-species

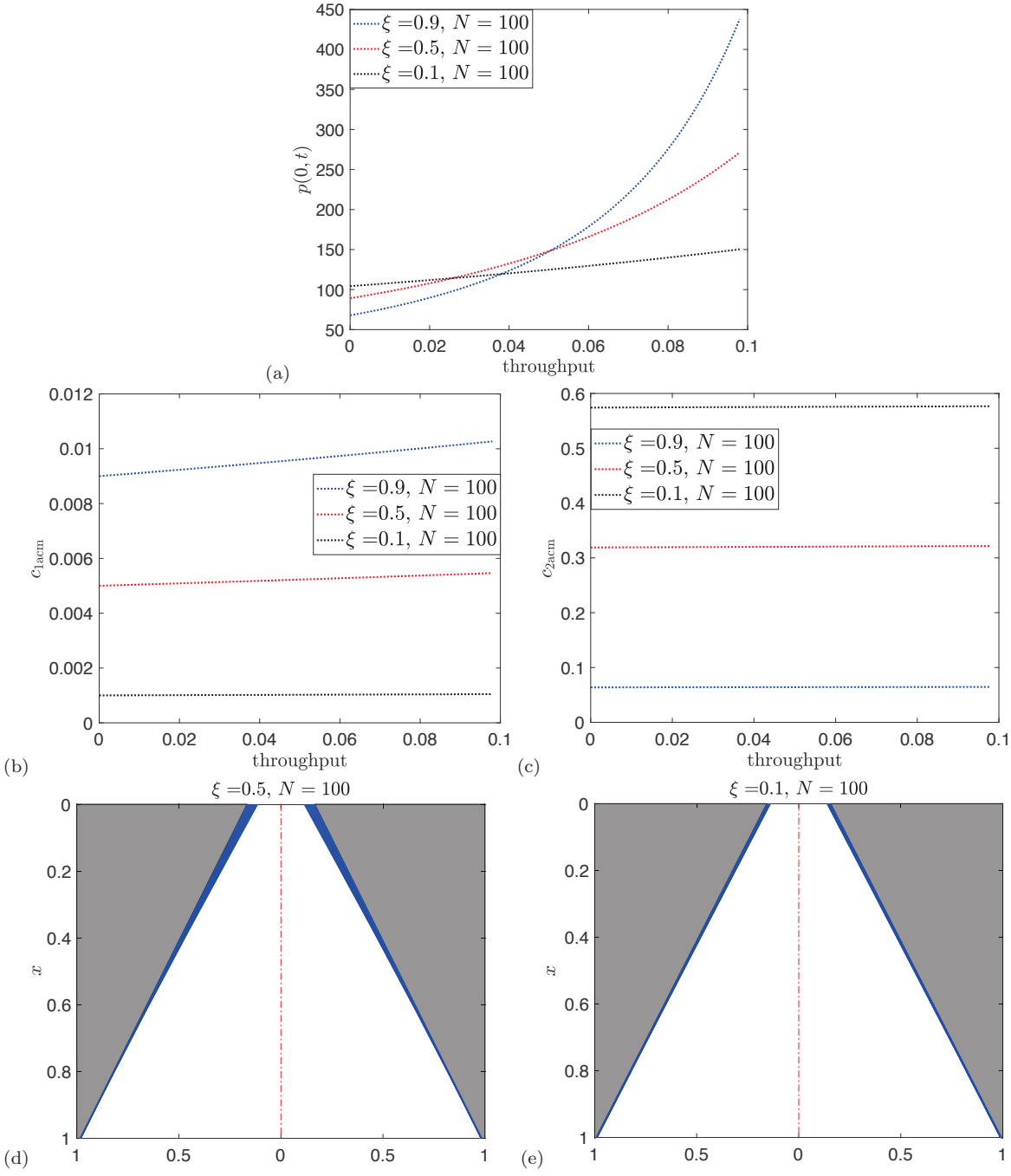

Figure 3.12 (a-c) Show the evolution for optimized pore profiles obtained for constant flux objective function (3.33) with $\xi = 0.9, 0.5, 0.1, \beta = 0.1, \lambda_1 = 10, \hat{R} = 0.98$ and $N = 100$: (a)$(p(0,t), j)$ plot (b) $(c_{1\mathrm{acm}}, j)$ plot, and (c) $(c_{2\mathrm{acm}}, j)$ plot. (d-e) shows the pore profile at the termination of the filtration, with blue color indicating particle deposition: (d) $\xi = 0.5$; (d) $\xi = 0.1$.

case, two important model parameters are identified and investigated to elucidate their effect on separation and optimal filter design: ξ, the concentration ratio of the two particle types in the feed, and $\beta = \Lambda_2\alpha_2/(\Lambda_1\alpha_1)$, the ratio of the effective particle deposition coefficients for the two particle types. A number of optimization problems for maximizing the mass yield of one particle species in the feed, while effectively removing the other, are considered, under both constant pressure and constant flux driving conditions. For filtration driven by a constant pressure drop, we find that the optimized pore profile is always of V-shape, which is in agreement with our earlier findings [59] for single-particle-species filtration (where the goal is to maximize total throughput of filtrate over the filter lifetime while removing a sufficient fraction of impurity). For filtration driven by a constant flux, the optimized pore profile may take either a V-shape or a Λ-shape depending on the particle composition ratio and the amount of feed considered for the optimization scenarios.

To increase the appeal and utility of our model for filter design applications, we proposed new objective functions (the fast optimization method) based on evaluating key quantities at the initial stage of the filtration. Due to the simpler forms of the proposed objectives, we find empirically that our fast method can be carried out with a relatively small number of initial search-points in design parameter space (compared with the slow method, which requires that a large number of simulations be run through to filter failure time). The proposed fast method is approximately 100 times faster than the naive slow method. The ideas that motivated our fast method could potentially be usefully applied to other optimization problems that require evaluation of quantities at the end of the time evolution, provided those quantities exhibit some monotonicity over time.

Observing that (based on our model predictions), effective separation in a single-stage filtration is usually achieved at the expense of short filter lifetime and inefficient filter use (most of the filter remaining only very lightly fouled), we also proposed an

alternative approach for maximizing the mass yield per filter while achieving effective separation, using multi-stage filtration. Using this approach we find that the mass yield per filter could be as much as two-and-a-half times that produced by the optimal single stage filtration, and surprisingly the purity of the final product is higher as well. In addition to the higher mass yield, the filter optimized for multi-stage filtration also requires less material to manufacture, due to its higher porosity. Multi-stage filtration has been utilized in industry [15] and reported experimentally [1,40]; however, to our best knowledge, little attention has been paid to optimizing this process from the theoretical side. We hope that our work will inspire further systematic studies into this promising approach.

CHAPTER 4

PRELIMINARY WORK: MODEL FOR REACTIVE PARTICLE REMOVAL

4.1 Overview

Filtration to remove undesired particles or contaminants is indispensable for many industrial applications, and in particular for waste water purification. In this chapter, we present a simple mathematical model for reactive particle removal using a reactive porous material. We demonstrate the applicability of our model by fitting it to experimental data using carefully estimated parameter values. Our optimization routines developed in Chapters 2 and 3 prove useful for finding the parameter values that provide the best fit to the experimental data.

4.2 Introduction

Filtration to remove undesired particles or contaminants is indispensable for many industrial applications, and has received significant attention in the scientific literature [12, 16, 60, 65, 66, 69]. A majority of studies focus on nondestructive particle removal via membrane filtration, based on considerations of the particle and pore size distribution [23, 31, 32, 41–43, 63], with considerable effort devoted to understanding the inevitable fouling [27, 28, 30, 55, 62]. However, very few studies have considered mathematical models for the alternative strategy of reactive particle removal using a chemically-active porous medium [36]: in many industrial settings, it may be possible to achieve particle removal by destructive means such as chemical reactions. Here, 'destructive' is understood to mean that during the filtration the particle and porous material react irreversibly with each other to form new compound. In this chapter, we outline a model for such reactive particle removal using dead-end filtration with feed containing multiple species of particles.

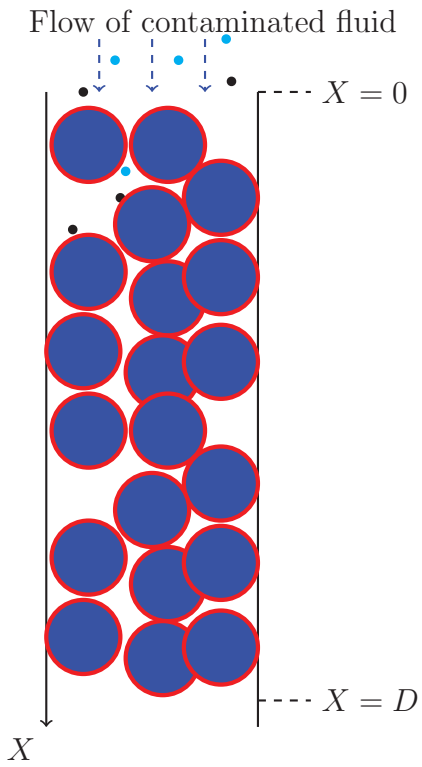

Figure 4.1 Schematic of unidirectional filtration through a reactive granular porous medium. Large blue circles represent the granular medium; the red boundary of these particles indicates the possible presence of a chemically-active coating. Small colored dots represent contaminant species to be removed via reaction.

We set up our model in Section 4.3, then present preliminary results that demonstrate its applicability in Section 4.4 by parameter fitting using experimental data from the study of Acheampong & Lens [1]. Discussion of our results and some preliminary conclusions will be made in Section 4.5.

4.3 Filtration Modeling with Reactive Particle Removal

We consider dead-end filtration of a feed solution containing two types of particles (e.g., chemically-distinct ions), type 1 and type 2, through a reactive porous medium of depth much greater than the typical pore size in the reactive granular material (e.g., a packed column of granular material such as chemically coated sand particles); see Figure 4.1, which shows a small portion of the reactive porous medium. We assume

that contaminant removal is through chemical reaction between the contaminants and the porous medium in the column. In addition we assume that the porous material granule size is much larger than the size of the contaminant particles to be removed. Considering the scale difference between the particle size in the feed and the porous material, we assume that the particle reaction with the reactive granular material, which happens only at the surface of the granular material, will not change appreciably the permeability of the porous medium while filtration is taking place. We implicitly assume that contaminant breakthrough — significant presence of undesirable particles in the filtrate — happens when the porous material loses its chemical reactive property, rather than due to any significant change in physical properties of the filter material (e.g., due to pore blocking). With the above assumption of constant permeability, a constant pressure drop applied across the porous medium will then generate a constant flux through it: the constant pressure and constant flux problems are equivalent here.

In setting up our mathematical model we use uppercase fonts to denote dimensional quantities and lower case for nondimensional quantities, which will be defined in Section 4.3.1 when we introduce appropriate physical scalings. We consider unidirectional Darcy flow in the positive X-direction, driven by constant pressure drop P_0 across the column. We assume the column has depth D (see Figure 4.1), and is of homogeneous composition (it would be easy to modify the model to allow for depth variation in the column). With the stated assumptions, the superficial Darcy velocity $\mathbf{U} = (U(T), 0, 0)$ within the column is given in terms of the pressure $P(X, T)$ by

$$U = -\frac{K}{\mu}\frac{\partial P}{\partial X}, \qquad 0 \le X \le D, \tag{4.1}$$

where μ is the viscosity of the incompressible feed solution (assumed Newtonian) and K is the column permeability. For the preliminary work described here, where the porous medium is homogeneous, a detailed expression for K in terms of physical

properties of the medium is not necessary, but if required, it could be modeled with the Kozeny-Carman formula for granular porous media (see, e.g. Probstein [47]),

$$K = \frac{\phi^3}{K_{\text{oz}} S_{\text{cp}}^2 (1-\phi)^2}, \tag{4.2}$$

where $\phi \in (0,1)$ is the void fraction or porosity of the porous medium; S_{cp} is the specific area (the ratio of the surface area to the volume of the solid fraction of the porous medium); and K_{oz} is the Kozeny constant (Carman proposed a value of 5 for K_{oz} for porous media composed of packed spherical particles [47]). The velocity within the pores, $U_{\text{p}}(T)$, is related to the superficial Darcy velocity $U(T)$ via porosity ϕ as

$$U(T) = \phi U_{\text{p}}(T). \tag{4.3}$$

Inspired by a model for so-called "cake filtration", in which a "caking layer" of sieved particles forms on the upstream surface of a regular membrane filter acting as an additional filter in series with the membrane [51], we propose the following simple fouling model, which assume that removal of each of the impurity species is due to reaction between impurity particles and the porous medium, and that the reaction occurs at a rate proportional to the local particle (impurity) concentration and the local reactive porous material surface concentration. In addition we assume the two impurity particle types are transported independently by the solvent and do not interact with each other:

$$U_{\text{p}} \frac{\partial C_i}{\partial X} = -\Gamma_i C_i E, \qquad C_i(0,T) = C_{i,0}, \qquad 0 \le X \le D,\, T \ge 0; \quad i = 1,2, \tag{4.4}$$

$$\frac{\partial E}{\partial T} = -\sum_{i=1}^{2} \Xi_i C_i E, \qquad E(X,0) = E_0, \qquad 0 \le X \le D,\, T \ge 0, \tag{4.5}$$

where $C_i(X,T)$ is the concentration (mass per unit volume of solute) of type i impurity particles; Γ_i is a particle deposition coefficient for type i particles; $E(X,T)$ is the

concentration of the reagent on the surface of the granular material (e.g., coating on the sand); and Ξ_i is the reaction rate between particle type i and the reactive porous medium. The concentrations of impurity in the feed, $C_{i,0}$, and the initial reagent concentration E_0, are assumed to be specified constants. We assume further that the particle deposition rate is proportional to the rate of particle reaction with the porous material, i.e. $\Gamma_1/\Gamma_2 = \Xi_1/\Xi_2$.

4.3.1 Non-dimensionalization

We assume in the following that feed at constant flux $U = U_0$ is passed through the column throughout the simulated filtration. We non-dimensionalize the variables in our model (4.1)–(4.5) using the following scalings, with lower-case fonts indicating the dimensionless variables:

$$u = \frac{U}{U_0} = 1, \quad u_{\mathrm{p}} = U_{\mathrm{p}}\frac{\phi}{U_0} = 1, \quad p = P\frac{K}{U_0 D\mu}, \tag{4.6}$$

$$x = \frac{X}{D}, \quad c_1 = \frac{C_1}{C_{10}}, \quad c_2 = \frac{C_2}{C_{10}}, \tag{4.7}$$

$$e = \frac{E}{E_0}, \quad t = \frac{T}{T_0}, \quad \text{with} \quad T_0 = \frac{1}{\Xi_1 C_{10}}. \tag{4.8}$$

The resulting non-dimensionalized equations are as below: Equations (4.1)-(4.5) become

$$1 = \frac{\partial p}{\partial x}, \qquad 0 \le x \le 1, \tag{4.9}$$

$$\frac{\partial c_1}{\partial x} = -\gamma_1 c_1 e, \qquad c_1(0,t) = 1, \tag{4.10}$$

$$\frac{\partial c_2}{\partial x} = -\gamma_2 c_2 e, \qquad c_2(0,t) = \xi, \tag{4.11}$$

$$\frac{\partial e}{\partial t} = -(c_1 + \frac{\gamma_2}{\gamma_1}c_2)e, \qquad e(x,0) = 1, \tag{4.12}$$

where $\xi = C_{20}/C_{10}$ and $\gamma_i = \Gamma_i E_0 D\phi/U_0$.

We explain briefly how we solve this system of equations numerically: at the initial time step, we know $e(x,0) = 1$, so we can solve for $c_1(x,0)$ and $c_2(x,0)$ using

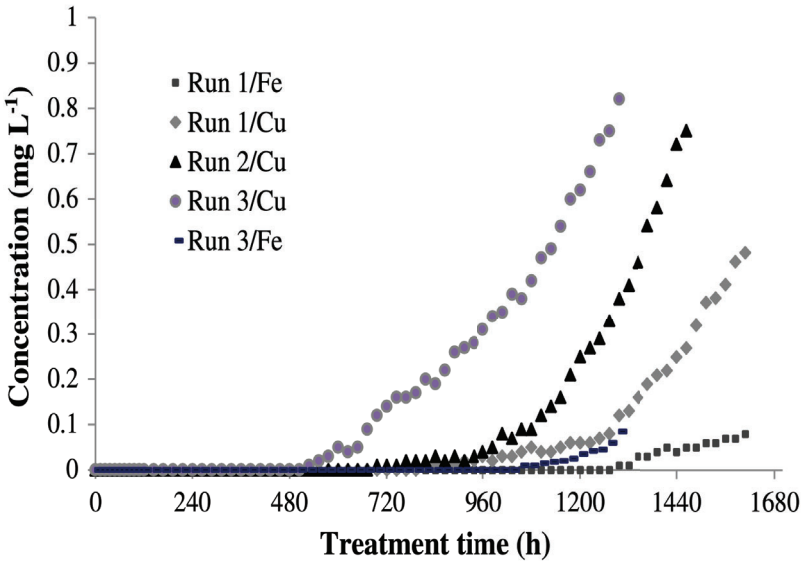

Figure 4.2 Experimental results from Acheampong & Lens [1]. Reproduced with permission.

Equations (4.10), and (4.11). We then update e at the next timestep using Equation (4.12) and $c_1(x, 0)$ and $c_2(x, 0)$ just found. Then we can solve for c_1 and c_2 at the new timestep, and repeat the process until the desired termination time is reached.

4.4 Results

We demonstrate the applicability of our model by parameter fitting to a particular experimental dataset due to Acheamphong & Lens [1], which investigates the feasibility of using coconut shell and iron oxide coated sand to filter and purify gold mining wastewater that contains multiple species of toxic heavy metal ions and cyanide, before discharging the filtrate to the environment. This study is relevant to our model as multiple contaminants (different species of particles to be removed) are present in the feed, and the removal of the contaminant is through reaction between contaminant (toxic heavy metal ions and cyanide) and reactive porous material (coconut shell and iron oxide coated sand). The experimental results are reproduced in Figure 4.2, and show the concentrations of two key contaminants, Cu^{2+} and Fe^{3+}

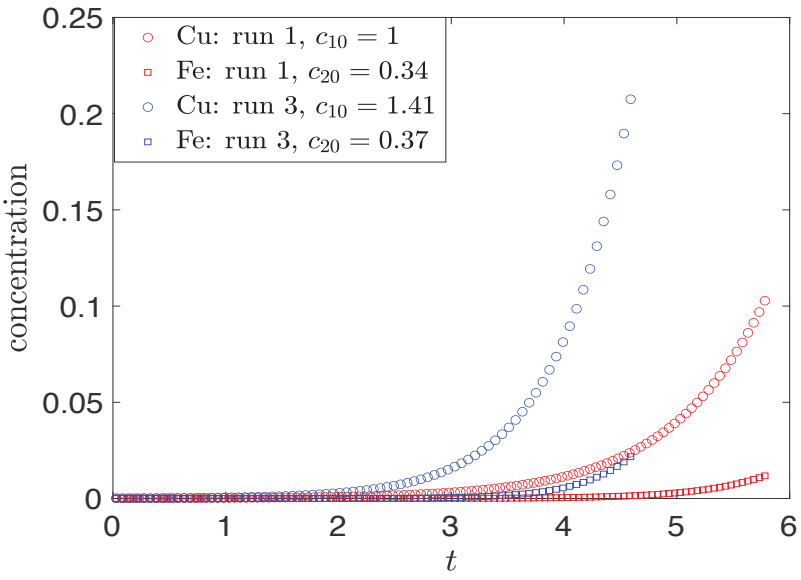

Figure 4.3 Model simulation with parameter values $\gamma_1 = 10, \gamma_2 = 15$.

ions, in the filtrate as the filtration progresses. Three sets of experiments are shown, indicated by Run 1, Run 2 and Run 3, with varying concentrations of contaminants in the feed. For Run 2, Fe^{3+} was not detected at the outlet of the filtration column, and is omitted from the plot.

The remainder of this section is organized as follows: In §4.4.1, we first generate artificial data using our model, qualitatively similar to the real data in Figure 4.2, to demonstrate how the optimization routine we developed in our earlier work [58, 59] can be reliably applied to determine best fit parameter values. We then present sample results from our model prediction with parameter values optimally fitted to the real experimental data in §4.4.2.

4.4.1 Parameter fitting using optimization

Before attempting a quantitative fit to real data we first show how our optimization routines can be used to reliably find parameters that provide the best fit to a given experimental dataset. Figure 4.3 shows two sets of simulations generated using our model, in terms of nondimensional quantities. The non-dimensionalized feed

concentrations c_{10} and c_{20} were obtained using the concentration of Cu from Run 1 in the experiment shown in Figure 4.2 as a base scale. We denote Cu ions as species 1 particles and Fe ions as species 2, in the notation of our model. Values $\gamma_1 = 10, \gamma_2 = 15$ are used for this simulation, chosen (via trial and error) to give results qualitatively similar to the real data (note that we purposely chose parameters in the ratios $\gamma_1 : \gamma_2 = 2 : 3$, with the consideration that in the experiment, the copper ions contain 2 positive charges (Cu^{2+}) while the iron contains 3 (Fe^{3+}). The qualitative similarity provides encouragement that our model could be useful for predicting experimental results if the parameter values γ_1 and γ_2 are chosen appropriately.

We next demonstrate how our optimization routines developed earlier can be used to realize the parameter fitting. To do this we generate simulated data by adding noise to the sample model results shown in Figure 4.3; see Figure 4.4(a). To test robustness of our parameter fitting routine we use two common types of noise: we add response-dependent Gaussian noise to the Fe data (noise amplitude proportional to the data values) and fixed-amplitude Gaussian noise to the Cu data. A successful parameter fitting routine should be able to fit our model to this simulated noisy data, and should find values of γ_1 and γ_2 very close to the values used to generate the initial simulations of Figure 4.3. We proceed as follows: We set up an objective function that numerically solves our model for given γ_1, γ_2 values and the returned value for the objective function is the squared difference between the solved value and the input noisy data. The parameter fitting problem can be cast as the following optimization problem:

Minimize

$$J(\gamma_1, \gamma_2) := \int_{t=0}^{t_f} dt \sum_{i=1,2} [c_i(1,t) - \text{data}_i(t)]^2 \tag{4.13}$$

subject to Equations (4.9)-(4.12), **and**

$$\gamma_i \geq 0, \quad i = 1, 2$$

$$t_f \quad \text{specified},$$

where $c_i(1,t)$ are the concentrations for each type of particles at the filtration column outlet at each time t, determined from Equations (4.9)-(4.12), data_i is the noisy data for each type of particle i, and t_f is the termination time for the filtration. If the method works, then with a low level of noise added to our model predictions, we should be able to recover the parameter values used to generate the noisy data. Figure 4.4(b) shows the plot for the parameter values found using our optimization routine with just 100 searching points. The values found in this test ($\gamma_1 = 10.0, \gamma_2 = 15.4$) are indeed very close to the original parameter values used to generate the data ($\gamma_1 = 10, \gamma_2 = 15$). We note that the approach is flexible, capable of fitting multiple data sets with varying size (vector size) in the same run.

4.4.2 Fitting the model to the real data

In this section, we use the optimization approach outlined above to find the best parameter values to model the experimental results presented by Acheampong & Lens [1]. When we deal with the real experimental data, there are two additional points to address: 1) the data are dimensional quantities, which require proper scaling to be comparable to our dimensionless mathematical model; 2) the data are discrete and when rescaled, are given at time intervals much larger than our numerical model computational timestep.

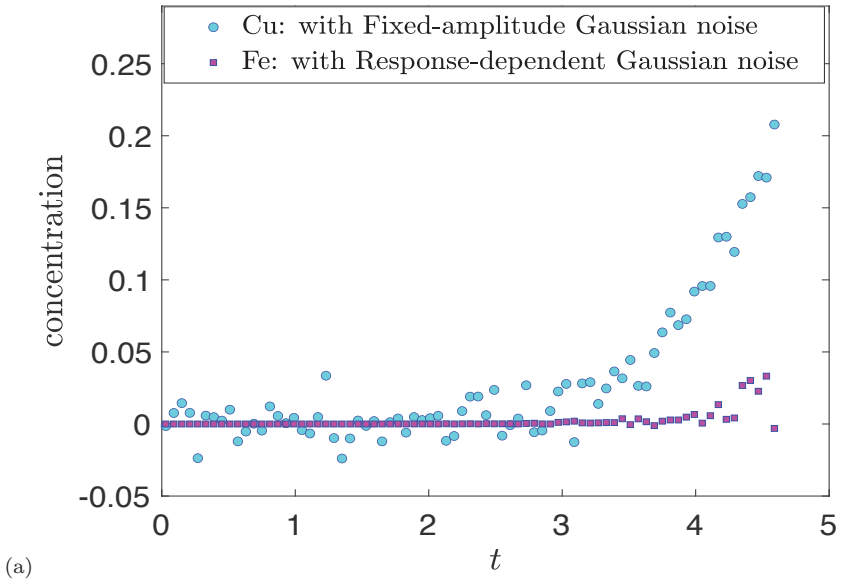

(a)

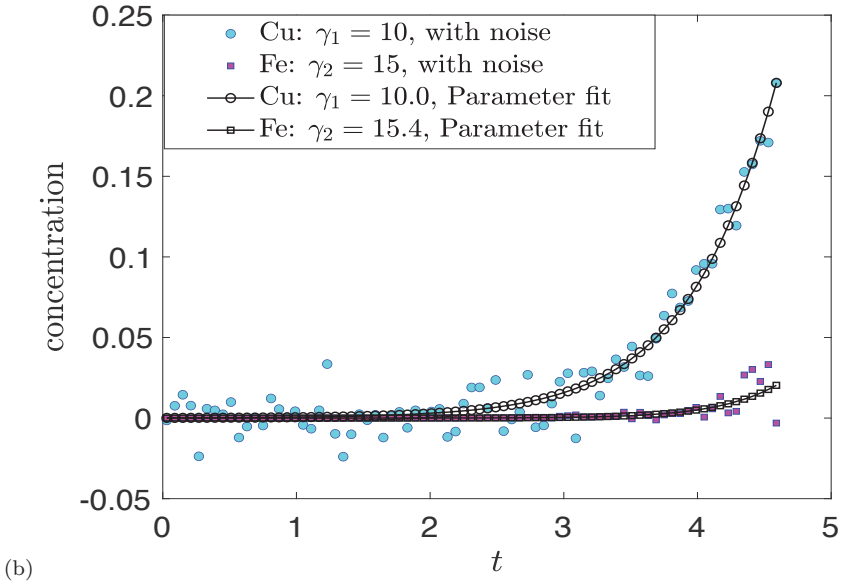

(b)

Figure 4.4 (a) Model prediction with added noise, parameter values fixed at $\gamma_1 = 10, \gamma_2 = 15, c_{10} = 1.41, c_{20} = 0.37$. (b) Parameter fitting for the noisy data using optimization.

Table 4.1 Dimensional Parameter Description and Values from Literature [1]

Parameter	Description	Value & Units
D	Depth of filtration column	150 cm
E	Reagent concentration on the surface of granular material	unknown kg/m^2
Q	Fixed flow rate for operation	150 ml/min
U_0	Fixed flux rate based on the fixed porous medium geometry	0.5 cm/min
K	Representative membrane permeability	unknown m^2 (very variable)
C_{i0}	Initial concentration of type i particles in feed	$C_{10} = 5.65$ mg/L for Run 1
Γ_i	Type i particle deposition coefficient	unknown m^2/s
Ξ_i	Reaction rate of type i particles to the reagents	unknown m^3/(kg $\cdot$ s)

For the second issue, one approach is to use matching tools to search the corresponding model prediction for each data point collected from the experiment. An alternative is to use interpolation tools to generate a smooth approximation to the experimental data, and use this function to generate data to compare with our model prediction. This is the approach we take; the experimental data are interpolated by polynomial functions of degree 10 using `MATLAB`®'s `polyfit` algorithm as shown in Figure 4.6(a), indicated by "Polyfit" in the legend. The raw data points were extracted using the open source software WebPlotDigitizer [50].

For the scaling issue with the raw data, we know the correct scale for the concentrations as we used the experimental value in the feed for scaling, see table 4.1. However, the time scale implicitly depends on the parameter γ_1, which is to be found using the raw data. Our approach is to take the time scale as an additional fitting parameter, and modify the objective function, which now simulates our model for any given time scale T_0 and parameter values γ_1, γ_2, and outputs the summation of square difference (after proper scaling) between model prediction and raw data generated by the polyfit function at each time step dictated by the raw data. This parameter fitting problem can be cast as the following optimization problem:

Minimize

$$J(\gamma_1, \gamma_2, T_0) := \int_{t=t_1}^{t_f} dt \sum_{i=1,2} [c_i(1,t)C_{10} - (\text{polyfit data})_i(tT_0)]^2 \tag{4.14}$$

subject to Equations (4.9)-(4.12), **and**

$$\gamma_i \geq 0, \quad i = 1, 2$$

$$T_0 > 0,$$

$$t_1 = T_1/T_0, \ t_f = T_f/T_0,$$

$$T_1, T_f \quad \text{specified based on raw data.}$$

Here $c_i(1,t)$ are the model-predicted concentrations for each type of particles at the filter outlet at each time t, which we find from Equations (4.9)-(4.12); $(\text{polyfit data})_i$ are the data values generated by the polynomial function obtained from the raw data using polyfit for each type of particle i; T_0 is the time scale (see Equation (4.8)); and based on the raw data we determine the fitting range for the starting time T_1 and end time T_f.

The optimization routine is as outlined in Section 4.4.1. In fitting to the real data we increased the number of searching points to compensate for the increased number of parameters to be optimized. The model predictions with the optimized parameters (indicated by legend "Parameter fit") are shown alongside the experimental data in Figures 4.5(b) and 4.6(b) for both sets of experimental data (Run 1 and Run 3). Parameter fit curves are generated using our model (after proper scaling) with optimized parameter value $\gamma_1 = 10.6, \gamma_2 = 13.8, T_0 = 261$ for Run 1 and $\gamma_1 = 9.7, \gamma_2 = 16.0, T_0 = 300$ for Run 3. Our parameter fitting indicates the variation of the porous material in terms of reactivity with the particles is significant, which may result from difference of porous material properties, such as packing density, granular size, or coating material, etc.

We first fit the experimental data from Run 1, in which both Cu and Fe have lower concentrations in comparison to Run 3. The results show in Figure 4.5 indicate that for this dataset, the parameter fitting routine achieves excellent agreement between the experimental results and our model predictions, see Figure 4.5. However, for data from Run 3, where contaminant concentrations in the filtrate are higher throughout, we observe that our model predicts the Fe concentration very well, but does not accurately describe the Cu concentration in the filtrate for a significant portion of the filtration duration, see Figure 4.6.

Our model is very simple, so there are many possible reasons for the relatively poor agreement in this case, but one possible explanation may be as follows. In formulating our model, we assume that at each stage, the available surface concentration of the reactive porous material is the same for both ion types, which is reasonable for the early stage of the filtration where we see neither particle type is detected in the filtrate (e.g., from $T = 0$ to $T = 500$), or for dilute ion concentrations. However, as the filtration proceeds and the reactive material is used up, the surface concentration may change more significantly after one ion reacts with the porous material. If there is a preferable ion for the reaction, then the other type of ion will suffer from the reduced surface concentration, which could be manifested as a deterioration in retention of the less favored ion (this could be viewed as a type of 'screening effect'). From the raw data, it seems likely that Fe is preferred for reaction with the porous material, and we see the retention deterioration shows much earlier for the Cu ions. This observation indicates that we may need to modify our model to account for differences in reaction rates between different ion types. For data from Run 1, since the concentrations for both Cu and Fe are lower in comparison with Run 3, the screening effect may not be appreciable, which leads to much better fitting.

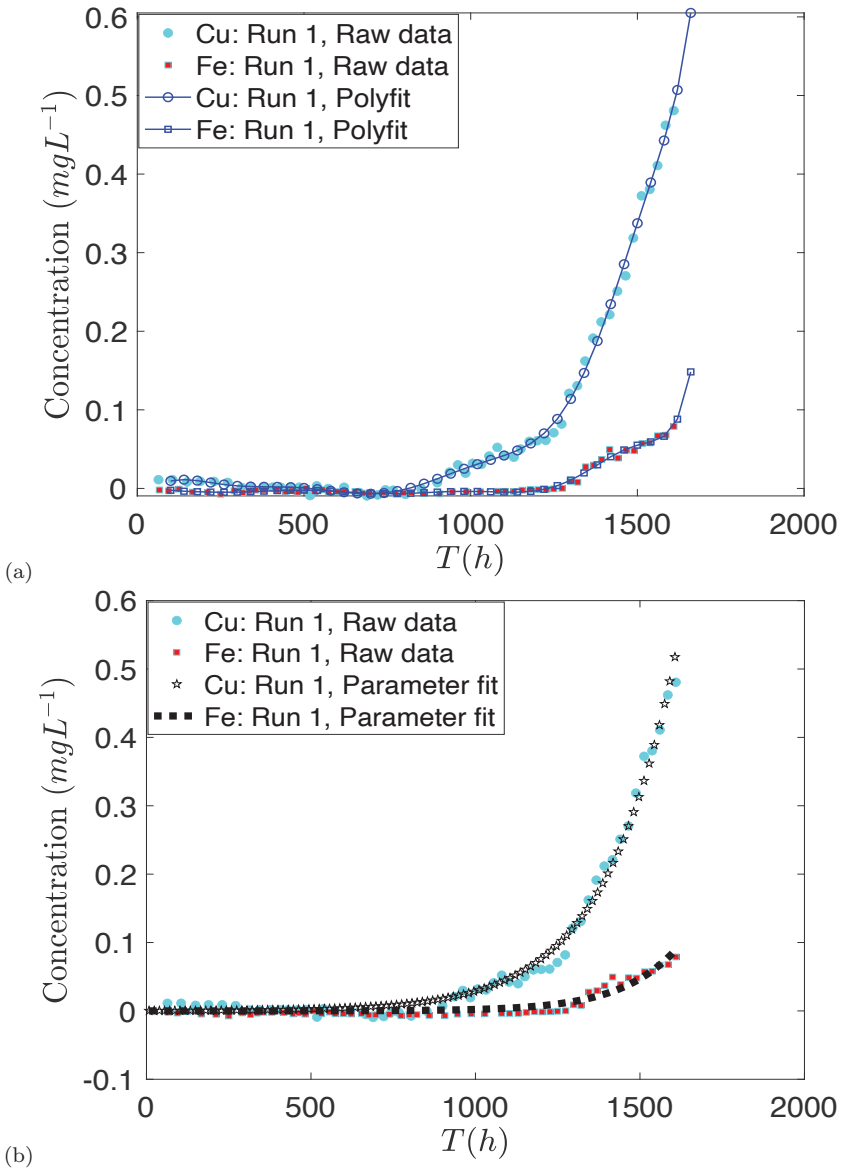

Figure 4.5 (a) Polynomial fitting for the raw data from experiment [1] Run 1. (b) Parameter fitting for data from experiment [1] using optimization. Parameter fit curves are generated with optimized parameter value $\gamma_1 = 10.6, \gamma_2 = 13.8, T_0 = 261$.

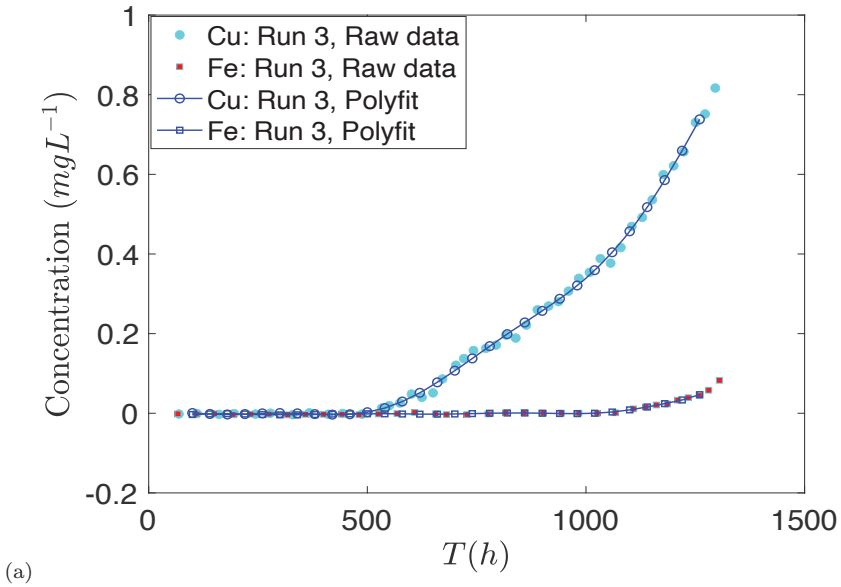

(a)

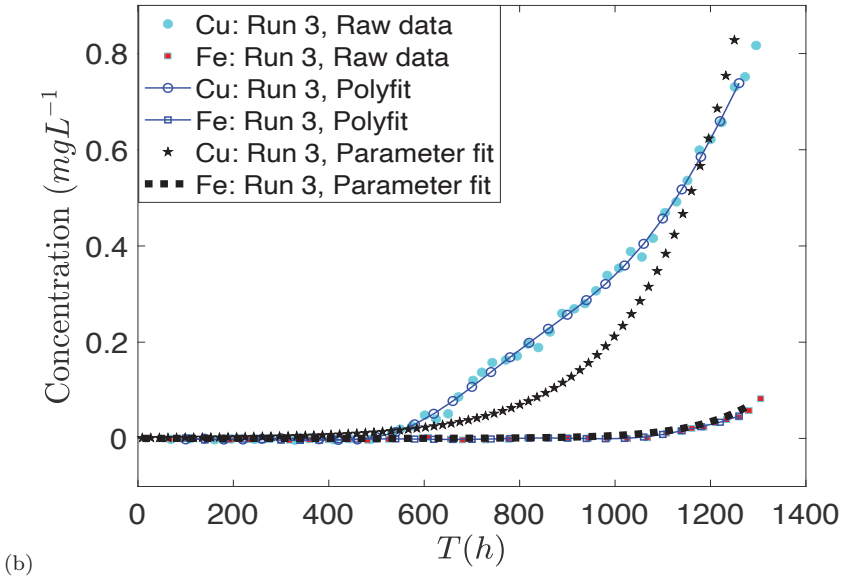

(b)

Figure 4.6 (a) Polynomial fitting for the raw data from experiment [1] Run 3. (b) Parameter fitting for data from experiment [1] using optimization. Parameter fit curves are generated with optimized parameter value $\gamma_1 = 9.7, \gamma_2 = 16.0, T_0 = 300$.

4.5 Conclusions and Future Study

In this preliminary work, we presented a simple mathematical model for reactive particle removal using a chemically reactive porous material. We demonstrated the applicability of our model by fitting to experimental data using parameter values estimated from the raw data. Our optimization routines developed in our earlier work prove to be useful for finding the optimal parameter values to best fit the experimental data. The discrepancy between our model predictions and the raw data indicates that we may need to consider taking account of the hypothesized "screening effect" to make this model more applicable to real situations. In addition, in this model we assume only simple first-order reaction kinetics, and certainly more complicated models including higher-order kinetics could be proposed if the experimental data indicate the necessity for doing so.

CHAPTER 5

CONCLUSIONS AND FUTURE WORK

In this final Chapter we summarize the main findings and insights gained through our investigations in Section 5.1, with a focus on highlighting those results most relevant to applications. We then discuss briefly some open questions and possible future work that we consider is worth pursuing in Section 5.2.

5.1 Summary and Conclusions

In Chapter 2, we formulated a mathematical model for evaluating the performance of a pleated membrane filter, with variable internal pore structure within the membrane. The relative simplicity of our model, achieved via asymptotic analysis that couples a pore-scale model for flow within the membrane to an outer macroscale model for flow in the region between pleats, allows for quick simulations of filtration all the way to final pore-blocking, which in turn allows us to carry out the optimization of the filter pore profile for a common filtration objective (maximizing throughput over the filter lifetime with a specified particle removal constraint that must be satisfied) and operating condition (constant driving pressure); see Section 2.4.2. For this filtration objective and operating condition, we are able to use our model to find (numerically) the optimal initial pore shape within a restricted class (low-order polynomials) of such shapes. Our results indicate that this optimization should be sufficient for most practical applications: as the degree of the polynomial increases from 1 to 3 convergence of the results (presumably to some global optimum) appears rapid.

We also briefly explored, in Section 2.4.4, the impact on filtration performance of (unavoidable) in-plane and in-depth variations to the desired (optimal) pore geometry. Our investigations for in-plane variations indicate that our optimization techniques could still be useful if the tolerance in pore-size variation is well-characterized, and

sufficiently small. However our investigations of in-depth pore shape variations indicate that particle removal capability of the membrane can be significantly impacted, even by quite small variations, and maintaining the optimized pore shape will be critical for achieving the highest total throughput $\mathcal{J}(t_f)$ while simultaneously satisfying the particle removal requirement. Though these conclusions hold strictly only for membranes with simple "track-etched" pore structure, we anticipate that they may be generalizable to membranes with more complex pore structure if we associate pore shape variations with general porosity variations in the membrane's cross-section or depth.

A significant observation from our simulations of Chapter 2 is that, under certain conditions, the concentration of impurity particles in the filtrate may *increase* after the filtration starts — that is, particle removal capability of the membrane may actually deteriorate in the early stages of the filtration. This phenomenon, which is known to occur experimentally (see, for example, Jackson *et al.* [32]), has not, to the best of our knowledge, been observed in earlier theoretical studies of adsorptive fouling. However, the results of Jackson *et al.* in fact show monotone deterioration in particle retention after onset, in contrast to our results which indicate an eventual improvement in retention as significant fouling occurs and the membrane resistance increases. This important qualitative difference indicates that additional refinements to our model may be needed to provide a more complete picture of filter performance.

In Chapter 3, we proposed a simplified mathematical model for filtration of feed containing multiple species of particles. Here, only "dead-end" filtration, where the flow of feed is always perpendicular to the planar membrane, is considered. For the case with just two particle species, two important model parameters are identified and investigated to elucidate their effect on separation and optimal filter design: ξ, the concentration ratio of the two particle types in the feed, and $\beta = \Lambda_2\alpha_2/(\Lambda_1\alpha_1)$, the ratio of the effective particle deposition coefficients for the two particle types. A

number of optimization problems for maximizing the mass yield of one particle species in the feed, while effectively removing the other, are formulated, under both constant pressure and constant flux driving conditions. For filtration driven by a constant pressure drop, we find that the optimized pore profile is always of V-shape (pores widest at the upstream membrane surface), which is in agreement with our earlier findings (Chapter 2; [59]) for single-particle-species filtration (where the goal is to maximize total throughput of filtrate over the filter lifetime while removing a sufficient fraction of impurity). For filtration driven by a constant flux, the optimized pore profile may take either a V-shape or a Λ-shape depending on the particle composition ratio and the amount of feed considered for the optimization scenarios.

To increase the appeal and utility of our model for filter design applications, we proposed new objective functions (the fast optimization method) based on evaluating key quantities at the initial stage of the filtration. Due to the simpler forms of the proposed objectives, we find empirically that our fast method can be carried out with a relatively small number of initial search-points in design parameter space (compared with the slow method, which requires that a large number of simulations be run through to filter failure time). The proposed fast method is approximately 100 times faster than the naive slow method.

Effective separation in a single-stage filtration is typically only achieveable at the expense of short filter lifetime and inefficient filter use (most of the filter remaining only very lightly fouled). We were therefore motivated to propose an alternative multi-stage filtration approach to maximize the mass yield per filter while achieving effective separation. Using this approach we were able to show that the mass yield per filter could be as much as two-and-a-half times that produced by the optimal single stage filtration, with higher product purity also. An additional advantage is that the filter optimized for multi-stage filtration also requires less material to manufacture, having higher porosity than one otimized for a single-stage filtration.

Multi-stage filtration has been utilized in industry [15] and reported experimentally [1, 40]; however, to our best knowledge, little attention has been paid to optimizing this process from the theoretical side. We hope that our work will inspire further systematic studies into this promising approach.

5.2 Future Work

Our results in Chapter 2 indicate that the optimization approach converges quite rapidly as the degree of the polynomial describing the pore radius depth variation is increased. In our study we implemented optimization using polynomials of degree 1, 2 and 3, i.e., up to four parameters (the polynomial coefficients) to be optimized; however, there is no guarantee that the optimization algorithm will converge to the global optimal solution. In addition, it may be desirable to explore more general pore shape. With an increasing number of parameters required by more general pore shape functions, a faster solver becomes necessary to find the optimizer in reasonable computation time. We are currently working on possible approaches to solve efficiently the general optimization problem in order to determine the optimum initial pore profile over all possible shapes (within the class of functions continuous over the depth of the pore).

Although we believe that our model as implemented in Chapter 2 represents a valuable step forward in helping manufacturers identify optimal membrane structures for given filtration scenarios, it does have several limitations, and there are many potential areas for improvement. First, we only consider very simple homogeneous feed solutions that contain identical particles. In most applications there will likely be multiple species in the same feed, and the objective with respect to which we optimize could also be more complicated: for example, to remove some species while allowing others to pass through. This question is partially addressed in our work presented in Chapter 3, though in a simpler flow geometry (dead-end filtration

rather than the pleated filter). Second, we only consider one fouling mechanism, while in practice there will often be multiple simultaneous mechanisms operating. It would not be difficult to include additional fouling mechanisms in our model; for example following the approach of Sanaei *et al.* [53]. We note, however, that the more mechanisms we include in our model, the more unknown parameters there will be, with correspondingly larger parameter space to be explored. In this case the optimization problems would need careful reformulation.

Third, even for such applications where standard blocking dominates, where our presented model should be adequate, there are further details that could and should be considered. For example, particles deposited on the clean membrane in the initial stages of filtration could lead to a shielding effect, and modify the physico-chemical interactions between particles and membrane, making it possibly more difficult for particles arriving at a later time to deposit on the membrane. We are currently pursuing this line of research. We hope that such modeling will provide new insights, in particular regarding the observed discrepancy in particle retention trends between our existing model predictions and the experimental results of Jackson *et al.* [32] noted above. Lastly, though we believe our simple "tubular pore" model should provide a good guide as to desirable membrane properties, there are certainly other types of pore structures that could be considered, e.g. regular branching pore structures [20, 52] or more general pore networks [19].

Our model in Chapter 3 extends to an arbitrary number of particle species in the feed; however, there are several important assumptions made in the model, which may require further investigation. First, we consider that the feed is sufficiently dilute and that different species of particles do not interact with each other. This assumption may not be valid as the number of particle species increases or for a feed characterized by large particle concentrations, which may require some averaging procedure for particles of similar but distinct physico-chemical properties. Particle-

particle interactions, if non-destructive, may be addressed by adding diffusion terms into the model, see e.g., [35].

In Section 3.4.4, we proposed a fast method for solving the optimization problems. The fast method shows excellent performance for the two species case but when the same objective function is used for the three species case, inconsistent results were observed. The success of the fast method with two species indicates that the chosen quantities (flux, particle concentration(s) in the filtrate) evaluated at an early stage of filtration have the potential to predict the final outcome; however, a better quantitative understanding of how such early-stage indicators signal final outcome is necessary for a reliable implementation of a fast method for feeds with more than two species of particles. Such a study may also help us gain more insight into our model and perhaps reveal some inherent monotonicity, despite the convoluted flow and fouling process. We intend to pursue this direction as future work.

As a part of our "proof of principle" study of multi-stage filtration, in Appendix B we present empirical numerical evidence showing that (with the chosen parameters and operating conditions) the highest yield is obtained using a four-stage filtration. However, we notice that the highest yield is not found when each stage filter is completely fouled, see Table B.1 together with Figures 3.8(b) and (c) for example; a somewhat counterintuitive finding. We believe that a systematic study on multi-stage filtrations would yield valuable insights into optimal filter usage, which may lead to some counterintuitive suggestions, such as not running a filtration through to filter exhaustion, especially for applications involving particles that one wishes to recover from the feed.

In Chapter 4, we presented our preliminary work for modeling filtration in reactive granular porous media. We expect this work, when complete, will lead to models that are much faster for performance prediction than the experimental

approach to which we compare, and that such models could be used to guide optimal operating conditions, predictions of filter lifespan, and improved filter design.

APPENDIX A

SYMMETRY IN THE PORE PROFILE EVOLUTION

In our simulations we observed that if the initial pore profile distribution is symmetric about $x = 1/2$ (i.e. $a_0(x, \tilde{y}) = a_0(1 - x, \tilde{y})$), the pores will retain this symmetry for the entire filtration process (i.e. $a(x, \tilde{y}, t) = a(1 - x, \tilde{y}, t)$, $0 \leq t \leq t_{\mathrm{f}}$), and we here present a proof for this. This symmetry arises from the coupled ODEs (2.40) and (2.41), reproduced below:

$$p_{0_{xx}}^{+}(x,t) = \frac{\Gamma(p_0^{+}(x,t) - p_0^{-}(x,t))}{r_{\mathrm{m}}(x,t)}, \quad p_0^{+}(0,t) = 1, \quad p_{0_x}^{+}(1,t) = 0, \tag{A.1}$$

$$-p_{0_{xx}}^{-}(x,t) = \frac{\Gamma(p_0^{+}(x,t) - p_0^{-}(x,t))}{r_{\mathrm{m}}(x,t)}, \quad p_0^{-}(1,t) = 0, \quad p_{0_x}^{-}(0,t) = 0, \tag{A.2}$$

(recall that the net membrane resistance $r_{\mathrm{m}}(x,t) = \int_{-1/2}^{1/2} a^{-4}(x, \tilde{y}, t) d\tilde{y}$). Observe first that, to show that the pore profile evolution is symmetric about $x = 1/2$ given the initial pore profile is symmetric about $x = 1/2$, is equivalent to showing that statement (A.3) holds:

$$r_{\mathrm{m}}(x,t) = r_{\mathrm{m}}(1-x,t) \quad \Longrightarrow \quad p_0^{+}(x,t) - p_0^{-}(x,t) = p_0^{+}(1-x,t) - p_0^{-}(1-x,t). \tag{A.3}$$

Note that

$$a(x, \tilde{y}, t) = a(1 - x, \tilde{y}, t) \quad \Longrightarrow \quad r_{\mathrm{m}}(x,t) = r_{\mathrm{m}}(1-x,t).$$

At $t = 0$, we have

$$a(x, \tilde{y}, 0) = a_0(x, \tilde{y}) = a_0(1 - x, \tilde{y}) = a(1 - x, \tilde{y}, 0) \quad \Longrightarrow \quad r_{\mathrm{m}}(x,0) = r_{\mathrm{m}}(1-x,0),$$

and $c(x, 1/2, 0) = c(1-x, 1/2, 0) = 1$ (in fact, $c(x, 1/2, t) = c(1-x, 1/2, t) = 1$ for $0 \le t \le t_{\mathrm{f}}$). From equation (2.42), reproduced below:

$$\frac{\partial c(x, \tilde{y}, t)}{\partial \tilde{y}} = \frac{\lambda a(x, \tilde{y}, t) c(x, \tilde{y}, t) r_{\mathrm{m}}(x, t)}{p_0^+(x, t) - p_0^-(x, t)}, \quad c(x, \frac{1}{2}, t) = 1, \tag{A.4}$$

we see that if $p_0^+(x, 0) - p_0^-(x, 0) = p_0^+(1-x, 0) - p_0^-(1-x, 0)$, then we have $c(x, \tilde{y}, 0) = c(1-x, \tilde{y}, 0)$. From equation (2.43), also reproduced below:

$$\frac{\partial a(x, \tilde{y}, t)}{\partial t} = -c(x, \tilde{y}, t), \quad a(x, \tilde{y}, 0) = a_0(\tilde{y}), \tag{A.5}$$

we then know that $a(x, \tilde{y}, \Delta t) = a(1-x, \tilde{y}, \Delta t)$ for the next time step $t = 0 + \Delta t$. Thus, the evolution will not break the symmetry as long as we have $p_0^+(x, t) - p_0^-(x, t) = p_0^+(1-x, t) - p_0^-(1-x, t)$ for each t. Hence, in the following we suppress the time dependence and focus on showing that (A.3) holds.

Proof. To show a function $f(x)$ is symmetric about $x = 1/2$, we just need to show $f(x) = f(1-x)$. In our case, $f(x) = p_0^+(x) - p_0^-(x)$.

Let $k(x) = \Gamma / r_{\mathrm{m}}(x) > 0$, where we know from the above that $k(x)$ is also symmetric about $x = 1/2$ if r_{m} is, i.e. $k(x) = k(1-x)$. The coupled ODEs (A.1) and (A.2) can then be written in the following form (here we use an overdot to denote d/dx):

$$\ddot{p}_0^+ = k(p_0^+ - p_0^-), \tag{A.6}$$

$$\ddot{p}_0^- = -k(p_0^+ - p_0^-), \tag{A.7}$$

$$p_0^+(0) = 1, \quad \dot{p}_0^+(1) = 0, \quad p_0^-(1) = 0, \quad \dot{p}_0^-(0) = 0. \tag{A.8}$$

From (A.6) and (A.7), we obtain the following:

$$p_0^+ = -p_0^- + Ax + B, \tag{A.9}$$

where A, B are arbitrary constants. Equations (A.9) and (A.8) then yield four conditions in terms of A and B:

$$p_0^+(1) = A + B, \quad \dot{p}_0^+(0) = A, \quad p_0^-(0) = B - 1, \quad \dot{p}_0^-(1) = A.$$

Now let $w(x) = [p_0^+(x) - p_0^-(x)] - [p_0^+(1-x) - p_0^-(1-x)]$. We claim that

$$w(x) = 0, \forall x \in [0, 1].$$

Checking the boundary conditions for $w(x)$ we find

$$\begin{aligned} w(0) &= A + 2B - 2, \\ w(1) &= -A - 2B + 2, \\ \dot{w}(0) &= A - A = 0, \\ \dot{w}(1) &= -A + A = 0. \end{aligned}$$

From the coupled ODEs (A.6), (A.7), (A.8) and the symmetry of $k(x)$, $w(x)$ must satisfy

$$\ddot{w}(x) = 2k(x)w(x), \tag{A.10}$$

$$\dot{w}(0) = 0, \dot{w}(1) = 0. \tag{A.11}$$

To show $w(x) \equiv 0$, we use a standard energy argument [2]. Multiplying (A.10) by w and integrating by parts, with the boundary conditions (A.11) applied, we obtain

$$\int_0^1 \dot{w}^2 + 2k(x)w^2 dx = 0.$$

Since $k(x) > 0$, it follows that $w \equiv 0$ on $[0, 1]$.

□

APPENDIX B

OPTIMAL RATIO FOR MULTI-STAGE FILTRATION

The observations of Figure 3.8 indicate there may be an optimal ratio between the number of filters to use at different stages of a multi-stage filtration, which would utilize each filter's filtration capacity as fully as possible, and minimize the loss of filtrate at each stage, ultimately maximizing the mass yield per filter. We used our model to conduct such an investigation, and compiled our findings in table B.1, which is also presented graphically in Figure B.1. At all filtration stages filters $F_{0.5}$, optimized to maximize the mass yield of type 2 particles while meeting a particle type 1 removal threshold $R = 0.5$, are used.

Figure B.1 shows, for each multi-stage filtration considered, the total mass yield per filter (Figure B.1(a)); the final purity k_2 of the filtrate (Figure B.1(b)); and the final cumulative particle removal ratios $\bar{R}_1(t_\mathrm{f}), \bar{R}_2(t_\mathrm{f})$ for the two particle types. We find that the maximal mass yield per filter is 0.013; the corresponding (four-stage) filtration is apparent as the global maximum of the mass yield per filter in Figure B.1(a). This maximum yield is also indicated in red font in table B.1, and is almost two and half times the yield obtained with a single-stage filtration optimized to maximize yield while immediately satisfying the purity constraint.

This four-stage filtration is illustrated schematically in Figure 3.9. We note that the higher mass yield per filter appears to be achieved at the expense of lowest purity $k_2 = 0.873$ among other multi-stage filtrations considered, with final cumulative particle 1 removal ratio $\bar{R}_1(\mathrm{t_f})$ just above 0.99 (see Figure B.1(b,c)), which makes sense as optimizers are generally found at the boundary of the feasible search space where one or more constraints are tight. However, the 2-stage local maximum simultaneously

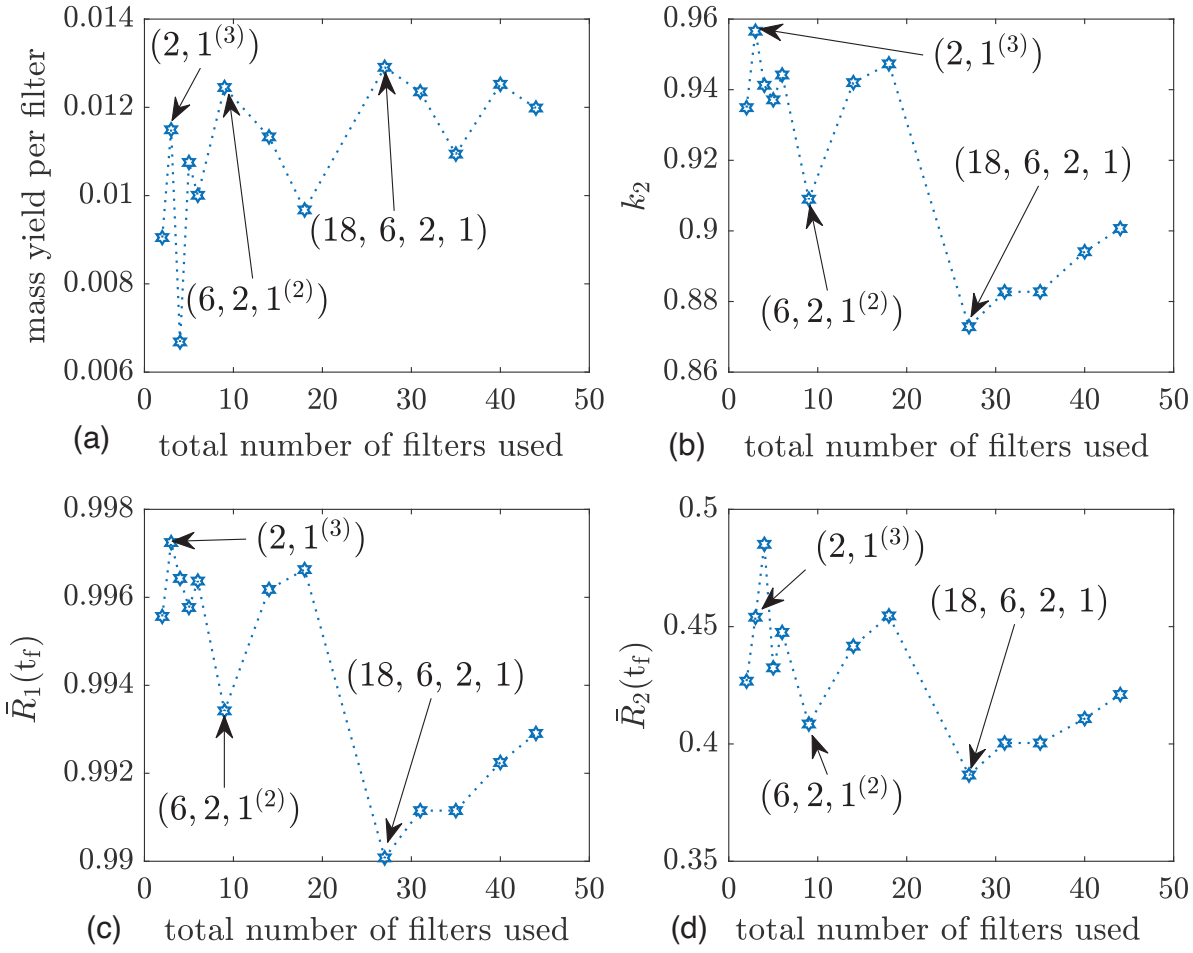

Figure B.1 (a) Mass yield per filter, (b) purity of type 2 particles (k_2), (c,d) final cumulative particle removal ratios for particle types 1 and 2 ($\bar{R}_1(\mathrm{t_f})$ and $\bar{R}_2(\mathrm{t_f})$) are plotted against the total number of filters used in each multi-stage filtration. The local maximum mass yields per filter for 2-stage, 3-stage and 4-stage filtrations are labelled with a list of values ($l_m^{(k)}$), representing the number of filters l_m used for stage m, and the number of times k each filter is used, listed in order of increasing m.

Table B.1 Comparisons of Multi-stage Filtrations (up to four stages are considered) with Differing Ratios of the Number (l_m) of Filters $F_{0.5,m}$ Used at Stage m

l_1	l_2	l_3	l_4	$c_{1\mathrm{acm}}(\mathrm{t_f})$	$c_{2\mathrm{acm}}(\mathrm{t_f})$	$j(\mathrm{t_f})$	**Mass Yield/Filter**
1	$1^{(4)}$	0	0	0.00399	0.0573	0.316	0.0090
2	$1^{(3)}$	0	0	0.00247	0.0546	0.631	0.012
3	$1^{(2)}$	0	0	0.00321	0.0515	0.519	0.0067
3	1	$1^{(3)}$	0	0.00380	0.0568	0.947	0.011
4	1	$1^{(3)}$	0	0.00327	0.0552	1.087	0.010
6	2	$1^{(2)}$	0	0.00592	0.0592	1.894	0.012
9	3	1	$1^{(2)}$	0.00343	0.0558	2.841	0.011
12	4	1	1^2	0.00303	0.0545	3.193	0.0096
18	6	2	1	0.00893	0.0589	5.683	0.013
21	7	2	1	0.00796	0.0600	6.386	0.012
24	8	2	1	0.00796	0.0600	6.386	0.011
27	9	3	1	0.00698	0.0589	8.501	0.012
30	10	3	1	0.00638	0.0579	9.108	0.011

The First Four Columns List Values $l_m^{(k)}$, with Superscripts (k) Indicating that Each Filter Is Used k Times. The Remaining Columns Show Final Cumulative Particle Concentration for Type 1 and Type 2 Particles, $c_{1\mathrm{acm}}(\mathrm{t_f})$ and $c_{2\mathrm{acm}}(\mathrm{t_f})$, Total Throughput $j(\mathrm{t_f})$ and Compound 2 Mass Yield per Filter. The Global Maximum Mass Yield per Filter Is Highlighted in Red Font.

achieves high mass yield per filter together with the highest purity, $k_2 = 0.997$, which indicates that this two-stage filtration may be useful to achieve high mass yield without sacrificing the purity of the final product.

APPENDIX C

MULTIPLE SPECIES

In this section, we present some sample results for feed containing more than 2 species of particles. We non-dimensionalize our model (3.2)–(3.7) using the same scalings as Section 3.3.3.1 for most quantities, with the following variations:

$$c_i = \frac{C_i}{\sum_i C_{0i}} \text{ and } t = \frac{T}{T_0}, \text{ with } T_0 = \frac{W}{\Lambda_1 \alpha_1 \sum_i C_{0i}}. \tag{C.1}$$

Eqns. (3.13)-(3.15) remain unchanged, and Eqns. (3.6)-(3.7) take the form

$$u_{\mathrm{p}} \frac{\partial c_i}{\partial x} = -\lambda_i \frac{c_i}{a}, \quad c_i(0,t) = \xi_i \text{ with } \sum_i \xi_i = 1, \tag{C.2}$$

$$\frac{\partial a}{\partial t} = -\sum_i \beta_i c_i, \; a(x,0) = a_0(x), \tag{C.3}$$

where $\lambda_i = 32\Lambda_i D^2 \mu/(\pi W^3 P_0)$ is the deposition coefficient for particle type i, $\xi_i = C_{0i}/\sum_i C_{0i}$ is the concentration ratio of type i particles, $\beta_i = \Lambda_i \alpha_i/(\Lambda_1 \alpha_1)$ is the effective particle deposition coefficient for particle type i (relative to particle type 1), and $a_0(x)$ is the pore profile at initial time $t = 0$. To illustrate the model we consider an optimization problem similar to **Problem 2**. For definiteness, we consider a feed containing three species of particles, with type 1 and type 3 the particles to be removed and type 2 the particles to be recovered from the feed. The goal is again to maximize the mass yield for type 2 particles ($c_{2\mathrm{acm}}(t_{\mathrm{f}})j(t_{\mathrm{f}})$) while achieving effective separation. Similar to our earlier approach in Section 3.5.1.2, we could define *effective separation* based on the final cumulative particle removal ratios as $\bar{R}_1(t_{\mathrm{f}}) \geq 0.99$, $\bar{R}_2(t_{\mathrm{f}}) \leq 0.5$, and $\bar{R}_3(t_{\mathrm{f}}) \geq 0.9$. Noticing the definition gets clumsy with increasing number of particle species, here we propose an alternative way of defining effective separation,

in observation of close relationship between purity and final particle removal ratios [see Equation (3.37)], with a focus on the particle that we would like to recover. We define *effective separation* for species i (the species we wish to recover) as retaining at least 50% of particle type i in the final filtrate (i.e., $\bar{R}_i(t_f) \leq 0.5$) with purity of at least 85% (i.e., $k_i \geq 0.85$). We note here, with this definition, the particle removal ratios for other particles (to be removed from the feed) can be systematically determined, when we are given the initial particle concentration for each species, using Equation (3.37).

In Figure C.1 we present optimization results for three feeds of different particle composition ratios (indicated by the different ξ_i values for each curve) with $\beta_1 = 1$, $\beta_2 = 0.1, \beta_3 = 0.5$, $\lambda_1 = 1$: (a) flux vs throughput, (u, j) plot; (b) accumulative type 1 particle concentration vs throughput, $(c_{1\text{acm}}, j)$ plot; (c) accumulative type 2 particle concentration vs throughput, $(c_{2\text{acm}}, j)$ plot; (d) accumulative type 3 particle concentration vs throughput, $(c_{3\text{acm}}, j)$ plot. The optimization was carried out using the slow method (similar to the slow method outlined for **Problem 2** in Section 3.4.3), and we find that the optimized pore profile takes a V-shape, as observed in our results for **Problem 2** in Section 3.5.1. The different feed composition does not significantly change the optimized pore profile. For higher concentrations of the heaviest-fouling particle (type 1 in this case) the pore closes faster with less total throughput observed in Figure C.1(a). We can see from Figures C.1(b) and (c) that the initial particle removal requirements are satisfied, though not sharp, in all three cases. We note in Figure C.1(d) that the particle removal constraint for type 3 particle is tight at the start of filtration, which indicates that this constraint is the most demanding. This makes sense as we are requiring a relatively high removal ratio (90%), with a much lower particle deposition coefficient compared to particle type 1 ($\lambda_3 = \beta_3\lambda_1$ and $\beta_3 = 0.5$; in this simulation α_i is the same for each type of particles). In all three cases shown, effective separation is achieved by our definition, details are provided in Table

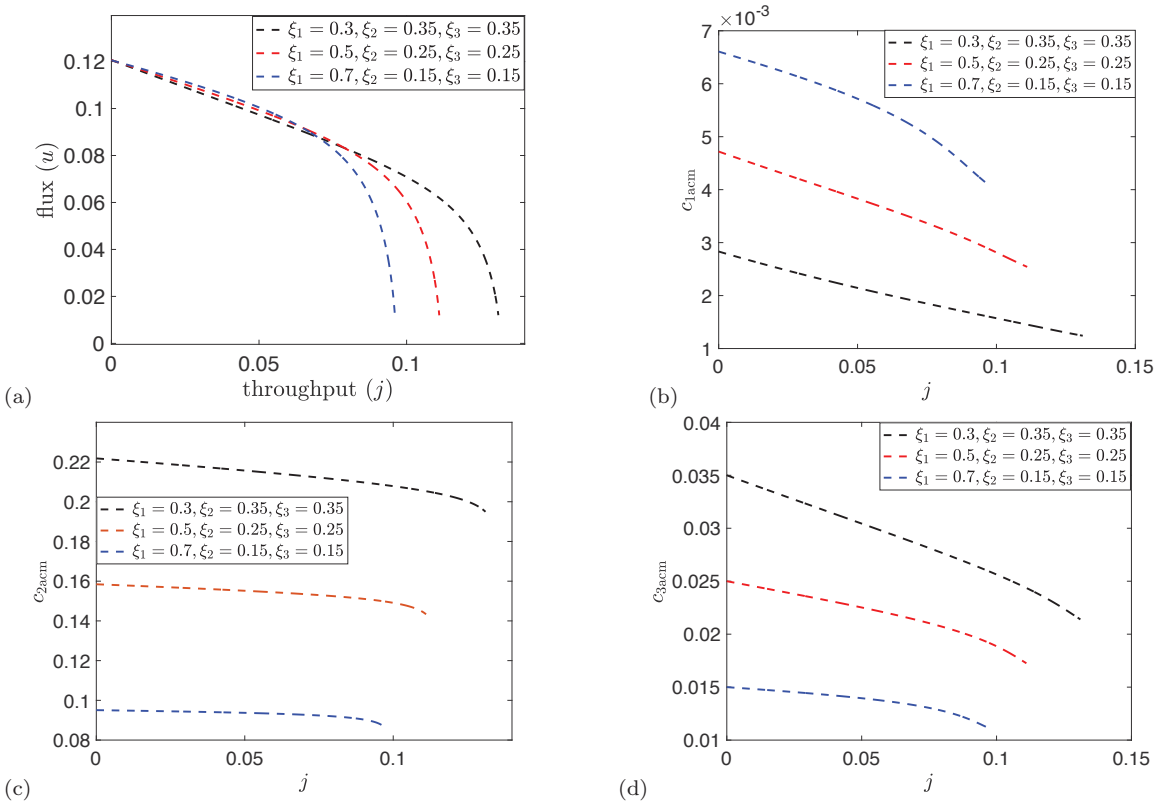

Figure C.1 Evolution of the optimized membrane pore for three different feeds (1) $\xi_1 = 0.3, \xi_2 = 0.35, \xi_3 = 0.35$, (2) $\xi_1 = 0.5, \xi_2 = 0.25, \xi_3 = 0.25$ and (3) $\xi_1 = 0.7, \xi_2 = 0.15, \xi_3 = 0.15$, with $\beta_1 = 1$, $\beta_2 = 0.1, \beta_3 = 0.5$, $\lambda_1 = 1$, $R_1(0) \geq 0.99$, $R_2(0) \leq 0.5$ and $R_3(0) \geq 0.9$: (a) (u, j) plot, (b) $(c_{1\mathrm{acm}}, j)$ plot, (c) $(c_{2\mathrm{acm}}, j)$ plot, (d) $(c_{3\mathrm{acm}}, j)$ plot.

C.1. Similar to the two species problem, the slow method for optimization takes about 40 minutes with 10000 searching points. Fast methods based on similar heuristics to those discussed in Section 3.4.4 were explored but found to give unreliable results for three particle species; further investigation is needed to speed up the optimization.

Table C.1 Three species feed filtration.

ξ_1	ξ_2	ξ_3	$\bar{R}_1(\mathrm{t_f})$	$\bar{R}_2(\mathrm{t_f})$	$\bar{R}_3(\mathrm{t_f})$	k_2	$j(\mathrm{t_f})$
0.3	0.35	0.35	0.996	0.443	0.939	0.896	0.131
0.5	0.25	0.25	0.995	0.427	0.931	0.879	0.111
0.7	0.15	0.15	0.994	0.416	0.925	0.850	0.096

We record ξ_i, particle ratios for each type of particles, $\bar{R}_i(\mathrm{t_f})$ the final cumulative particle removal ratio for particle type i, k_2 purity of type 2 particles in the final filtrate, $j(\mathrm{t_f})$ total throughput.

REFERENCES

[1] M. A. Acheampong and P. N. L. Lens. Treatment of gold mining effluent in pilot fixed bed sorption system. *Hydrometallurgy*, 141:1–7, 2014.

[2] N. I. Akhiezer. *The calculus of variations*. New York, New York: Blaisdell publishing company, a division of Random House, Inc., 1962.

[3] P. Apel. Track etching technique in membrane technology. *Radiat. Meas.*, 34.1:559–566, 2001.

[4] P. Bacchin, Q. Derekx, D. Veyret, K. Glucina, and P. Moulin. Clogging of microporous channels networks: role of connectivity and tortuosity. *Microfluid Nanofluid.*, 17:85–96, 2014.

[5] U. Beuscher. Modeling sieving filtration using multiple layers of parallel pores. *Chem. Eng. Tech.*, 33:1377–1381, 2010.

[6] B. Blankert, B. H. L. Betlem, and B. Roffel. Dynamic optimization of a dead-end filtration trajectory: Blacking filtration laws. *J. Membrane Sci.*, 285:90–95, 2006.

[7] G. R. Bolton, D. LaCasse, and R. Kuriyel. Combined models of membrane fouling: development and application to microfiltration and ultrafiltration of biological fluids. *J. Membrane Sci.*, 277:75–84, 2006.

[8] W. R. Bowen, J. I. Calvo, and A. Hernández. Steps of membrane blocking in flux decline during protein microfiltration. *J. Membrane Sci.*, 101:153–165, 1995.

[9] S. Boyd and L. Vandenberghe. *Convex optimization.* Cambrige University Press, Cambridge, United Kingdom, 2004.

[10] A. I. Brown. *An ultra scale-down approach to the rapid evaluation of pleated membrane cartridge filter performance*. PhD thesis, University College London, 2011.

[11] J. C. Chen, Q. Li, and M. Elimelech. In situ monitoring techniques for concentration polarization and fouling phenomena in membrane filtration. *Adv. Colloid Interface Sci.*, 107:83–108, 2004.

[12] G. Daufin, J.P. Escudier, H. Carrère, S. Beérot, L. Fillaudeau, and M. Decloux. Recent and emerging applications of membrane processes in the food and dairy industry. *Inst. Chem. Eng.*, 89:1094–1103, 2011.

[13] N. Debnath, A. Kumar, T. Thundat, and M. Sadrzadeh. Investigating fouling at the pore-scale using a microfluidic membrane mimic filtration system. *Nature: Scientific Reports*, 9, 2019.

[14] C. Duclos-Orsello, W.Y. Li, and C.C. Ho. A three mechanism model to describe fouling of microfiltration membranes. *J. Membrane Sci.*, 280:856–866, 2006.

[15] K. Elsaid, M. Kamil, E. T. Sayed, M. A. Abdelkareem, T. Wilberforce, and A. Olabi. Environmental impact of desalination technologies: A review. *Sci. Total Envir.*, 748:141528, 2020.

[16] P. Emami, S.P. Motevalian, E. Pepin, and Zydney A.L. Impact of module geometry on the ultrafiltration behavior of capsular polysaccharides for vaccines. *J. Membrane Sci.*, 561:19–25, 2018.

[17] S. Giglia and G. Straeffer. Combined mechanism fouling model and method for optimization of series microfiltration performance. *J. Membrane Sci.*, 417-418:144–153, 2012.

[18] H. P. Grace. Structure and performance of filter media. ii. performance of filter media in liquid service. *AIChE Journal.*, 2:316–336, 1956.

[19] B. Gu, L. Kondic, and L. J. Cummings. A graphical representation of membrane filtration. *ArXiv preprint*, ArXiv2106.03915, 2021.

[20] B. Gu, D. L. Renaud, P. Sanaei, L. Kondic, and L. J. Cummings. On the influence of pore connectivity on performance of membrane filters. *J. Fluid Mech.*, 902:A5, 2020.

[21] J. Hermia. Constant pressure blocking filtration law: application to power law non-newtonian fluids, trans. *Inst. Chem. Eng.*, 60:183–187, 1982.

[22] R. M. Hicks, E. M. Murman, and G. N. Vanderplaats. An assessment of airfoil design by numerical optimization. *NASA Report-TM-X-3092*, July 1974.

[23] C. C. Ho and A. L. Zydney. Effect of membrane morphology on the initial rate of protein fouling during microfiltration. *J. Membrane Sci.*, 155:261–275, 1999.

[24] C. C. Ho and A. L. Zydney. A combined pore blockage and cake filtration model for protein fouling during microfiltration. *J. Colloid interface Sci.*, 232:389–399, 2000.

[25] J. Hoslett, T. M. Massara, and S. Malamis. Surface water filtration using granular media and membranes: A review. *Sci. Total Envir.*, 639:1268–1282, 2018.

[26] O. Iliev, R. Kirsch, and S. Osterroth. Combined depth and cake filtration model coupled with flow simulation for flat and pleated filters. *Chem. Eng. Tech.*, 41:70–78, 2018.

[27] E. Iritani. A review on modeling of pore-blocking behaviors of membranes during pressurized membrane filtration. *Drying Tech.*, 31:146–162, 2013.

[28] E. Iritani and N. Katagiri. Developments of blocking filtration model in membrane filtration. *KONA Powder and Particle J.*, 33:179–202, 2016.

[29] C. R. Ison and K. J. Ives. Removal mechanisms in deep bed filtration. *Chem. Eng. Sci.*, 24:717–729, 1969.

[30] K. J. Ives. Rapid filtration. *Water Research Pergamon Press.*, 4:201–223, 1970.

[31] T. Iwasaki, J. J. Slade, and W. E. Stanley. Some notes on sand filtration. *American Water Works Association*, 29:1591–1602, 1937.

[32] N. B. Jackson, M. Bakhshayeshi, A. L. Zydney, A. Mehta, R. van Reis, and R. Kuriyel. Internal virus polarization model for virus retention by the Ultipor VF grade DV20 membrane. *BioTech. Prog.*, 30:856–863, 2014.

[33] X. Jin, T. Foller, X. Wen, M. B. Ghasemian, F. Wang, M. Zhang, H. Bustamante, V. Sahajwalla, P. Kumar, H. Kim, G. H. Lee, K. Kalantar-Zadeh, and R. Joshi. Effective separation of CO_2 using metal-incorporated rGO membranes. *Adv. Mater.*, 32, 2020.

[34] M. W. Jornitz. *Filter construction and design.*, volume 98. Springer, Berlin, Heidelberg, 2006.

[35] M. M. Kim and A. L. Zydney. Theoretical analysis of particle trajectories and sieving in a two-dimensional cross-flow filtration system. *J. Membrane Sci.*, 281:666–675, 2006.

[36] K. B. Kiradjiev, C. J. Breward, I. Griffiths, and D. W. Schwendeman. A homogenized model for a reactive filter. *SIAM J. Appl. Math.*, 81:591–619, 2021.

[37] C. Kloss, C. Goniva, A. Hager, S. Amberger, and S. Pirker. Models, algorithms and validation for opensource DEM and CFD-DEM. *Progress in Computational Fluid Dynamics*, 12, 2012.

[38] A. Kumar. Private Communication, 2014. Dr. Kumar was a researcher at Pall Corporation when this communication happened.

[39] D. A. Ladner, M. Steele, K. Weir, K. Hristovski, and P. Westerhoff. Functionalized nanoparticle interactions with polymeric membranes. *J. Hazardous Materials*, 211-212:288–295, 2012.

[40] Y. J. Lau, R. R. Karri, N. M. Mubarak, M. Khalid, P. Jagadish, E. C. Abdullah, S. Y. Lau, and H. B. Chua. Removal of dye using peroxidase-immobilized buckypaper/polyvinyl alcohol membrane in a multi-stage filtration column via RSM and ANFIS. *Envir. Sci. Pollution Research*, 27:40121–40134, 2020.

[41] H. Lee, D. B. Kwak, S. C. Kim, Q. Ou, and D. Pui. Influence of colloidal particles with bimodal size distributions on retention and pressure drop in ultrafiltration membranes. *Separation Purification Tech.*, 222:352–360, 2019.

[42] H. Lee, D. Segets, S. Süß, W. Peukert, and S. C. Chen. Liquid filtration of nanoparticles through track-etched membrane filters under unfavorable and different ionic strength conditions: Experiments and modeling. *J. Membrane Sci.*, 524:682–690, 2017.

[43] J. Lin, D. Bourrier, M. Dilhan, and P. Duru. Particle deposition onto a microsieve. *Phys. Fluids*, 21, 2009.

[44] Z. Liu, Z. Ji, J. Shang, H. Chen, Y. Liu, and R. Wang. Improved design of two-stage filter cartridges for high sulfur natural gas purification. *Separation Purification Tech.*, 198:155–162, 2018.

[45] J. Lohaus, Y. M. Perez, and M. Wessling. What are the microscopic events of colloidal membrane fouling? *J. Membrane Sci.*, 553:90–98, 2018.

[46] B. Ma, X. Li, B. Liu, P. Xing, W. J. Zhang, C. Wang, and Y. Chen. Effective separation and recovery of valuable components from CIGS chamber waste via controlled phase transformation and selective leaching. *ACS Sustainable Chem. and Eng.*, 8:3026–3037, 2020.

[47] R. F. Probstein. *Physicochemical Hydrodynamics*. Hoboken, New Jersey: Wiley-Interscience, 1994.

[48] M. Rebai, M. Prat, M. Meireles, P. Schmitz, and R. Baclet. Combined depth and cake filtration model coupled with flow simulation for flat and pleated filters. *Chem. Eng. Res. Design.*, 88:476–486, 2010.

[49] B. C. Ricci, C. D. Ferreira, A. O. Aguiar, and M. C. Amaral. Integration of nanofiltration and reverse osmosis for metal separation and sulfuric acid recovery from gold mining effluent. *Separation Purification Tech.*, 154:11–21, 2015.

[50] A. Rohatgi. Webplotdigitizer: Version 4.4, 2020. Available at `https://automeris.io/WebPlotDigitizer`. Retrieved on July 12, 2021.

[51] P. Sanaei and L. J. Cummings. Flow and fouling in membrane filters: effects of membrane morphology. *J. Fluid Mech.*, 818:744–771, 2017.

[52] P. Sanaei and L. J. Cummings. Membrane filtration with complex branching pore morphology. *Phys. Rev. Fluids*, 3:094305, 2018.

[53] P. Sanaei, G. W. Richardson, T. Witelski, and L. J. Cummings. Flow and fouling in a pleated membrane filter. *J. Fluid Mech.*, 795:36–59, 2016.

[54] G. Shi, Y. Shen, P. Mu, Q. Wang, Y. Yang, S. Ma, and J. Li. Effective separation of surfactant-stabilized crude oil-in-water emulsions by waste brick powders-coated membrane under corrosive conditions. *Green Chem.*, 2020.

[55] L. A. Spielman. Particle capture from low-speed laminar flows. *Ann. Rev. Fluid Mech.*, 9:297–319, 1977.

[56] D. D. Sun, 2019. Research photo from Darren Sun's website, Fouling on UF Membrane, available at `https://personal.ntu.edu.sg/ddsun/research.html`. Retrieved on July 12, 2021.

[57] X. Sun, D. M. Kanani, and R. Ghosh. Characterization and theoretical analysis of protein fouling of cellulose acetate membrane during constant flux dead-end microfiltration. *J. Membrane Sci.*, 320:372–380, 2008.

[58] Y. X. Sun, L. Kondic, and L. J. Cummings. Filtration with multiple species of particles. *ArXiv preprint*, ArXiv2106.15440, 2021.

[59] Y. X. Sun, P. Sanaei, L. Kondic, and L. J. Cummings. Modeling and design optimization for pleated membrane filters. *Phys. Rev. Fluids*, 5:044306, 2020.

[60] P. Sylvester, T. Milner, and J. Jensen. Radioactive liquid waste treatment at Fukushima Daiichi. *J. Chem. Tech. Biotech.*, 88:1592–1596, 2013.

[61] S. Ta'asan, G. Kuruvila, and M. D. Salas. Aerodynamic design and optimization in one shot. *AIAA*, 92-0025, 1992.

[62] C. Y. Tang, T. H. Chong, and A. G. Fane. Colloidal interactions and fouling of NF and RO membranes: a review. *Adv. Colloid Interface Sci.*, 164:126–143, 2011.

[63] E. M. Tracey and R. H. Davis. Protein fouling of track-etched polycarbonate microfiltration membranes. *J. Colloid Interface Sci.*, 167:104–116, 1994.

[64] M. Ulbricht. Review: Advanced functional polymer membranes. *Polymer*, 47:2217–2262, 2006.

[65] R. G. M. Van der Sman, H. M. Vollebregt, A. Mepschen, and T. R. Noordman. Review of hypotheses for fouling during beer clarification using membranes. *J. Membrane Sci.*, 396:22–31, 2012.

[66] R. Van Reis and A. Zydney. Review: Bioprocess membrane technology. *J. Membrane Sci.*, 297:16–50, 2007.

[67] M. Wessling. Two-dimensional stochastic modeling of membrane fouling. *Separation Purification Tech.*, 24:375–387, 2001.

[68] S. R. Wickramasinghe, E. D. Stumpb, D. L. Grzeniaa, S. M. Hussonc, and J. Pellegrino. Understanding virus filtration membrane performance. *J. Membrane Sci.*, 365:160–169, 2010.

[69] L. T. Yogarathinam, A. Gangasalam, A. F. Ismail, S. Arumugam, and A. Narayanan. Concentration of whey protein from cheese whey effluent using ultrafiltration by combination of hydrophilic metal oxides and hydrophobic polymer. *J. Chem. Tech. & Biotech.*, 93:2576–2591, 2018.

[70] A. L. Zydney and C. C. Ho. Scale-up of microfiltration systems: fouling phenomena and $v_{\max}$ analysis. *Desalination*, 146:75–81, 2002.